

# Resistance Spot Welding and In-Process Heat Treatment of Hot Stamped Boron Steel

by

Jeff Shao-Chun Hou

A thesis  
presented to the University of Waterloo  
in fulfillment of the  
thesis requirement for the degree of  
Masters of Applied Science  
in  
Mechanical Engineering

Waterloo, Ontario, Canada, 2016

©Jeff Shao-Chun Hou 2016

## **AUTHOR'S DECLARATION**

I hereby declare that I am the sole author of this thesis. This is a true copy of the thesis, including any required final revisions, as accepted by my examiners.

I understand that my thesis may be made electronically available to the public.

## **Abstract**

Escalating environmental concerns have prompted efforts to reduce vehicle weight and carbon emissions, resulting in increased application of advanced high strength steels (AHSS). 22MnB5 hot stamping grade AHSS, namely USIBOR 1500P, provide high strength to weight ratio allowing sheet thickness reduction to decrease weight, while maintaining high safety characteristics.

Resistance spot welding (RSW) has been the predominant welding process for automotive assemblies. Welding hot-stamping AHSS has introduced new challenges for achieving acceptable welds. The added alloying elements and high hardenability characteristics resulting in low weldability and weld toughness complicates this initiative. The current study examines the effects of in-process weld tempering with secondary current pulse has on the weld toughness during RSW of USIBOR steels.

RSW and weld tempering were tested on USIBOR at two different surface conditions; as-delivered and hot-stamped. Joint performance properties, micro-hardness map profiles, and failure modes of welds for both tempered and non-tempered conditions are detailed. Furthermore, a relationship between resulting joint performance and microstructural evolution is produced.

The objective of this work is to optimize in-process tempering parameters, analyze metallurgical evolution of the weldments, and compare the effects on mechanical performance for both tempered and non-tempered welds.

## Acknowledgements

I would like to foremost thank my academic supervisors, Dr. Adrian P. Gerlich and Dr. Norman Y. Zhou for their time, guidance, support and the given opportunity of this research project. Their knowledge and wisdom have guided and encouraged me through the progression of this research.

I would also like to acknowledge my industry collaborators, specifically Nigel Scotchmer and Kevin Chen from Huys Industry and Elliot Biro from ArcelorMittal Dofasco for their support. The research would not have been possible without the USIBOR sheet material from ArcelorMittal and the copper electrodes from Huys Industry.

I'd like to express my gratitude towards Dulal Saha for all of the invaluable comments during our technical discussions, encouragements, and assistance during lab experiments needed to complete this work.

I would also like to thank Dr. Yuquan Ding for his time and assistance in acquiring optical microstructure images much needed for this research.

I would also like to thank my readers, Dr. Adrian P. Gerlich, Dr. Norman Y. Zhou, Dr. Mary Wells, and Dr. Kaan A. Inal for their time and insight, as well as their positive feedback.

Last but not least, I would like to thank my family, friends, and colleagues from both within CAMJ and MME department for their support throughout the progression of this degree.

## Table of Contents

AUTHOR'S DECLARATION .....	ii
Abstract .....	iii
Acknowledgements .....	iv
Table of Contents .....	v
List of Figures .....	viii
List of Tables.....	xiii
List of Equations .....	xiv
Nomenclature .....	xv
Chapter 1 Introduction.....	1
1.1 Automotive Applications for Advanced High Strength Steels (AHSS).....	1
1.2 HF Steel Application for Anti-Intrusion Components .....	2
1.3 Problems to Resistance Spot Welding USIBOR 1500P.....	4
1.4 Objectives.....	4
1.5 Criteria and Constraints.....	5
1.6 Thesis Outline .....	6
Chapter 2 Literature Review .....	7
2.1 Resistance Spot Welding.....	7
2.1.1 Fundamentals.....	9
2.1.2 Weldability and Determination of Weld Quality .....	12
2.1.3 Welding parameters.....	13
2.1.4 Mechanical Performance of RSW .....	18
2.2 Welding Metallurgy for Ferrous Material .....	24
2.2.1 Fusion Zone (FZ) and Weld Solidification Process .....	25
2.2.2 Heat Affected Zone (HAZ) and sub-zones.....	26
2.3 Ferrous Martensite.....	27
2.3.1 Martensite Tempering .....	28
2.3.2 Rapid Tempering.....	29
2.4 USIBOR 1500P .....	30
2.4.1 Hardenability and Critical Temperatures .....	31
2.4.2 Base metal and coating morphology .....	34

2.4.3 Resistance Spot Weldability and Weld Performance.....	36
2.4.4 In-Process Tempering Methodologies .....	40
Chapter 3 Experimental Methods .....	41
3.1 Materials .....	41
3.1.1 Mechanical Properties.....	42
3.1.2 Specimen Dimensions.....	42
3.2 Resistance Spot Welding .....	43
3.2.1 Equipment.....	43
3.2.2 Welding Procedure.....	45
3.2.3 Weld Size Measurement .....	46
3.2.4 Vickers Hardness Testing .....	46
3.2.5 Tensile Testing.....	48
3.3 Metallographic Characterization.....	50
3.3.1 Sample Preparation .....	50
3.3.2 Microscopy .....	50
Chapter 4 RSW and In-Process Tempering of As-Delivered USIBOR Sheets .....	51
4.1 Welding Scheme Optimization .....	54
4.1.1 Application of pre-pulse current for coating removal.....	54
4.1.2 Weld growth progression .....	56
4.1.3 Tempering pulse selection .....	58
4.2 Mechanical Testing Results .....	59
4.2.1 Nugget Hardness Profile .....	59
4.2.2 Tensile Shear and Cross Tension Results .....	61
4.3 Tempered Microstructural Evolution.....	62
4.4 Summary .....	64
Chapter 5 RSW and In-Process Tempering of Hot-Stamped USIBOR Sheets.....	65
5.1 Welding scheme optimization.....	66
5.1.1 Quench period determination and Temper pulse application.....	67
5.1.2 Tempering Challenges .....	68
5.2 Mechanical Testing.....	70
5.2.1 Lap Shear and Cross Tensile Performance .....	70

5.2.2 Micro-hardness measurements .....	74
5.3 Failure Analysis.....	75
5.4 Weld Microstructure.....	79
5.4.1 Microstructural Evolution Comparison – Optical Microscopy .....	79
5.4.2 Microstructural Evolution Comparison – Scanning Electron Microscopy.....	84
5.5 Summary .....	87
Chapter 6 Conclusion and Recommendations.....	89
6.1 RSW and In-Process Tempering of As-Delivered USIBOR Sheets .....	89
6.2 RSW and In-Process Tempering of Hot-Stamped USIBOR Sheets.....	90
6.3 Future Work Recommendations.....	91
Appendix A Hot-Stamped USIBOR Weld Stereoscopy Images.....	93
Appendix B Instrumented Experimental Data .....	94
Bibliography.....	96

## List of Figures

Figure 1-1: Steel Application Trend in Automotive Industry [4] .....	2
Figure 1-2: Load transmission path in a BIW for different crash situations [7] .....	3
Figure 2-1: Resistance Spot Welding Machine Schematic [21] .....	8
Figure 2-2: Electrode and Stack-up Cross Section Schematics [22].....	8
Figure 2-3: Stages of Resistance Spot Welding [27] .....	9
Figure 2-4: Stack-up resistance between welding electrodes [21].....	10
Figure 2-5: Bulk resistivity vs. temperature between different base materials [23] .....	10
Figure 2-6: Resistance profile comparison between coated and uncoated steels [27] .....	11
Figure 2-7: Temperature distribution during RSW between Al-Si and Zn coated HF steel [28] .....	11
Figure 2-8: a) weld growth curve for fixed weld times b) weldability lobe at constant electrode force [21] .....	12
Figure 2-9: Multi-Pulse Profile Welding Scheme.....	15
Figure 2-10: Deflection of welder's arm under electrode force [33].....	17
Figure 2-11: Effects of nugget shapes due to misalignment modes [32] .....	17
Figure 2-12: Electrode pressure distribution due to misalignment [32].....	18
Figure 2-13: a) Chisel Test b) Peel Test [36].....	19
Figure 2-14: Tensile Shear Test schematics and fracture progression [39] .....	20
Figure 2-15: Cross tensile test schematics and fracture progression [39].....	21
Figure 2-16: Load-Displacement curve for weld joint tensile test [17] .....	22
Figure 2-17: Different failure/fracture modes for resistance spot welded nugget [40].....	23
Figure 2-18: Load- displacement curve difference between PO and IF failures [42].....	24
Figure 2-19: Peak temperatures and microstructural evolution of a weld zone [43] .....	25



Figure 2-20: Effect of carbon concentration of the ranges of lath and plate martensite of iron-carbon alloys [48] .....	27
Figure 2-21: Lath martensitic structure schematics and optical micrograph [50, 51] .....	28
Figure 2-22: Fe <sub>3</sub> C formation within martensite subjected to isothermal and non-isothermal tempering [58] .....	30
Figure 2-23: Hot Stamping Process: a) direct hot stamping, b) indirect hot stamping [10] .....	31
Figure 2-24: Continuous Cooling Transformation (CCT) Curve and Critical Cooling Rate [59] .....	33
Figure 2-25: M <sub>s</sub> and M <sub>f</sub> temperatures of 22MnB5 grade hot-stamping steel at various cooling rates [60].	34
Figure 2-26: USIBOR 1500P Morphology: A) As-delivered and B) Hot-stamped [8] .....	35
Figure 2-27: Al-Si Coating Morphology: A) As-delivered and B) Hot-stamped [8] .....	36
Figure 2-28: USIBOR RSW weld quality vs current: a) nugget diameter, b) tensile shear strength, c) cross tensile strength [60] .....	38
Figure 2-29: Effect of base metal strength on TSS and CTS of spot welded joints [68] .....	38
Figure 2-30: HF steel vs low carbon steel nugget hardness [60] .....	39
Figure 2-31: Microstructure and corresponding hardness mapping of boron alloy steel spot welds for welding currents of: a) 4kA, b) 6kA, and c) 8kA [69] .....	40
Figure 3-1: UofWaterloo Hydraulics Lab - Mini Macrodyne Press and Front Loading Furnance .....	41
Figure 3-2: Modified flanged tensile shear specimen .....	43
Figure 3-3: MFDC Spot Welder .....	44
Figure 3-4: RWMA CLASS II 8mm electrode schematics .....	44
Figure 3-5: Preliminary simulated weld thermal profile for tempering scheme optimization .....	45
Figure 3-6: Weld size measurement by metallographic inspection .....	46
Figure 3-7: Nanovea CB500 automated micro-indenter .....	47
Figure 3-8: AWS specified micro-hardness mapping [17, 18] .....	47

Figure 3-9: Modified straight line micro-hardness map for faying line hardness analysis .....	48
Figure 3-10: Tensile shear test setup: schematics and specimen layout [17, 18].....	49
Figure 3-11: Cross tensile test setup: schematics and specimen layout [17, 18] .....	49
Figure 4-1: As-delivered USIBOR weld: base material tearing around the nugget (red arrow) after cold forming.....	51
Figure 4-2: Tailored welded patch for indirect hot-stamping schematics: side flange weld failure (red) of a U-channel due to localized weld shear before final hot stamping operation [8].....	52
Figure 4-3: Weld fracture of As-delivered USIBOR welds after cold forming: weld fracture through the interface and sheet thickness [72] .....	53
Figure 4-4: A) Optical macrograph of cross-section when no pre-pulse is applied, B) detail of interface at nugget center, showing the Al-Si coating remaining at the interface. ....	55
Figure 4-5: Appearance of interface following the application of pre-pulse parameter cycle times and currents.....	56
Figure 4-6: As-delivered USIBOR nugget growth progression: A) growth progression after pre-pulse current (7.2 cycles) B) growth progression after 13.2 cycles welding time C) final nugget growth progression.....	57
Figure 4-7: Welding current pulses and SORPAS simulated thermal history for weld quench prior to in-process tempering pulses .....	58
Figure 4-8: Hardness map profile of as-welded and tempered weldments on as-delivered USIBOR sheets .....	60
Figure 4-9: Average hardness of nugget centers.....	60
Figure 4-10: Tensile shear and cross tensile joint performance comparison between as-welded (non-tempered) and tempered welds .....	61

Figure 4-11: Microstructural evolution of different tempering levels: A) 60% max current temper (9.6kA), B) 65% max current temper (10.4kA), C) 70% max current temper (11.2kA)..... 63

Figure 5-1: Hot-stamped USIBOR weld: initial nugget optimization..... 66

Figure 5-2: Weld Nugget Thermal Profile & Welding Scheme Pulses..... 67

Figure 5-3: Secondary weld pool formation from tempering pulse current due to electrode misalignment: A) severely misaligned, B) ideal alignment ..... 68

Figure 5-4: Example hot-stamped VS as-delivered USIBOR dynamic resistance..... 69

Figure 5-5: Hot-stamped USIBOR tensile shear joint performance comparison between tempered and non-tempered welds: A) load-displacement curves, B) calculated weld toughness ..... 71

Figure 5-6: Hot-stamped USIBOR cross tensile joint performance comparison between tempered and non-tempered welds: A) load-displacement curves, B) calculated weld toughness ..... 73

Figure 5-7: Weld Nugget Hardness Profile: a) As-Welded, b) Optimal Tempered, c) Overheated Tempered ..... 74

Figure 5-8: Cross tensile fracture cross-section of as-welded (non-tempered) hot-stamped USIBOR weldment ..... 76

Figure 5-9: Cross tensile fracture cross-section of optimally tempered hot-stamped USIBOR weldment . 77

Figure 5-10: Cross tensile fracture cross section of overheated tempered hot-stamped USIBOR weldment - fusion boundary fracture path..... 78

Figure 5-11: As-welded cross-section macrostructure and detailed microstructure of different regions: A) fusion zone (FZ), B) coarse grain region (CGHAZ), C) fine grain region (FGHAZ), D) inter-critical region (ICHAZ), E) base metal (BM) ..... 82

Figure 5-12: Tempered cross-section macrostructure and detailed microstructure of different regions: A) fusion zone (FZ), B) coarse grain region (CGHAZ), C) fine grain region (FGHAZ), D) inter-critical region (ICHAZ), E) base metal (BM) ..... 83

Figure 5-13: SEM micrographs at 20k magnification illustrating A-B, C, D, E) As-welded HAZ microstructures and T-B, C, D, E) Tempered HAZ microstructures ..... 86

Figure 6-1: USIBOR 1500P Base Metal Tensile Data..... 94

## **List of Tables**

Table 2-1: Stages of Tempering [52, 53].....	29
Table 3-1: USIBOR 1500P Chemical Composition.....	42
Table 3-2: USIBOR 1500P Material Property .....	42
Table 3-3: As-delivered coated welding scheme - for in-direct hot-stamping application .....	45
Table 3-4: Hot-stamped welding scheme - for direct hot-stamping application .....	46
Table 5: Tensile Shear Test Results for Hot-Stamped Tempered Welds .....	94
Table 6: Cross Tensile Test Results for Hot-Stamped Tempered Welds .....	95

## List of Equations

Eqn. 1: Joule Heating.....	9
Eqn. 2: Minimum Nugget Diameter .....	12
Eqn. 3: Minimum Shear Tension Strength.....	20
Eqn. 4: Minimum Cross Tension Strength.....	21
Eqn. 5: E. Miyoshi $A_{c1}$ Temperature Equation.....	33
Eqn. 6: E. Miyoshi $A_{c3}$ Temperature Equation.....	33
Eqn. 7: K. W. Andrews $M_s$ Temperature Equation.....	33

# Nomenclature

## List of Symbols

wt%	weight percentage concentration	[%]
$Y_s$	yield strength	[MPa]
UTS	ultimate tensile strength	[MPa]
E	elastic modulus	[GPa]
Q	heat	[J]
I	current	[A]
R	electrical resistance	[ $\Omega$ ]
$R_{\text{bulk}}$	bulk resistance	[ $\Omega$ ]
$R_{\text{int}}$	surface/interface contact resistance	[ $\Omega$ ]
t	time	[s]
$t_s$	sheet thickness	[mm]
$D_{\text{weld}}$	nugget diameter	[mm]
$D_{\text{electrode}}$	electrode tip diameter	[mm]
$M_s$	martensite start temperature	[ $^{\circ}\text{C}$ ]
$M_f$	temperature of 100% martensite transformation	[ $^{\circ}\text{C}$ ]
$Ac_1$	austenite transformation temperature	[ $^{\circ}\text{C}$ ]
$Ac_3$	complete austenite transformation temperature	[ $^{\circ}\text{C}$ ]

## **List of Abbreviations**

AHSS	Advanced High Strength Steel
AWS	American Welding Standards
BIW	Body in White
BM	Base Material
CCT	Continuous Cooling Transformation
CGHAZ	Coarse Grain Heat Affected Zone
CT	Cross Tension Strength
CTT	Cross Tensile Test
FZ	Fusion Zone
FB	Fusion Boundary
FGHAZ	Fine Grain Heat Affected Zone
HAZ	Heat Affected Zone
ICHAZ	Inter-critical Heat Affected Zone
MS	Martensitic Steel
MFDC	Medium Frequency Direct Current
OM	Optical Microscopy
PWHT	Post Weld Heat Treatment
RSW	Resistance Spot Welding
SCHAZ	Sub-critical Heat Affected Zone
SEM	Scanning Electron Microscopy
ST	Shear Tension Strength
TST	Tensile Shear Test
UCHAZ	Upper-critical Heat Affected Zone

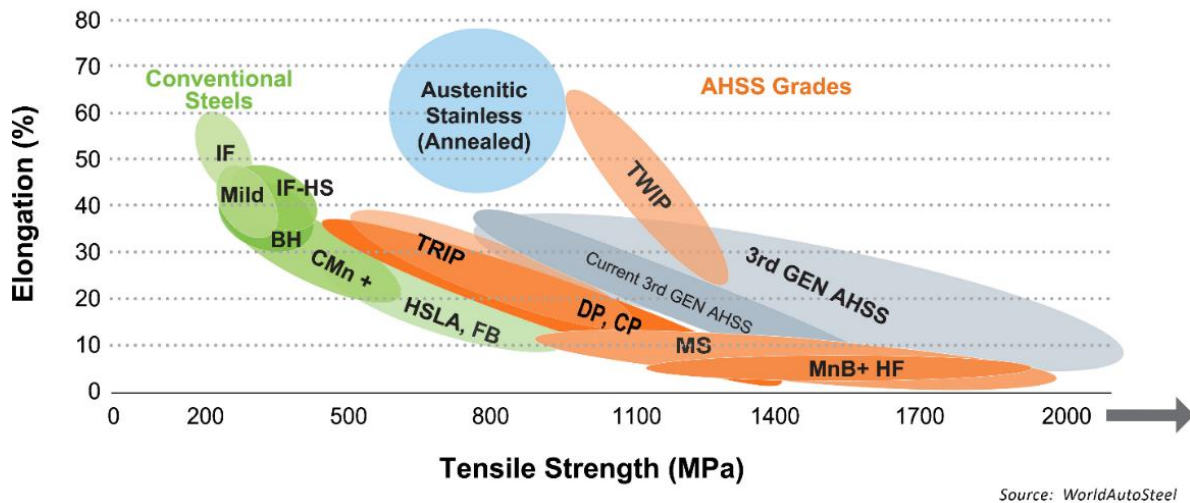


# Chapter 1

## Introduction

### 1.1 Automotive Applications for Advanced High Strength Steels (AHSS)

Escalating concerns regarding climate change due to CO<sub>2</sub> emissions have prompted the U.S Environmental Protection Agency (EPA) to issue legislations to reduce the average automotive fleet carbon emissions level from 155 grams/km in 2016 down to 101 grams/km by 2025 [1]. One of the means to achieve these goals is by vehicle weight reduction, which also reduces fuel consumptions, where fuel savings of 0.15-0.70L/100km can be achieved per 100kg of mass reduction [2]. Vehicle weight reduction can be achieved by increased utilization of non-ferrous or low-density materials such as aluminium alloys or fibre-reinforced polymers [3]. However, the high cost of these alternative materials make them less attractive for production of high volume car models, and these also impede the recyclability of used vehicles. As a result, steel will continue to be used considering its cost, suitability for high volume productions, and recyclability. The typical approach to vehicle weight reduction for steel body-in-white (BIW) involves reductions in sheet thickness. However, this may result in a decrease in BIW structural integrity, compromising occupant safety. In order to address weight reduction while maintaining occupant safety, application of advanced high strength steels (AHSS) has been incorporated [4].

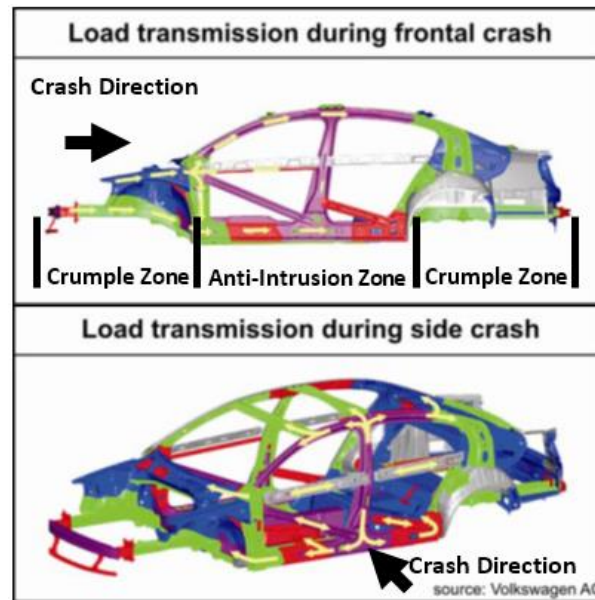


**Figure 1-1: Steel Application Trend in Automotive Industry [4]**

AHSS includes many families of steels with various microstructural and performance properties, such as: Dual Phase (DP), Complex-Phase (CP), Ferritic-Bainitic (FB), Martensitic (MS or MART), Transformation-Induced Plasticity (TRIP), Hot-Formed (HF), and Twinning-Induced Plasticity (TWIP) [4]. It is a general trend that increasing material strength resulted in diminishing elongation, as depicted in Figure 1-1. The material of particular interest is the aluminized 22MnB5 HF steel, trade-named USIBOR 1500P by ArcelorMittal.

## 1.2 HF Steel Application for Anti-Intrusion Components

The selection for AHSS grades is dependent on the location of application in the BIW. For example, DP or TRIP steels are well suited for crumple/crash zones where high energy absorption characteristics are crucial [4, 5, 6]. Meanwhile, MS and HF steels with extreme high strengths are well suited for anti-intrusion components which make up the passenger compartments. However, locations that bridge between different zones within the BIW require specific material characteristics for optimal load transmission during crash events Figure 1-2.



**Figure 1-2: Load transmission path in a BIW for different crash situations [7]**

HF components consists mainly of martensitic microstructure due to high hardenability characteristics after hot-stamping, a production process comprises of heating HF steel blanks to a malleable state at high temperatures and stamped/quenched to the desired geometrical form in one swift stroke. Hot-stamped USIBOR 1500P offers tensile strength up to 1500MPa and low elongations of 5% [8]. Low ductility characteristics of this material impedes impact (crash) performance, especially in side impact scenarios depicted in Figure 1-2. As a result, it becomes imperative for anti-intrusion components to have varying (tailored) properties with increased elongation for higher energy absorption [7]. Production of components with tailored properties can be achieved with modification to the thermal processes by reducing cooling rates low enough to avoid full martensitic microstructure during hot-stamping. This process can be done by varying cooling rates with the integration of heating elements within the forming dies to reduce cooling rates at desired locations [7, 9, 10]. Alternatively, tailoring can be achieved by welding different grade materials to form one component, which are known as tailored welded blanks [10].

### **1.3 Problems to Resistance Spot Welding USIBOR 1500P**

In light of increasing demand for HF grade AHSS and tailored properties requirement for hot-stamped components, there are, on the other hand, limited study on weldability and weld tailoring of USIBOR 1500P; which in turn may limit its applicability. Optimization and analysis of resistance spot welding of USIBOR 1500P will enable more efficient utilization of the steel. The following comprise the main problems found in RSW of USIBOR 1500P. One of the challenges to resistance spot welding USIBOR 1500P is weldability. The operating window for RSW of the steel is generally narrower compared to conventional automotive steels [11, 12]. This can be attributed partly to their surface coating that serves as an oxidation barrier during hot stamping [13]. Additionally, the added alloying elements for hardenability enhancements contributes to accelerated resistive heat generation, thus resulting in increased chances of weld expulsion when welding USIBOR 1500P steels. Due to the high hardenability characteristics of USIBOR 1500P, weld nuggets are prone to interfacial failures due to notch sensitivity [14, 15, 11]. High hardenability results in microstructures with high hardness and low ductility in the weld heat affected zone (HAZ). A narrow softened or tempered zone subjected to sub-critical temperatures is typically formed and surrounded by high hardness surrounding materials, leading to a brittle stress concentration points that promotes crack propagation. An interfacial fracture mode is normally associated with low energy absorption [5, 16]. However, USIBOR 1500P spot welds normally fail interfacially, even when achieving high fracture strengths. Welds which fail interfacially still exhibit poor energy absorption properties. This is crucial in terms of welds subjecting to impact loading, since this essential to the crashworthiness of vehicles.

### **1.4 Objectives**

The aim of this thesis is to understand resistance spot welding process of USIBOR 1500P with varying welding schemes (processing conditions), analyze metallurgical transformations of weldments for

both fusion and heat affected areas (microstructures), and its effects on mechanical performance in various tensile loading modes and weld hardness characteristics (properties). The specific objectives of this thesis are as follows:

1. To investigate the practicality of rapid martensite tempering with in-process tempering method during RSW of USIBOR. In addition, to optimize and analyze welding schemes for two sheet stack-up of USIBOR 1500P steels. Welding scheme optimizations were done on both as-delivered and hot-stamped USIBOR steels.
2. To compare joint performance between as-welded and tempered welds by evaluating fracture loads, displacements, and energy (weld toughness).
3. To correlate the hardness of rapidly weld tempered USIBOR weld nuggets with microstructures using optical and scanning electron microscopy.

## **1.5 Criteria and Constraints**

The assessment of spot weld properties and characteristics are based upon recommended practices according to American Welding Society (AWS) and International Organization Standardization Organization (ISO) standards [17, 18, 19]. Mechanical testing methods used in this researched are detailed in following chapters. Additional mechanical property tests of the USIBOR base material are based upon ASTM International E8-10 [20]. This thesis work is limited to the investigation of the effects of RSW and tempering of USIBOR hot-stamping steel. Attention has been addressed in particularly for the hot-stamped condition of the USIBOR steel, since it is the common condition in which it is welded during automotive manufacturing. Material thickness is restricted to 1.2mm and 1.5mm due to availability and the corresponding electrode sizes used are recommended by AWS guidelines. An important consideration that was encountered during this thesis work is the electrode alignment during RSW. This was unexpectedly

found to have a dramatic influence on the output when applying tempering in-situ during RSW, and represents one of the critical issues to be addressed in terms of industrial applications.

## **1.6 Thesis Outline**

This thesis report has been organized in 7 chapters as follows:

- Chapter 1: Introduction to background, problem, objectives, justification and constraints.
- Chapter 2: Literature review – characteristics of RSW process, fundamentals of ferrous RSW microstructural evolution, processing of USIBOR 1500P and its characteristics, and tempering evolution of martensitic steels.
- Chapter 3: Experimental Methods – details on materials, instrumentation and characterization methods, experimental procedures, simulation software, and modelling theory.
- Chapter 4: As-Delivered state USIBOR Welding and Tempering – details welding challenges with as-received coatings and heat balance. Application of in-process tempering pulses and evaluation of resulting weld performance.
- Chapter 5: Hot-stamped state USIBOR Welding and Tempering – details the application of in-process tempering pulse on hot-stamped USIBOR welds and evaluation of resulting weld performance in comparison to un-treated weld nuggets.
- Chapter 6: Conclusions and Recommendations – summarizes the main findings, the knowledge and contributions attained to this research work, and proposed future work.

## Chapter 2

### Literature Review

#### 2.1 Resistance Spot Welding

Resistance spot welding (RSW) is an autogenous welding process (meaning no filler metal is added) in which contacting metal surfaces are joined together with localized heat generation due to resistance of an applied electric current [21, 22, 23, 24]. The invention of resistance welding was accredited to Elihu Thomson when he accidentally fused two electrical wires together during an experiment. Thomson filed the patent *Method of Electric Welding* [25] in 1890 and the welding principle was further developed into resistance spot, seam, projection, and flash butt welding [26].

RSW has been the predominant welding method for joining steel sheets in automotive manufacturing, specifically for body-in-white (BIW) construction. The process is rapid, easily automated, autogenous, and requires little skill to operate, thus making it suitable for high capacity production lines [24]. Presently, a typical BIW includes 4000-6000 spot welds, depending on the model and size of the vehicle [21].

RSW involves coordinated application of electric current and mechanical pressure of the proper magnitude in order to generate a defect free weld. Due to the short current path of a typical two sheet stack-up, low voltage, high current is necessary to develop the desired amount of heat for welding. Figure 2-1 illustrates a schematic of a resistance spot welding setup. The current from incoming single phase power is stepped up through a welding transformer and into the welding horn which is connected using flexible conductors. The horn is constructed out of heavy duty copper arms with electrode holders where copper alloyed welding electrodes reside. Figure 2-2 illustrates the cross section of a two sheet stack-up clamped between water cooled electrodes at specified electrode pressure. Water cooling is generally supplied to the

electrodes to prevent these from overheating/melting. During welding either alternating (AC) or direct current (DC) is passed from the electrodes through the clamped workpieces. Peak heat generation and material fusion occurs at the workpiece faying surfaces due to high resistance at the faying interface combination compared with the electrode to workpiece interfaces, resulting in a welded joint.

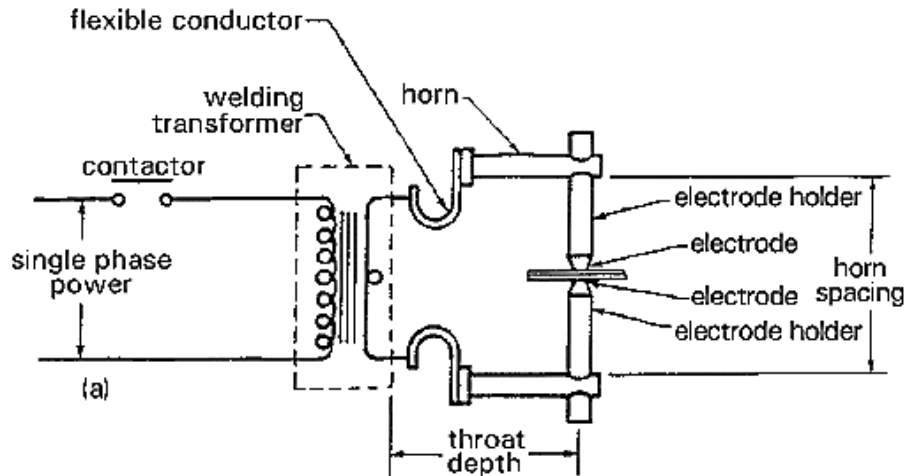


Figure 2-1: Resistance Spot Welding Machine Schematic [21]

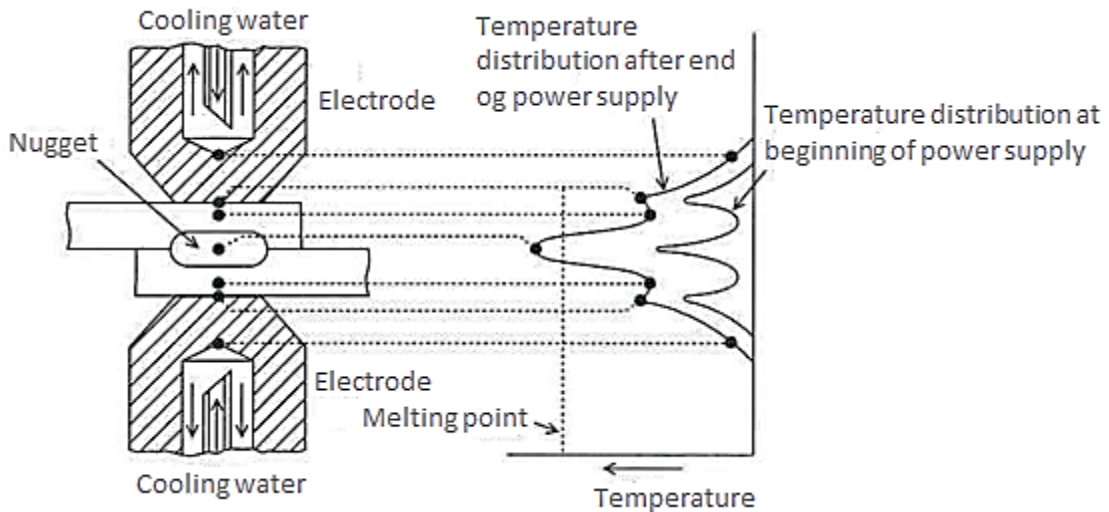


Figure 2-2: Electrode and Stack-up Cross Section Schematics [22]



The RSW process consists of 5 distinct stages: 1) initial squeeze of the work pieces between electrodes, 2) application of the electrode force to desired load 3) application of current for heat generation at the faying interface, 4) holding time to allow for solidification of the molten metal and finally 5) electrode release of the work pieces.

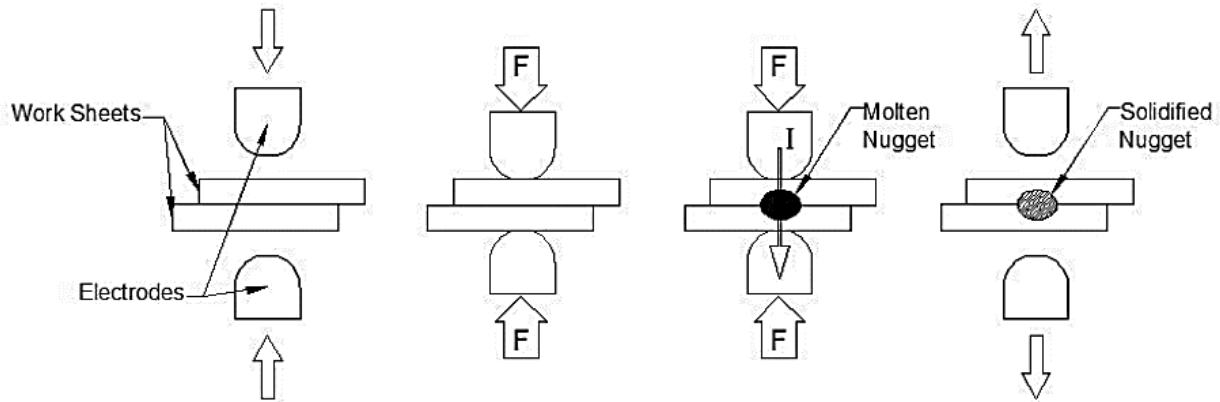


Figure 2-3: Stages of Resistance Spot Welding [27]

### 2.1.1 Fundamentals

The physical principle of RSW can be expressed by Joule's first law or Joule Heating, quantifying the amount of heat released by passage of electric current through a conductor. Joule heating is expressed as:

$$Q = I^2Rt, \quad \text{Eqn. 1: Joule Heating}$$

where  $Q$  [J] is the amount of heat generated,  $I$  [Amps] is the current applied through the conductor,  $R$  [ $\Omega$ ] is the total resistance of the conductor, and  $t$  [s] is the time of the duration of applied current.

The resistance of the conductor is the summation of various interface and bulk resistances in series of the sheet metal stack-up. A typical two non-coated sheet stack-up setup consists of seven resistances across the circuit (Figure 2-4).  $R_1$  and  $R_7$  are electrode bulk resistances, where the resistivity is lowest due

to the excellent electrical conductivity of the copper electrodes. R2 and R6 are electrode to workpiece contact resistances; due to the contact with copper electrodes, these resistances are relatively low. R3 and R5 are workpiece bulk resistances; resistivity of the bulk material is dependent to electrical conductivity characteristics of the base material (Figure 2-5). Finally, R4 is the workpiece interface resistance; this resistance is generally the highest between the steel-steel interfaces, resulting in highest heat generation in this area to create the weld pool.

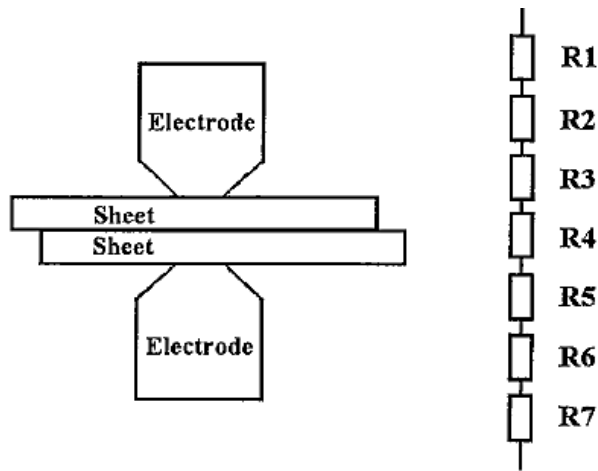


Figure 2-4: Stack-up resistance between welding electrodes [21]

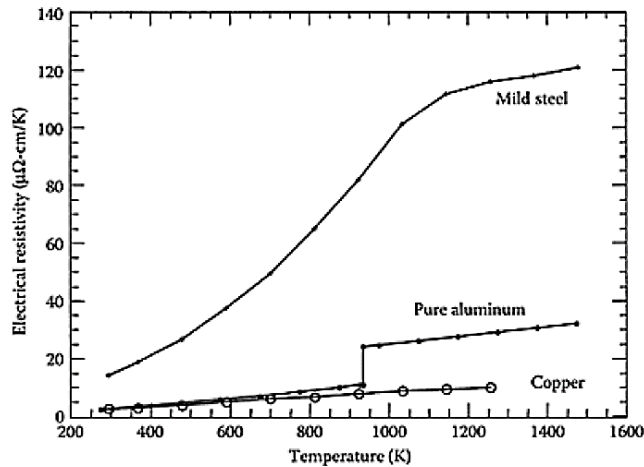
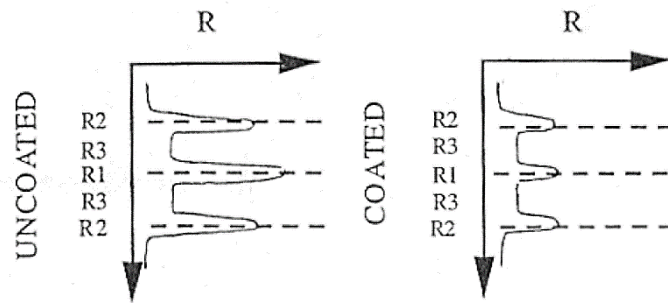


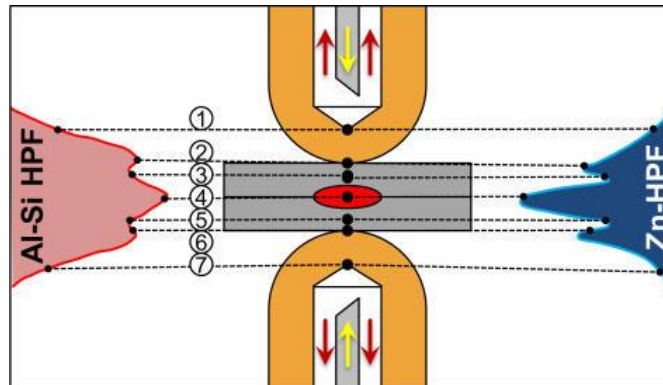
Figure 2-5: Bulk resistivity vs. temperature between different base materials [23]

Resistances for coated steels compared to uncoated ones differ significantly. In the case of automotive steels, coatings such as hot-dipped galvanized (HDG; Zn based coating) are typically used; which have a melting point much lower than that of the steel. This leads to melting of the coating during RSW, which may suddenly drastically reduce the contact resistance,  $R_4$ . This significantly influences the heat generation potential, resulting in required higher current input to attain acceptable weld sizes [23]. Figure 2-6 illustrates a sample of resistance differences between coated and non-coated steels.



**Figure 2-6: Resistance profile comparison between coated and uncoated steels [27]**

In the case of hot-stamping steels such as USIBOR 1500P, the Al-Si protective coatings used to prevent oxidation during thermal treatment are diffused with iron, resulting in formation of intermetallic layers of higher resistivity, promoting heat generation (Figure 2-7) [28, 29].



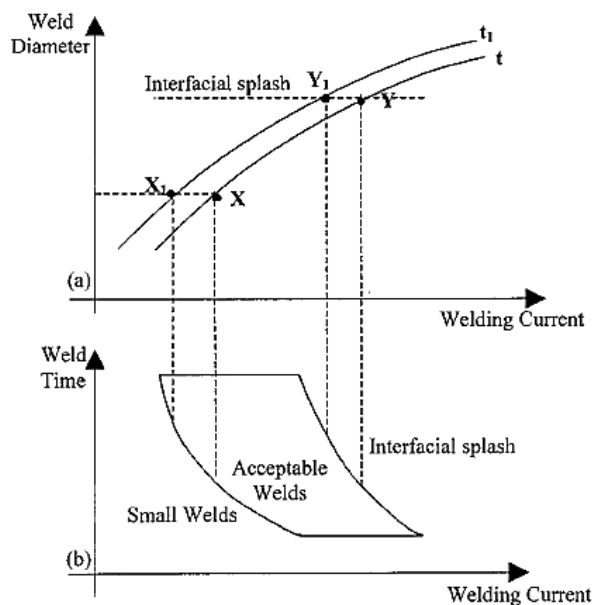
**Figure 2-7: Temperature distribution during RSW between Al-Si and Zn coated HF steel [28]**

### 2.1.2 Weldability and Determination of Weld Quality

Weldability in resistance spot welding is a measure of how effectively a particular material stack-up combination can be welded using specified electrodes and forces. Weldability lobes (Figure 2-8) describe the upper and lower limits of the system with respect to parameters such as weld current and weld time combinations that produce satisfactory weld sizes. The lower limit for a satisfactory weld is determined by the minimal weld diameter expressed as [18]:

$$M_{dia} = 4\sqrt{t_s} \quad \text{Eqn. 2: Minimum Nugget Diameter}$$

given by AWS D8.9M, where  $M_{dia}$  is the minimum weld diameter (mm) and  $t_s$  is the material sheet thickness (mm).



**Figure 2-8: a) weld growth curve for fixed weld times b) weldability lobe at constant electrode force [21]**

The upper limit of the satisfactory is determined by the observation of weld flash or expulsion. Weld flash occurs when heat generation is too rapid, resulting in the electrode to sheet interface to glow red hot during welding. Weld expulsion occurs when the molten weld pool grows too rapidly and too large for

the constant cooling of the electrodes to contain, resulting in molten material being expelled out of the faying interface or near surface of the sheets adjacent to the electrode. The ranges of current and time which define the weldability is determined by the relative power required to form a weld, as well as the robustness of the weld system. Typically, wide weldability lobes are more robust than narrow lobes, as there will be a greater range of current that can be applied to form a satisfactory weld.

### **2.1.3 Welding parameters**

The main parameters that can be controlled during resistance welding machine are welding current, welding and cooling times, electrode geometry, and electrode force. Each of these parameters have different effects on the resulting weld quality. The combinations of these parameters determines the weld quality and ranges for the weldability lobe.

#### **2.1.3.1 Welding Current**

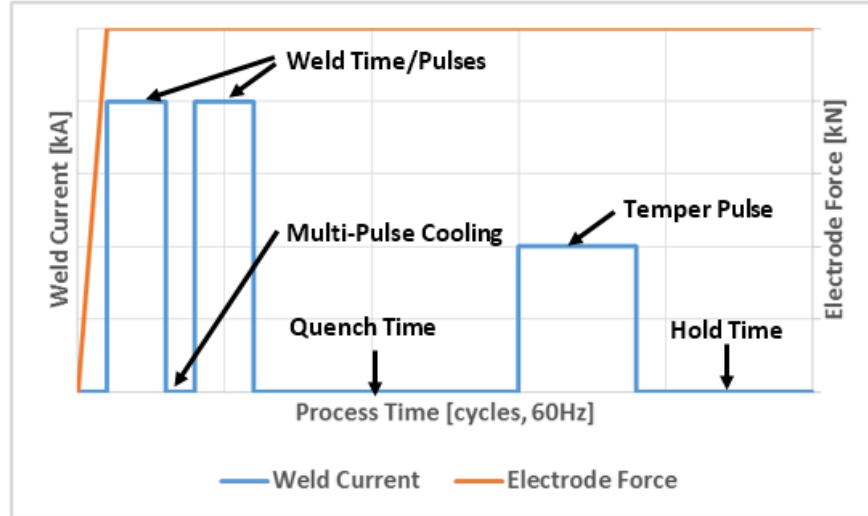
The weld current can either be alternating (AC) or direct (DC) currents. AC current sources causes the weld pool to grow in steps as the current switches polarity. DC current sources, on the other hand results in continuous growth of weld pool. The weld current can be considered the most influential to heat generation during resistance spot welding. According to Eqn. 1, the heat generation is proportional to the square of the applied current. Essentially, doubling the current will quadruple heat generation of any period of weld time. The automotive industry has mainly setup its assembly lines with AC resistance spot welding machines and DC powered machines have been limited to more specialized applications. Recently, medium frequency DC (MFDC) spot welders have become more popular due to increased energy savings, shorter welding times compared to AC, and reduced capital costs related to high current transformers [12, 30].

### 2.1.3.2 Welding and cooling time

Time can be differentiated between welding and cooling times. Time is generally measured in cycles with 60 cycle/seconds for the 60Hz North American machines. Times for DC power supplies are measured in milliseconds.

Weld time is the period which current is applied to the weld pool. Weld current and weld times are complementary to each other. At low weld currents, sufficient time is required for heat generation. In contrast, high weld currents requires low weld times to avoid expulsion. However, time cannot be shortened too much regardless of the increase of current. Based on Eqn. 1, heat generation is proportional to the square current. The effect of high current and short time combination would generate heat too rapidly, resulting in pitting, surface flashing, or weld expulsion. Weld time is commonly set constant depending on material thickness, grade, and coating, as per AWS D8.9M: 2012 for automotive steel materials.

Cooling times are measured during the period when current stops flowing, but electrode force is still applied. During this time, heat generation is halted and heat is conducted away from the weld by the water cooled electrodes and adjacent bulk material. The cooling time is also generally known as holding time that occurs at the end of the applied current pulse so the weld pool can solidify. Holding times allow enough molten material to solidify to provide the weld with sufficient structural strength. Long holding times are generally applied for weld pools to fully solidify. However, this may not always be desired as rapidly quenched weld pools may form porosities or void shrinkages. As a result, holding times can be shortened by releasing the electrodes before the weld pool fully solidifies, allowing the remainder molten material to solidify by conduction to the surrounding material or convection to the surrounding air.



**Figure 2-9: Multi-Pulse Profile Welding Scheme**

Depending on welding schemes, cooling times can either be identified as multi-pulse cooling or quench times. For thicker materials, multi-pulsed schemes are desired in order to form high quality welds of sufficient size without risking premature expulsion, the cooling periods in between pulses are identified as multi-pulse cooling times [31]. These cooling periods typically range from 2 to 4 cycles, or 33 to 66 milliseconds as defined by AWS D8.9M [18].

For welds that require post weld heat treatments (PWHT), an intermission quench time is applied for the weld to completely solidified, as molten material cannot be meaningfully heat treated with temper pulses. This is akin to the application of external heating following other welding processes in order to suppress brittleness or excessively hard microstructures in steels. In the case of RSW, this PWHT can be applied during the process by the electrodes, by using a current which is below the threshold required to cause melting of the sheets, essentially allowing heat treatment to be performed in-situ shortly after the weld is formed.

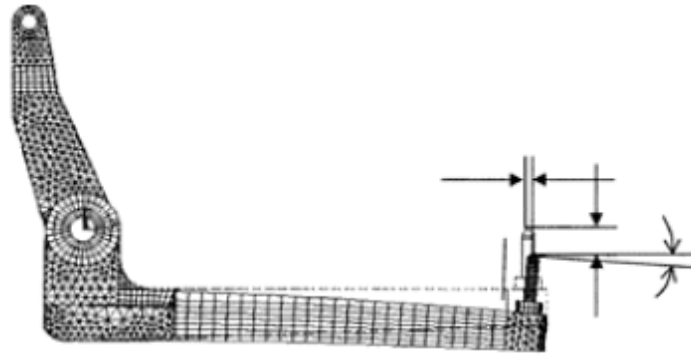
### 2.1.3.3 Electrode Pressure

The pressure applied by the electrodes helps to secure the workpieces together during welding. There are two stages of weld forces; initial squeeze force and welding force. The initial squeeze force is required to avoid unwanted motion of the electrodes upon the workpieces prior to the weld, aiding electrode and material alignment. Prior to the application of weld current, the electrode force is intensified to a desired level, this is known as the weld force. The weld force influences contact resistances of the material stack-up, thus influences the resulting heat generation. A low electrode force may lead to a reduction of actual contact between workpieces, and the resulting contact resistance will be high. Low electrode forces lead to a risk of rapid heat generation and expulsion as there is insufficient force to contain the expanding weld metal. On the contrary, higher weld forces lowers interfacial contact resistance as micro asperities between interfaces are “squeezed” together. As a result, lower heat generation may occur and this must be compensated for with increased weld current/time combinations.

### 2.1.3.4 Electrode Alignment

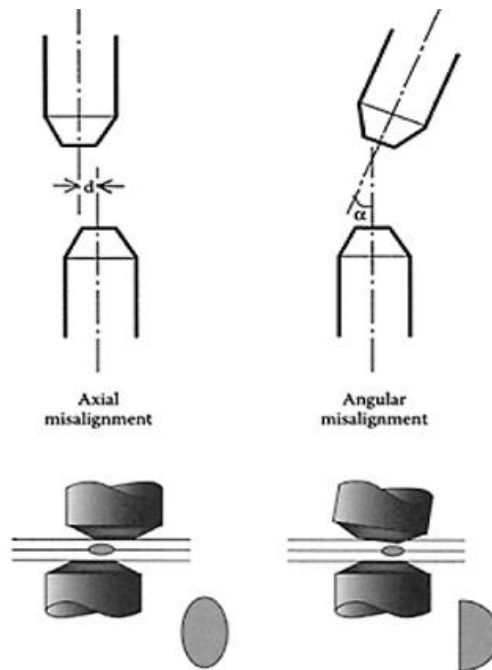
Under ideal conditions, the top and bottom electrodes are situated with faces parallel to each other and concentrically overlapping during welding. Good electrode alignment ensures uniform electric current conduction and heat generation for nugget formation [32, 33]. Poor alignment can cause poor weld qualities such as diminishing weld strengths due to undersized nuggets or even expulsion. Electrode misalignment can be attributed to factors such as poor electrode setup, low machine stiffness, and dynamic movements during welding [33]. Figure 2-10 is a schematic illustrating deflection of a welder’s arm under forces during welding. At high electrode forces or weldment of heavy gauge sheet material, deflection due to poor machine stiffness can cause electrodes to become misaligned in both axial concentricity and angular alignment.





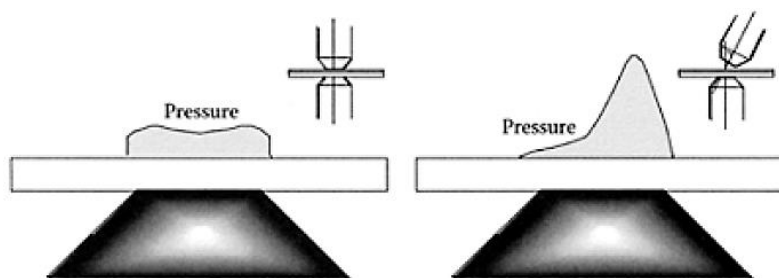
**Figure 2-10: Deflection of welder's arm under electrode force [33]**

Irregular nugget shapes can occur for misaligned electrodes due to an imbalance of electrode forces and heat generation. Figure 2-11 illustrates probable nugget shapes due to different misalignment modes. Assuming axial misalignment in only one of the axis, electrical current is forced to travel at an angular path from the one electrode to another. The resulting nugget shape will be oval due to narrowing of current density along the displaced direction.



**Figure 2-11: Effects of nugget shapes due to misalignment modes [32]**

When electrodes are angularly misaligned, pressure generated from the applied electrode force will concentrate to one side. Figure 2-12 illustrates the pressure distribution comparison between ideally aligned electrodes to angular misaligned electrode. For ideally aligned electrodes, the pressure is evenly distributed around the electrode edge in order to contain the molten nugget and prevent weld expulsion [34]. For angularly misaligned electrode, clamping pressure distributes asymmetrically, causing increased risks of weld expulsion [35].

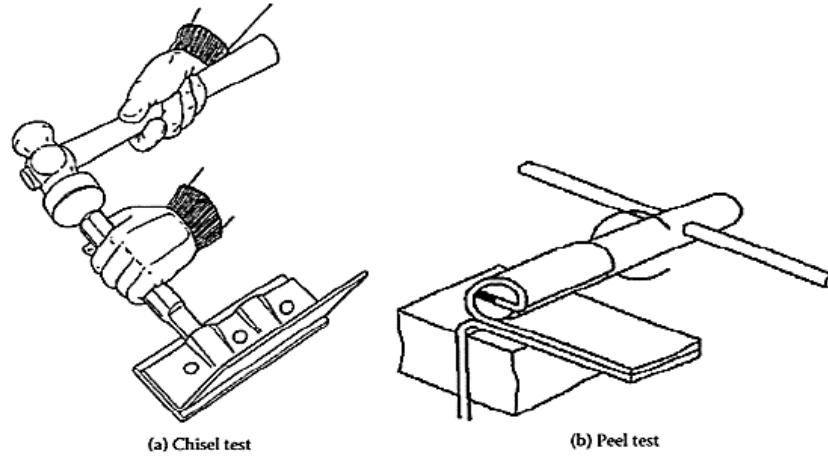


**Figure 2-12: Electrode pressure distribution due to misalignment [32]**

## **2.1.4 Mechanical Performance of RSW**

### **2.1.4.1 Qualitative (Destructive) Tests**

Various destructive mechanical tests are done on the weld nuggets to either qualitatively or quantitatively assess their soundness. A large portion of these destructive tests are performed at assembly lines, where time restraining circumstances only allows for weld button size and failure mode monitoring. The two general qualitative tests are chisel test and peel test. Chisel tests involves driving a chisel wedge in between welds to assess brittle fracture behavior of the specific weld (generally done after the weld has cooled down). The peel test involves peeling one of sheet lap jointed to the other sheet that is anchored (normally by a vice). Once workpiece is peeled away revealing the weld faying surface, button diameter and failure mode is monitored and evaluated [36].



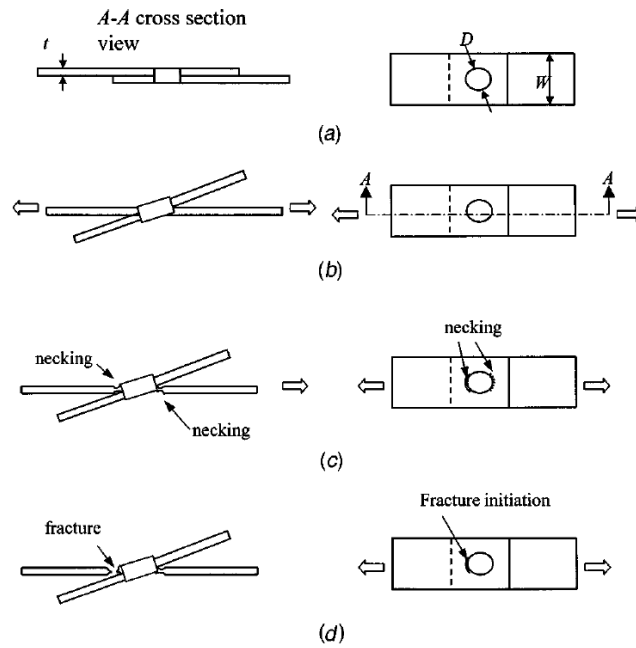
**Figure 2-13: a) Chisel Test b) Peel Test [36]**

#### 2.1.4.2 Tensile Shear (TST) and Cross Tensile Test (CTT)

In order to quantitatively evaluate the soundness of weld nuggets (strength and ductility), instrumented performance tests, where load and displacement quantities are monitored and recorded, are conducted. The two common instrumented tension tests are tensile shear (TST) and cross tensile test (CTT) [36, 37, 38].

TST (also known as shear test) is done on a lap welded specimen (Figure 2-14a) by subjecting the sample to uniaxial loading until weld fracture by “shearing” mode. The testing method focuses on the weld nugget integrity (stiffness) under shear loading mode. Figure 2-14 is a schematic demonstrating the failure progression of a lap welded specimen undergoing TST. Initially, the weld nugget experiences rotation as the specimen is pulled. As the loading progresses, the material surrounding the nugget begin to deform, similar to a rigid button embedded in ductile material. Finally necking occurs (generally in the  $0^\circ$  and  $180^\circ$  positions) at the edge of the nugget. Under ideal circumstances for pullout failure, fracture is initiated at one of these two points and the weld button will be pulled out [39]. If the weld fails interfacially, the fracture initiates at the faying area and fractures through the nugget. It can be noted that nugget rotation can be

minimized by shimming the grip regions of each sheet to equal thicknesses to ensure axial loading through the nugget [17, 18, 38]. Additionally, increased specimen width as well as increased base material stiffness also minimizes nugget rotation [38].



**Figure 2-14: Tensile Shear Test schematics and fracture progression [39]**

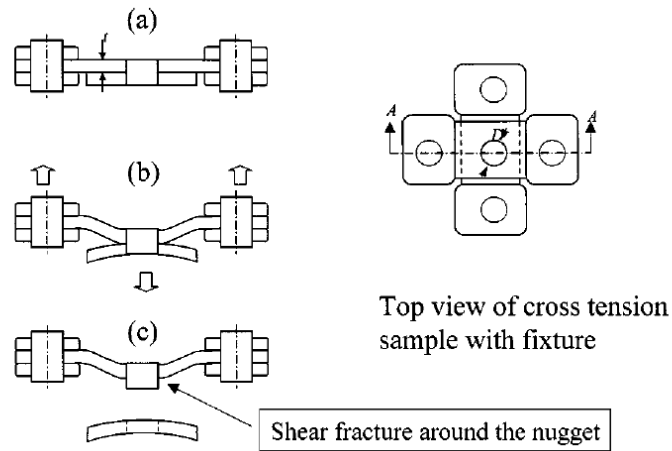
Minimum shear tension strength has been defined by AWS D8.1M:2007 to ensure minimum acceptable shear tension weld strength is achieved. The minimum strength is a function of base material strength and sheet thickness. The relation is defined by the following:

$$ST = \frac{(-6.36e-7*UTS^{-4}+6.58e-4*UTS+1.674)*UTS*4*t_s^{1.5}}{1000} [17]$$

Eqn. 3: Minimum  
Shear Tension  
Strength

where, ST is the shear tension strength in (kN), UTS is the base metal tensile strength (MPa), and  $t_s$  is the material thickness (mm).

CTT (also known as tension test) subjects the weld nugget in the normal direction in order to test the “opening” resistance of the weld nugget. Failure load results from CTT are dependent on base material sheet thickness, strength and ductility, as well as heat-affected zone strength and ductility of the weld region [37]. CTT requires specialized specimen geometry and grip fixtures to ensure normal tension is applied on the weld (details will be highlighted in chapter 3).



**Figure 2-15: Cross tensile test schematics and fracture progression [39]**

Figure 2-15 demonstrates the deformation pattern and failure progression of cross tensile specimen during CTT. Initially, large bending deformation occurs along the width of the sample. As the loading progresses, necking and fracture occurs around the weld button. Eventually, the weld nugget is pulled out from either one of the coupons and stays with the other coupon for pullout failure.

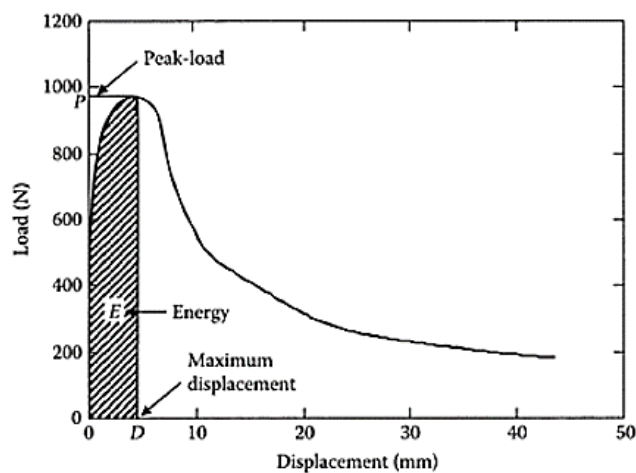
The minimum cross tension strength recommended by AWS D8.1M:2007 is a function of the base material thickness. The equation is given as:

$$CT = 1.25 * t_s^{2.2} [17] \quad \text{Eqn. 4: Minimum Cross Tension Strength}$$

where, CT is the cross tension strength in (kN), and  $t_s$  is the material thickness (mm).

### 2.1.4.3 Quantitative Result Interpretation

Recorded data from instrumented tensile tests are generally in the form of load-displacement curves for weld joint tensile test. Stress-strain calculations are generally not used to quantify RSW performance due to the dynamic nature of the weld nugget during loading, thus it becomes difficult to properly gauge the changes in nugget area as well as utilization of strain gauges on the welded specimen. Figure 2-16 depicts a general load-displacement curve for a weld joint tensile test.



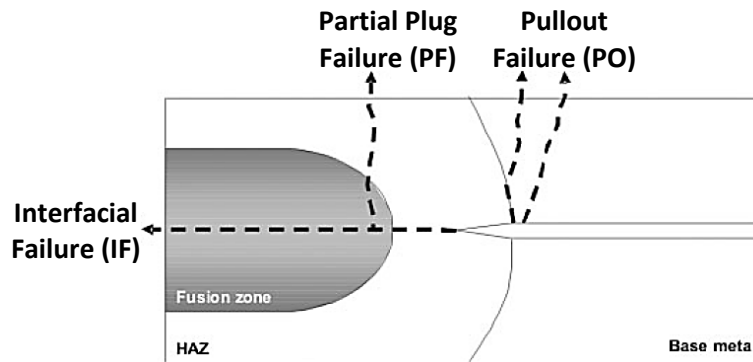
**Figure 2-16: Load-Displacement curve for weld joint tensile test [17]**

For a typical weld load-displacement curve, the following information is usually collected.

- Peak load – The maximum load attainable of the weld during tensile test prior to fracture.
- Ductility – is the maximum weld displacement prior to fracture (“D” in Figure 2-16).
- Energy – The total energy absorption is calculated as the area under the curve from load/displacement origin until the peak load.

#### 2.1.4.4 Weld Failure Mode

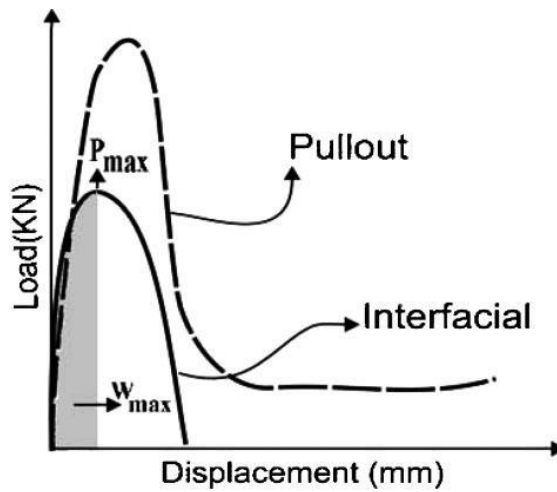
There are eight different combinations of failure modes for resistance spot welds identified by AWS D8.1M:2007: button pullout, partial thickness fracture with button pullout, partial thickness fracture, interfacial fracture with button pullout and partial thickness, interfacial fracture with button pullout, interfacial fracture with partial thickness fracture, interfacial fracture, and finally, no fusion [17]. For simplicity, only three main failure modes are considered: pullout failure (PO), partial plug failure (PF), and interfacial failure (IF) [40, 41].



**Figure 2-17: Different failure/fracture modes for resistance spot welded nugget [40]**

Figure 2-17 illustrates the different fracture paths of IF, PF, and PO failures.

PO welds are generally associated to large welds, where the weld nugget is completely pulled out from one of the metal sheets, leaving a hole in the other. In the case of IF, fracture primarily initiates at the faying notch and fracture propagates through the fusion zone. IF is associated to small welds which has low load carrying and poor energy absorption capability and is often avoided in industry standard [16, 39, 42]. PF welds share a mixture of interfacial and pullout failure, where fracture first propagates in the fusion zone and then is redirected through the thickness of the base metal.



**Figure 2-18: Load- displacement curve difference between PO and IF failures [42]**

Many welding institutes including AWS and ISO have defined the minimum weld nugget to be given by Eqn. 2. However, IF remain persistent for AHSS welds even when nugget diameter surpasses minimum requirement. It has been argued that the dynamic of weld fracture for AHSS significantly differs than that of conventional automotive sheet steels, thus weld quality checks for AHSS welds should not be deemed solely on fracture modes [38].

## **2.2 Welding Metallurgy for Ferrous Material**

Figure 2-19 illustrates the relationship between peak temperatures, Fe-C binary phase diagram, and resulting microstructural evolution of a gas metal arc welding (GMAW) weld. The schematic offers similar temperature to microstructural evolution relationship for many fusion welding process, including RSW. A typical fusion weld section composes of two distinct zones; fusion zone (FZ) and heat affected zone (HAZ).



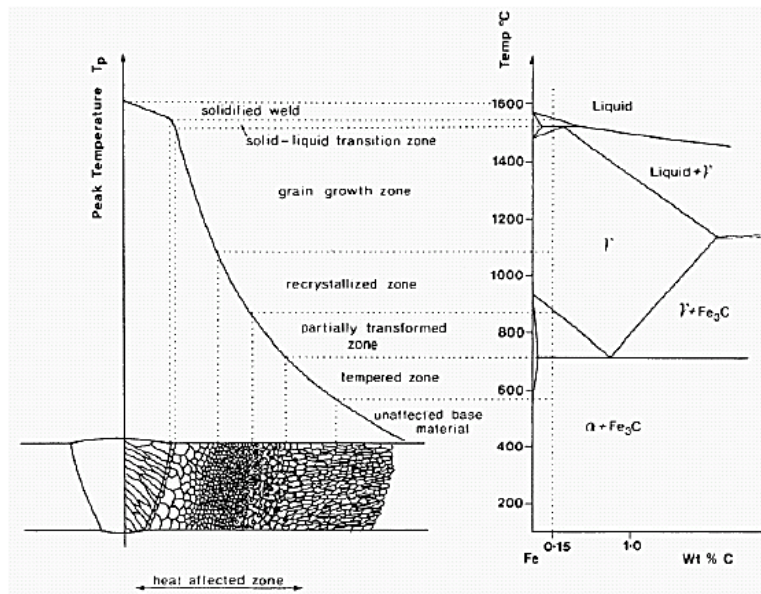


Figure 2-19: Peak temperatures and microstructural evolution of a weld zone [43]

### 2.2.1 Fusion Zone (FZ) and Weld Solidification Process

The FZ is the region where melting and solidification occur to form the joint/weld. The temperature within the FZ exceeds the liquidus temperature ( $>1500^{\circ}\text{C}$  for steel) and solidifies as heat is removed post weldment. The ability to form a serviceable joint is dependent on the material chemical composition and the circumstances of solidification. Solidification of a resistance spot weld pool is similar to that of metal casting, where solidification starts with the formation of nucleates (solid species within the liquid phase) within the weld pool and the continuation of liquid-to-solid transformation of crystal structure growth. The crystallization process is governed by heat dissipation of the weld pool into the surrounding, normally occurring by conduction. The initial solidification of the weld pool is that of epitaxial nucleation and growth, initializing at the liquid-solid interface, known as fusion boundary (FB) [44, 45, 46]. Grain growth is primarily columnar as the FB front moves forward for RSW. The evolution of grain growth within the weld pool is dependent on the temperature gradient and growth rate. As the solidification front forward into the weld pool, the temperature gradient (G) decreases while the growth rate (R) increases. The general

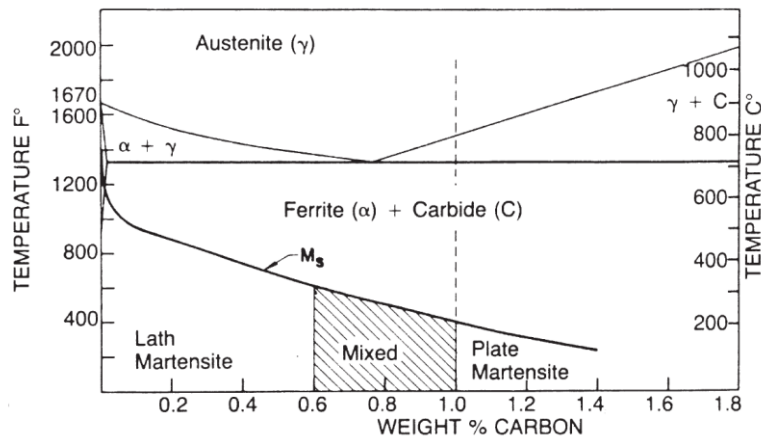
solidification mode undergo from planar > cellular > cellular dendritic > columnar dendritic as G/R decreases [45].

### **2.2.2 Heat Affected Zone (HAZ) and sub-zones**

The HAZ is a region of the base material (BM) where temperatures were not high enough to cause melting and solidification, but high enough for solid state transformations within the microstructure. Microstructural transformation within the HAZ is governed by local thermal cycle, resulting in heterogeneous regions. Based on different local thermal cycles, various zones of HAZ with different microstructures can be identified. The region adjacent to the FB (supercritical HAZ) can be sub categorized into two parts; the coarse grain (CG-HAZ) and fine grain (FG-HAZ). Temperatures experienced at the CG-HAZ is typically between solidus and homogenizing temperatures ( $\sim 1500^{\circ}\text{C} > T > \sim 1100^{\circ}\text{C}$ ), thus this region is also known as grain growth zone as initial segregations are eliminated and reformed from cooling during post weldment [47]. Below the grain coarsening temperatures and above the full austenite transformation temperature ( $A_{c3}$ ) lies the grain refined zone (FG-HAZ). Further away from the FG-HAZ lies a region that experiences partial phase transformation, also known as inter-critical (IC-HAZ). The temperatures experienced in this region vary between  $A_{c3}$  and the austenite start temperature ( $A_{c1}$ ). As a result, new phases that do not exist in the original base material may form, due to partial austenite transformation and subsequently quenched post weldment. The sub-critical HAZ (SC-HAZ) or tempered zone is a region where temperatures do not exceed  $A_{c1}$  and generally above martensite start temperature ( $M_s$ ). As a result this region does not normally show any major observable microstructural changes as temperatures are not high enough to cause any phase transformation. This region, however, generally contains the weakest microstructure since the region has been softened by sub-critical temperatures (tempered).

## 2.3 Ferrous Martensite

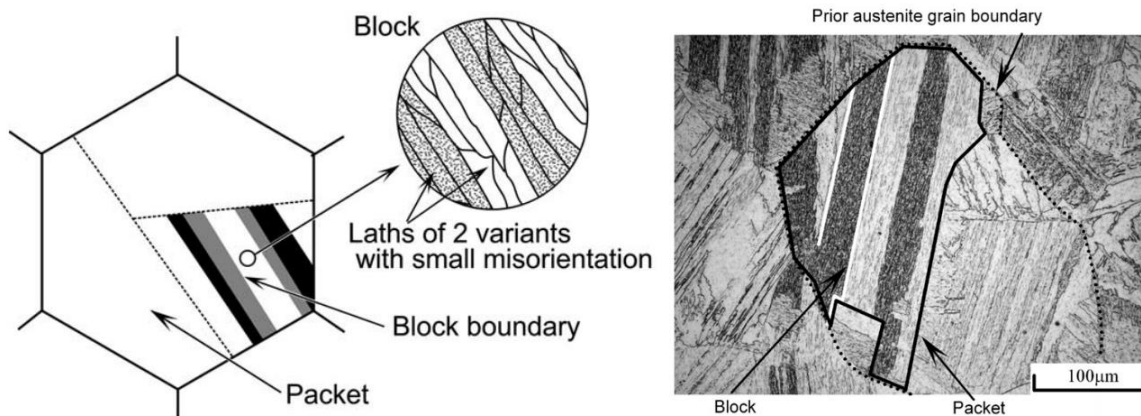
The term *martensite* was named after German metallurgist Adolf Martens. The name was first used to identify very hard, plate-like or acicular constituent produced in many steels that are rapidly quenched from austenite state [48]. Martensitic transformation is diffusionless (meaning that the chemical composition of the parent and product phases are identical) and occurs upon cooling at rates fast enough to suppress the diffusion-controlled transformation of austenite to ferrite, pearlite, and bainite. In martensitic transformation, neither iron atoms nor carbon atoms diffuse; therefore, the transformation occurs by shearing or the rapid bulk motion of atoms. Martensite is in the form of metastable body-center tetragonal (bct) structure, contrast to body-center cubic (bcc) of common steels at equilibrium state [48, 49]. The morphology and structure of, dependent of carbon content, ferrous martensite generally is in the form of plates or lath, or mixed structure (Figure 2-20).



**Figure 2-20: Effect of carbon concentration of the ranges of lath and plate martensite of iron-carbon alloys [48]**

In the case of hot-stamping steel, the martensite morphology is predominately lath martensite due to carbon concentration not exceeding 0.25wt%. Lath martensite is found in low to medium alloyed steels of carbon concentrations up to 0.6wt%. Martensitic lath structures are usually grouped together in differently oriented packets (or bundles) sharing identical orientation and habit plane. Within each packet,

small angle misoriented lath structure is differentiated into different blocks (appears as microstructures of different contrasts). The combination of blocks and packets forms within an austenite grain [48, 50, 51]. Figure 2-21 illustrates schematics and optical micrograph of a typical Fe-C alloy lath martensite structure.



**Figure 2-21: Lath martensitic structure schematics and optical micrograph [50, 51]**

### **2.3.1 Martensite Tempering**

In the as-quenched state, martensite has very high strength and hardness. It is a very useful material in specific areas requiring such characteristics; however, as-quenched martensite is also very brittle and requires heat treatment to increase ductility at the expense of strength. Heat treatment of martensite is generally known as *tempering*, by heating martensitic steel to a certain temperature (typically 250-700°C) below critical temperature  $A_{c1}$  for a specific period of time [52, 53, 54]. The tempering process involves overlapping stages of the following: the segregation of carbon to lattice defects and the precipitation of carbides, the decomposition of retained austenite (if any), and the recovery and recrystallization of the martensitic structure [52, 53]. Essentially, softening of martensite occurs with carbide nucleation and coarsening through carbon diffusion from the supersaturated martensitic structure to forms a mixture of ferrite ( $\alpha$ ) and cementite ( $Fe_3C$ ) phases. It should be noted that tempering is a diffusion process, thus

sufficient time must pass at selected temperatures for transformations to occur. Table 2-1 details the martensite tempering transformations at each stage, associated with different temperature ranges.

**Table 2-1: Stages of Tempering [52, 53]**

Temperature	Transformation
T1: (100 – 250°C)	Decomposition of supersaturated martensite to transition carbide, epsilon( $\epsilon$ )-carbide and low carbon martensite ( $\alpha''$ )
T2: (200 – 300°C)	Decomposition of retained austenite (if present) to bainite
T3: (250 – 350°C)	Transformation of bct martensite ( $\alpha''$ ) into Ferrite ( $\alpha$ ) and cementite ( $\text{Fe}_3\text{C}$ ) constituents
T4: (>350°C)	Spheroidization of cementite
T5: (>350°C) Alloyed steel	Intermetallic precipitates and alloy carbides

### 2.3.2 Rapid Tempering

Tempering is generally accomplished by isothermal heating with sufficient soaking period up to numerous hours in order to attain desired steel attributes. However, thermal histories of a spot weld are rapid and softening can still be observed specifically within the HAZ regions, regardless of the absence of prolonged dwell times. Cvetkovski *et al.*, observed an initial large drop in hardness of martensitic structure within the first tenth of a second when laser tempering martensitic medium carbon steel. Limited softening was observed for longer temper times [55, 56, 57]. Simply stated, the initial softening of martensite is related to carbide nucleation and is dependent on specific temperature levels (activation energy), whereas, subsequent softening is due to carbide coarsening when enough tempering time has passed for diffusion.

The morphology of carbide (cementite) formation within martensite subjected non-isothermal tempering do differ to isothermal tempering. Baltazar *et al.*, have observed that during that non-isothermal tempering of martensite, fine cementite formation was attributed to combined effect of delay in cementite precipitation and insufficient time for diffusion of carbon due to high heating/cooling rates. As such, there was not enough time for third stage (T3) tempering where cementite coarsening and recrystallization occur

[58]. Figure 2-22 illustrates of fine inter and intra-lath cementite formation of a martensite sub-structure subjected to non-isothermal tempering, comparing to fully spheroidized cementite and complete grain recovery after isothermal tempering.

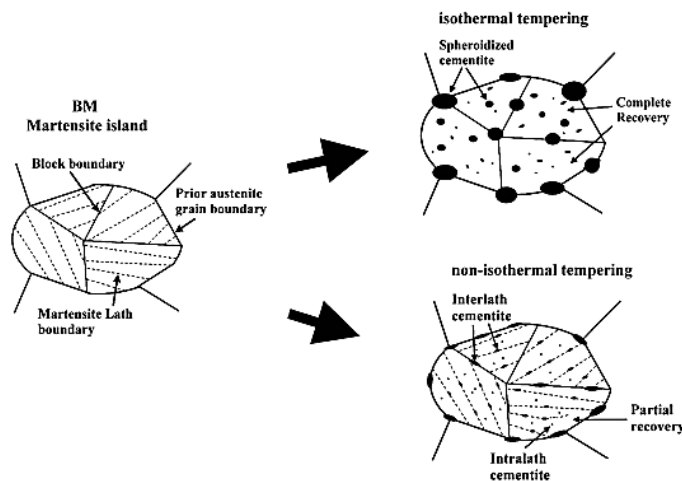


Figure 2-22:  $Fe_3C$  formation within martensite subjected to isothermal and non-isothermal tempering [58]

## 2.4 USIBOR 1500P

USIBOR 1500P, trade named by ArcelorMittal, is a 22MnB5 grade boron alloyed steel coated with Al-Si coatings for hot-stamping process. The intended use of USIBOR 1500P is for automobile structural and safety component by offering very high mechanical strength of the final part, while achieving weight savings of 30% to 50% compared to conventional cold forming grade steels [8].

Hot stamping is a non-isothermal forming process, where forming and quenching takes place in one combined process. There are two main variants of hot-stamping; direct and indirect hot stamping method as illustrated in Figure 2-23. Direct hot-stamping involves the heating steel blanks above  $A_{c3}$  temperature and soaked for a given amount of time (typically 900-950°C for 4 to 10 minutes) in an open-atmosphere furnace, transferred to the press, and subsequently formed and quenched in the closed tool. In-

direct hot-stamping involves an extra step of cold pre-forming part to near completion and then normal hot-stamping procedure for final part geometry calibration [10, 8, 59, 60, 61].

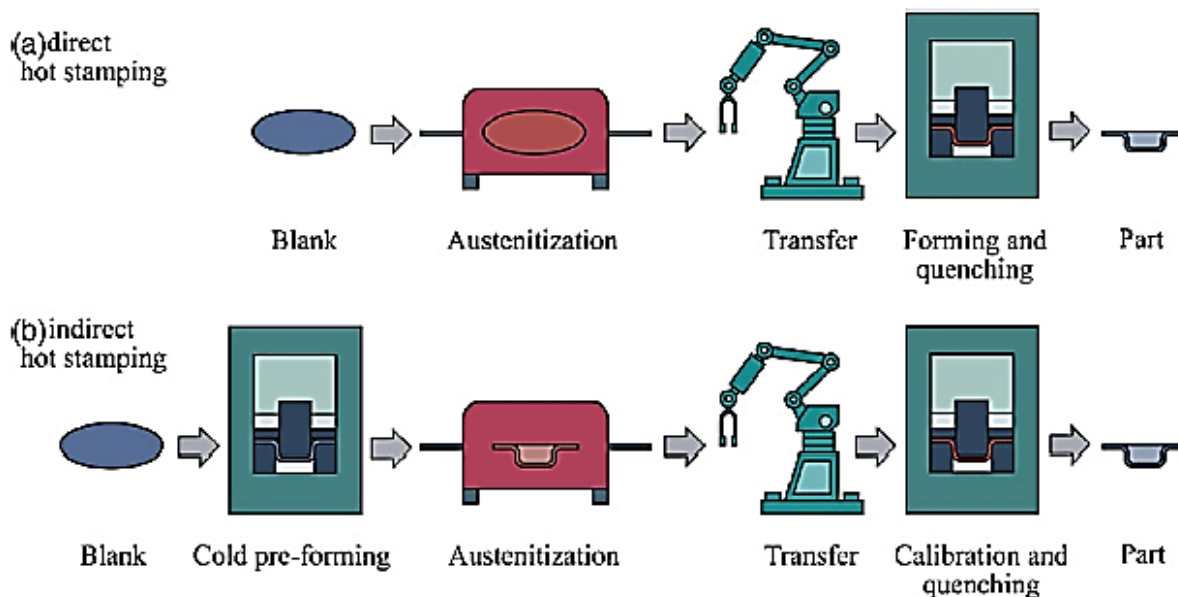


Figure 2-23: Hot Stamping Process: a) direct hot stamping, b) indirect hot stamping [10]

### 2.4.1 Hardenability and Critical Temperatures

The high hardenability (ease to form martensite) characteristics of USIBOR 1500P is a result of added alloying elements, with the major effect contributed by the addition of boron (B). 22MnB5 hot-stamping grade steels generally have chemical compositions of main alloying elements of 0.19-0.25wt% C, 1.1-1.4wt% Mn, and 0.0008-0.005wt% B [62]. Details of specific chemical composition of the USIBOR sheets used for experiments will be discussed in the following section. The effects of main alloying elements are as follows:

## **Carbon**

Carbon is the main hardening element in all steels. Tensile strength, hardness, and hardenability increase as carbon content increases up to 0.85% (hypoeutectoid limit). Beyond 0.85%, toughness, ductility, and weldability decrease considerably [63].

## **Manganese**

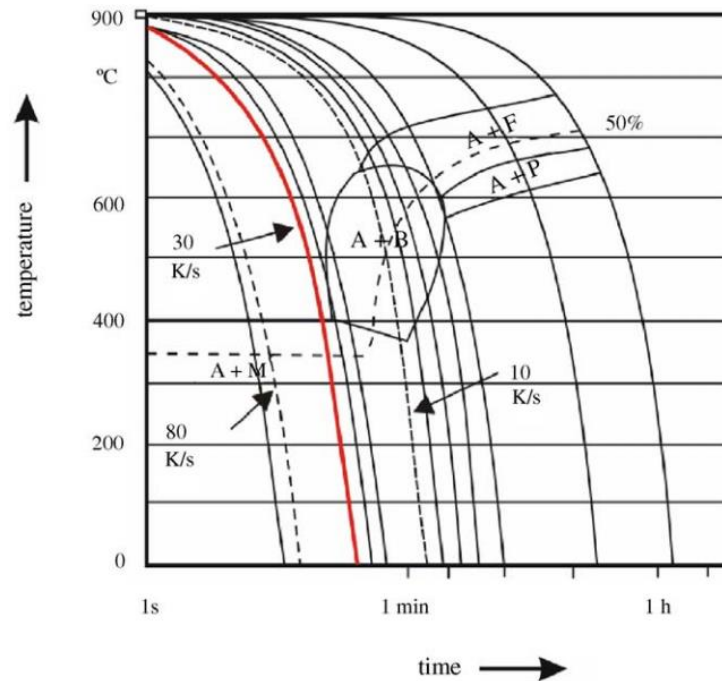
The general purpose of manganese (Mn) as alloying element in steel serves as a deoxidizer and desulfurizer. Addition of Mn aids the lesser tendency of macro-segregation and hot shortness by elimination of iron sulfides. Mn is also a solid-solution strengthener in steel and is very effective in increasing hardenability [63].

## **Boron**

Addition of boron (B) in very small amounts (0.001 to 0.003%) has startling effect on hardenability for steels. Boron also improves hardenability of other alloying elements, with 0.003wt% B contribution to increased hardenability being equivalent to 0.5wt% of elements such as Mn, Cr, and Mo. Boron as a hardenability agent, is however, limited to steel containing less than 0.4%C and its effect decreases with increasing carbon content [63].

Figure 2-24 is a continuous cooling transformation diagram of USIBOR 1500P. The diagram illustrates the different expected phases that will exist within the microstructure, depending on the cooling rate, when cooling the steel from fully homogenized state. Within the diagram, A represents austenite, B is bainite, F is ferrite, M is martensite, and P is pearlite (fine laminar structure of ferrite and cementite mix). The critical cooling rate for martensitic transformation of USIBOR 1500P is around 30K/s.





**Figure 2-24: Continuous Cooling Transformation (CCT) Curve and Critical Cooling Rate [59]**

Critical temperatures of steels differ depending on the chemical composition. The austenizing temperatures ( $Ac_1$  and  $Ac_3$ ) can be calculated with the following equations developed by E. Miyoshi [63]:

$$Ac_1(^{\circ}C) = 751 - 26.6C - 11.1Mn - 22.9Cu - 23.0Ni + 17.6Si + 24.1Cr + 22.5Mo - 39.7V + 223Nb - 169Al - 895B \quad \text{Eqn. 5: E. Miyoshi } Ac_1 \text{ Temperature Equation}$$

$$Ac_3(^{\circ}C) = 937 - 476C - 19.7Mn - 16.3Cu - 26.6Ni - 4.9Cr + 56Si + 38.1Mo + 12.5V - 19Nb + 198Al + 3315B \quad \text{Eqn. 6: E. Miyoshi } Ac_3 \text{ Temperature Equation}$$

The temperatures are measured in degree Celsius, with alloying elements in wt% concentrations. Calculated  $Ac_1$  and  $Ac_3$  temperatures are 730 and 831°C respectively. The martensitic start temperature ( $M_s$ ) can be calculated with the following semi-empirical equation developed by Andrews [52]:

$$M_s(^{\circ}C) = 539 - 423C - 30.4Mn - 17.7Ni - 12.1Cr - 7.5Mo + 10Co - 7.5Si \quad \text{Eqn. 7: K. W. Andrews } M_s \text{ Temperature Equation}$$

The  $M_s$  temperature is roughly 400°C for USIBOR 1500P. The martensitic finish  $M_f$  temperature is dependent on cooling rates, thus it cannot be calculated with an equation and has to be measured empirically. According Suehiro *et al.*, the  $M_f$  temperature at 30K/s cooling rate is roughly between 200 and 300°C (Figure 2-25)

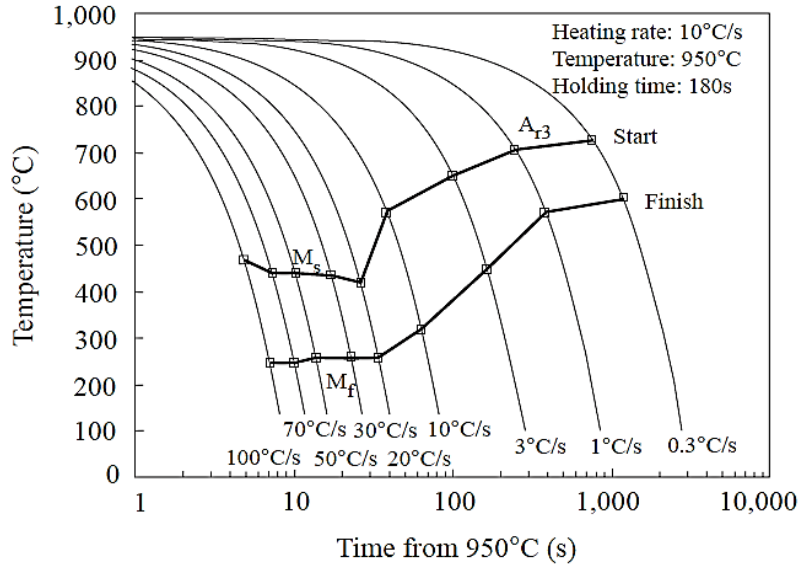
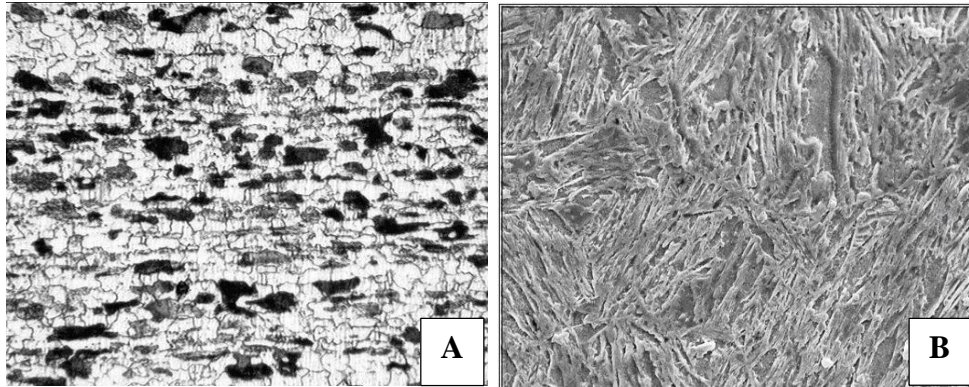


Figure 2-25:  $M_s$  and  $M_f$  temperatures of 22MnB5 grade hot-stamping steel at various cooling rates [60]

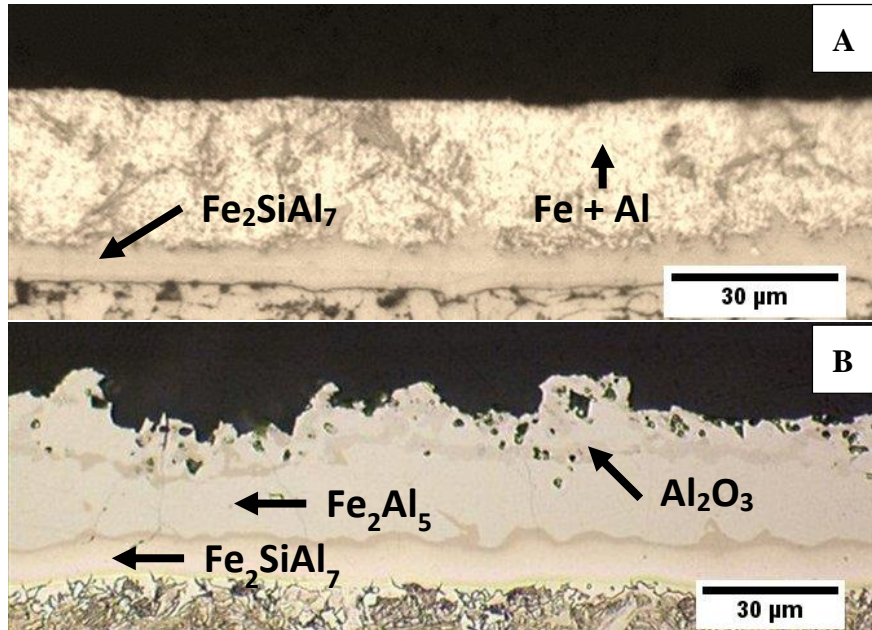
#### 2.4.2 Base metal and coating morphology

USIBOR 1500P in its as-delivered state exhibits ferritic-pearlitic microstructure (Figure 2-26a) with a tensile strength about 600 MPa and fracture elongation greater than 10%. After hot-stamping, the microstructure becomes fully martensitic (Figure 2-26b) with strength reach up to 1500 MPa; however, elongation is decreased to 6% [8].



**Figure 2-26: USIBOR 1500P Morphology: A) As-delivered and B) Hot-stamped [8]**

In a typical hot-stamping process, the heating of the steel takes place in open atmosphere furnaces (containing oxygen). Bare steels become oxidized and decarburized when heated up to austenizing temperatures, thus protective coatings are applied to steels to prevent these two phenomena. USIBOR 1500P is most commonly hot-dipped into a molten Al alloy bath with a composition of approximately 88wt% Al, 9wt% Si, and 3wt% Fe, at 675°C [61]. There are two main layers of coating for the as-delivered steel (Figure 2-27a). The upper layer consists of biphasic eutectic aluminium and silicon. The layer below is an inhibition layer of  $\text{Fe}_2\text{SiAl}_7$  intermetallic layer that was formed during the hot dip process [61, 64]. The melting temperature of the coating is roughly 580-600°C and the typical thickness of the aluminized coating is 25-30  $\mu\text{m}$ .



**Figure 2-27: Al-Si Coating Morphology: A) As-delivered and B) Hot-stamped [8]**

During hot-stamping, the heating temperature above 900°C triggers Fe-Al reactions causing the coating to be enriched with Fe through diffusion, forming a wavy layer of hard and brittle  $\text{Fe}_2\text{Al}_5$  phase as well as other Fe-Al intermetallic. The most topmost part of the coating is an  $\text{Al}_2\text{O}_3$  oxide layer, which serves as an oxidation protection layer when the metal is heated in the furnace [61, 64].

### 2.4.3 Resistance Spot Weldability and Weld Performance

#### 2.4.3.1 Weldability of USIBOR 1500P

As discussed previously, one of the major challenges of USIBOR is narrow weldability window. There are two factors contributing to this phenomenon, the effect of added alloying elements for hardenability and effects of protective coating type. Kong *et al.*, examined the effects of alloying elements having on electrical resistance for welding uncoated AHSS. His observation indicated that electrical conductivity decreased linearly with increasing alloying elements (meaning higher electrical resistance)

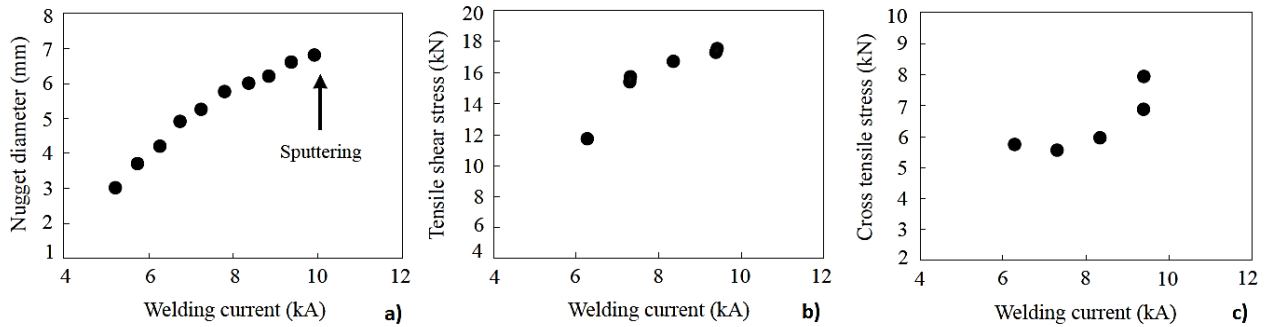
within the steel [11, 65]. The increase of resistivity contributed to higher tendency of weld expulsion due to rapid weld pool growth.

The other contributing factor is due to the protective coating. Studies have indicated that the development of Al-Si-Fe intermetallic during the hot stamping process has negative impact towards welding stability. Ji *et al.*, investigated that the coating intermetallic layers have high melting temperature (over 1160~1500°C), resulting in slow initial weld pool generation [28, 66]. As such, elevated welding current is required in order to break through the coating to create a weld. In addition, Al-Fe intermetallic coating transforms into a liquid film during weldment and is squeezed out into the periphery creating a conductive large corona bond consisting of re-solidified intermetallic layer, resulting in large current paths in the periphery, ultimately lowering current density. Schmidova *et al.*, investigated the effects of increased intermetallic layer due to prolonged soaking time during hot-stamping process. It was found that over-abundance of intermetallic layer creates instability to the welding process due to higher amount of pores from increased oxide layer, thus causing irregular current flow [67]. The combination of slow weld pool generation due to high melting temperature of coating intermetallic and rapid weld growth due to high resistivity from added alloying elements, resulted in narrow band of weld-able current range for RSW. As a result, multi-impulse current wave forms are used to better control weld nugget growth [12].

#### 2.4.3.2 Mechanical Performance and nugget hardness profiles

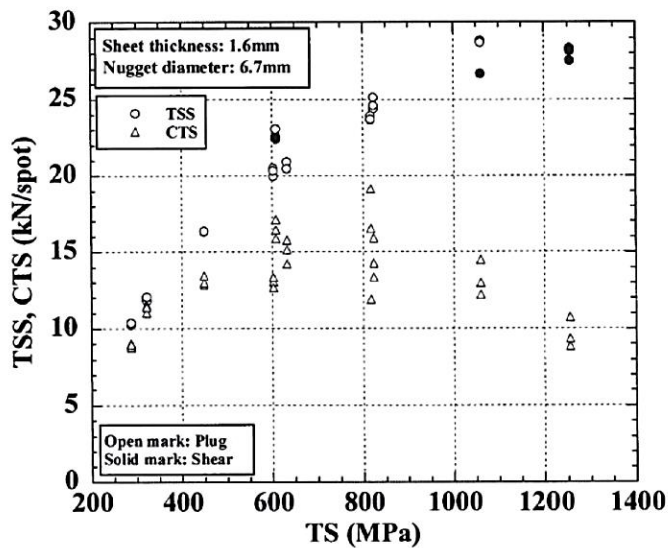
Weld strength of an optimally welded spot weld for USIBOR 1500P generally exceed minimum requirement as required by AWS by a large portion. Suehiro *et al.*, recorded that a single 7mm diameter weld has tensile shear strength as high as 18kN and cross tensile strength as high as 9kN. Figure 2-28 illustrates comparison plots of applied welding current vs nugget diameter, tensile shear strength, and cross tensile strength. It should be noted that there is a proportional increase in nugget diameter to tensile shear strength. However, cross tensile strength did not exhibit the same trend as the weld strength remained

constant from 6-9kA welding and spiked up around 10kA [60]. The change in CTS trend can be explained by fracture behavior caused by weld characteristics for USIBOR welds.



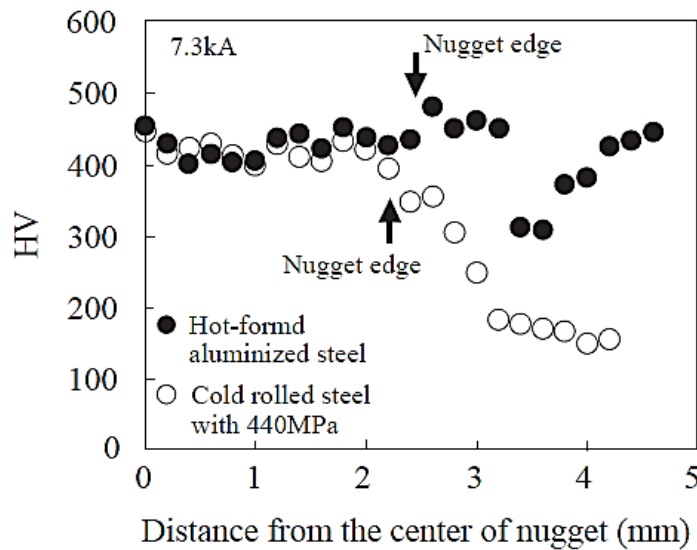
**Figure 2-28: USIBOR RSW weld quality vs current: a) nugget diameter, b) tensile shear strength, c) cross tensile strength [60]**

Furusako *et al.*, explained that the trend illustrated in Figure 2-29 was due to increasing in stress concentration at the nugget edge (corona bond area), thus nugget ductility and toughness decrease with increasing base metal strength.



**Figure 2-29: Effect of base metal strength on TSS and CTS of spot welded joints [68]**

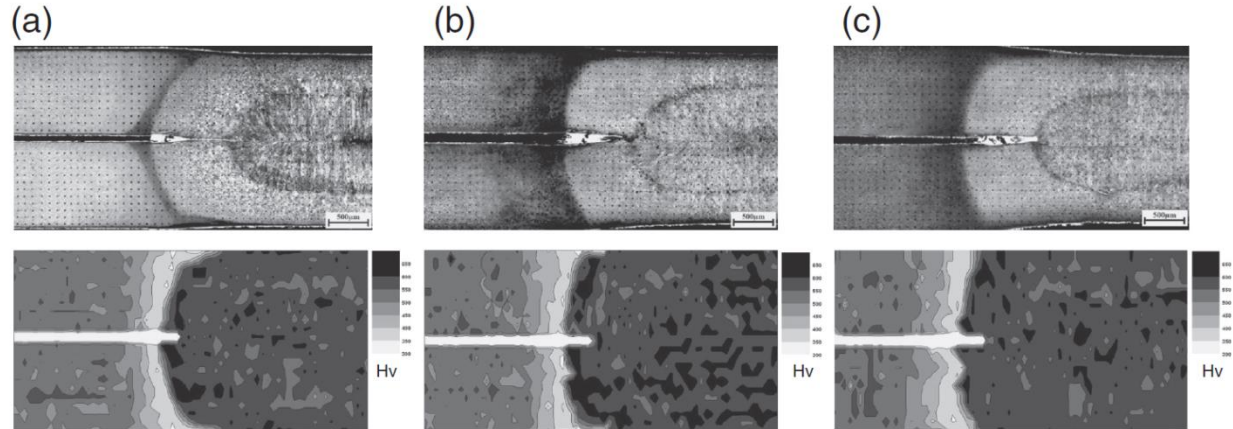
Furusako further expanded that the increase in nugget hardness due to enhancement of hardenability is the result for increased notch stress concentration, promoting high tendency for interfacial failure modes. This phenomenon can be further reinforced with hardness map comparison between hot-stamping steel and cold rolled steel spot weld (Figure 2-30). It can be noted that hardness of the nugget remained consistent beyond nugget edge (fusion boundary) until a sharp drop of hardness at the SC-HAZ. The hardness profile for the cold rolled steel exhibited very differently, with hardness gradually decreasing beyond the nugget edge [60].



**Figure 2-30: HF steel vs low carbon steel nugget hardness [60]**

Jong *et al.*, reinforced this with detailed hardness map of the entire nugget area as illustrated in Figure 2-31. Regardless of applied weld current, hardness from the FZ all the way ICHAZ remain fairly consistent. It should be noted that hardness specifically near the corona bonds (faying interface) has a similar hardness as well [65]. Additionally, Schmidova *et al.*, has also indicated that the presence of re-melted brittle intermetallic phases of the Al-Si coating residue within the corona bond after weldment has harmful effect on fracture behavior, also promoting interfacial weld failures [67].





**Figure 2-31: Microstructure and corresponding hardness mapping of boron alloy steel spot welds for welding currents of: a) 4kA, b) 6kA, and c) 8kA [69]**

#### **2.4.4 In-Process Tempering Methodologies**

Studies have attempted in-process tempering methodologies to improve CTS and/or modify failure mode for USIBOR or martensitic steel welds. Chuko and Gould, explored the tempering response of DP690 and DP960 steels with the application of an in-process quench temper welding scheme. The temper time and current relationship was empirically mapped out with temper time measured in cycles and percentage of expulsion current for applied power. They presented the effectiveness of tempering with recorded Rockwell hardness performed on the weld surface. Chuko and Gould concluded that tempering response is most robust with 30 cycles of tempering time and 70~80% of expulsion current [70]. Diallo *et al.*, explored the improvement CTS with utilization of similar tempering scheme on various grades of boron steels. A 1.2s quench time and 0.6s temper time was kept constant for tempering comparison. Optimal tempering current was found to be within the range of 60-80% of max welding current and the optimal welding current for initial nugget development was found to be around 8kA [14]. It should be noted that weld energy absorption has not been fully explored in both cases and will be discussed in depth in the following chapters.



# Chapter 3

## Experimental Methods

### 3.1 Materials

All experiments were carried out with 1.2mm and 1.5mm thick USIBOR 1500P, supplied by ArcelorMittal Dofasco, Hamilton Canada. Table 3-1 documents the chemical composition of the USIBOR sheets used. Welding experiments were done on the USIBOR sheets for both as-delivered and hot-stamped conditions.

1. As-delivered coated welds for in-direct hot-stamping experiment was done on 1.2 to 1.5mm stack-up with the thinner sheet on top for better heat balance and to counter act with Peltier (thermoelectric) effects from the MFDC machine.
2. The hot-stamped sheet weld experiment was done on 1.5 to 1.5mm stack-up. The hot stamping process was performed by heating the blanks up to 930°C and soaked for 4 minutes in a front loading open atmosphere furnace and then subsequently flat stamped and quenched at 450kN of force with a 250T hydraulic press (Figure 3-1).



Figure 3-1: UofWaterloo Hydraulics Lab - Mini Macrodyne Press and Front Loading Furnace

**Table 3-1: USIBOR 1500P Chemical Composition**

Steel Grade	Thickness [mm]	Coating, wt-%			Base Metal, wt-%								
		Type	Al	Si	C	Mn	P	Si	Cr	S	Al	B	Ti
22MnB5	1.2 & 1.5	Al-Si	90	10	0.23	1.22	0.013	0.21	0.2	0.002	0.041	0.0027	0.032

### 3.1.1 Mechanical Properties

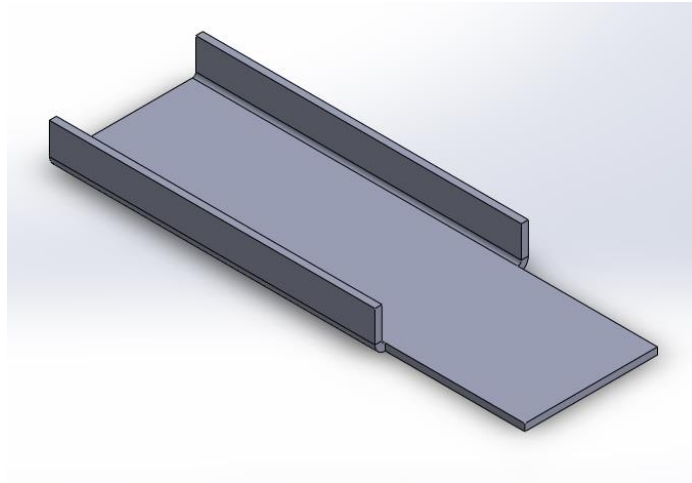
The experimentally determined uniaxial tensile properties: elastic modulus (E), 0.2% yield strength (YS), ultimate tensile strength (UTS), and % elongation of USIBOR 1500P in both as-delivered and hot-stamped conditions are listed in Table 3-2. The mechanical properties listed in the table correlated well with literature review.

**Table 3-2: USIBOR 1500P Material Property**

Condition	E [GPa]	0.2% YS [MPa]	UTS [MPa]	Hardness [HV]
As-Delivered	213	422	570	190
Hot Stamped	199	1250	1600	520

### 3.1.2 Specimen Dimensions

Metallographic coupons of all weld experiments were done on 30x100mm sheets regardless of material thickness and surface conditions. This specimen size was also selected for TST in contrast of the 60x138mm, recommended by AWS standard. This was due to the limited amount of USIBOR sheet material available for the research, as such the sample dimensions were minimized in order to save as much material as possible. Weld rotation during TST for hot-stamped USIBOR sheets was negligible with the 30x100mm coupons. On the contrary, TST on as-delivered USIBOR welds suffered significant joint rotation; therefore, the TST specimens were slightly modified to have flanges along the majority of the length in order to increase stiffness. Figure 3-2 illustrates the geometry of the flanged coupons used for as-delivered USIBOR weld TST.



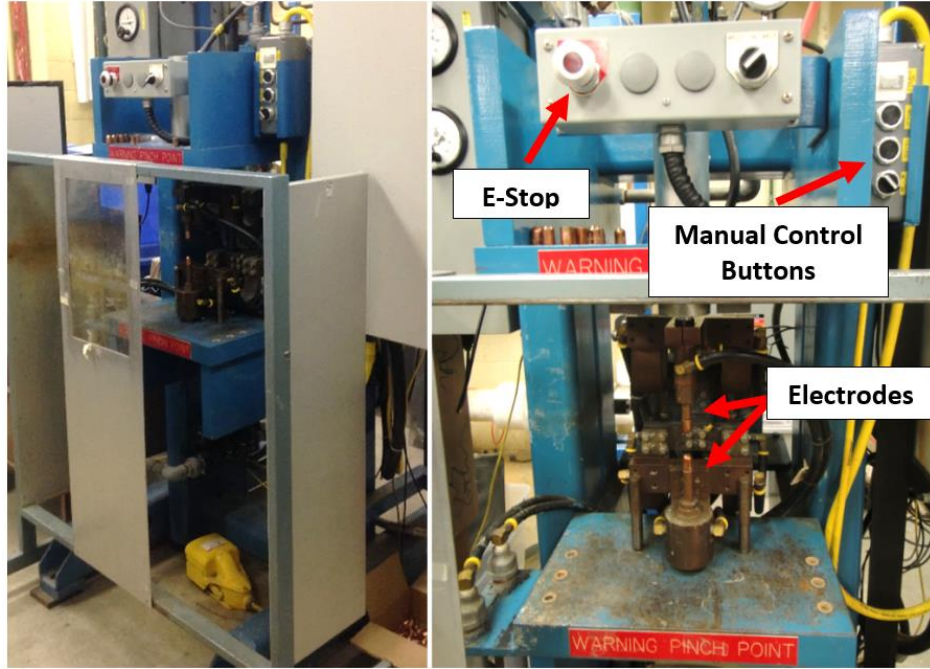
**Figure 3-2: Modified flanged tensile shear specimen**

Specimen dimensions for CTT were based on AWS standards at 150x50 with 20mm mounting holes at designated locations. Schematics of TST and CTT will be discussed in detail in the next section.

## **3.2 Resistance Spot Welding**

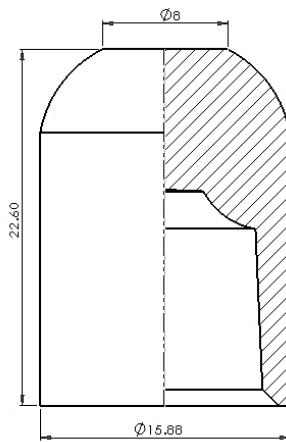
### **3.2.1 Equipment**

Welding experiments were conducted using a pedestal-type, pneumatically controlled, 144/180-kVA medium frequency direct-current (MFDC) resistance spot welder. The welder has a maximum constant current capacity at 60kA and electrode load capacity at 25kN. Weld schedule controls were performed by an upgraded computer-welder interfacing controller (GeniusHW I) from Harms & Wends and the interface software used was Harms & Wende XPegasus Gold edition V3.1.10. The welder is fully equipped with data acquisition (DAQ) system, built into the GeniusHW I controller, capable of recording weld current (kA), voltage (V), and resistance ( $\Omega$ ) as a function of time and is displayed via the XPegasus Gold software.



**Figure 3-3: MFDC Spot Welder**

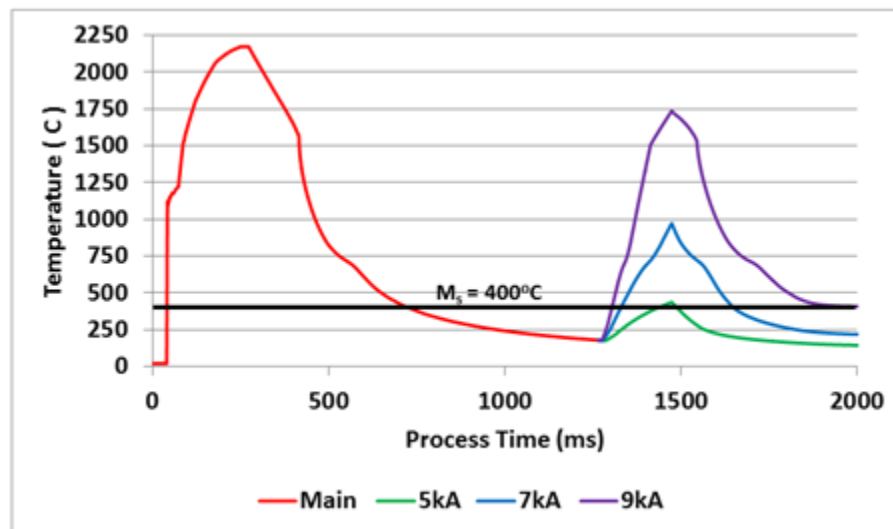
The electrodes used for welding in the present work are the RWMA CLASS II electrodes. The electrode surface contact diameter is 8mm as specified by AWS D8.1M for group 4 (tensile strength >800MPa) steels at 1.5mm in thickness. The geometry of the electrodes are dome shaped (B-Type) commonly used by Honda Automotive.



**Figure 3-4: RWMA CLASS II 8mm electrode schematics**

### 3.2.2 Welding Procedure

Preliminary welding scheme optimization was done by simulation with SORPAS Enterprise 2D version, standing for **S**imulation and **O**ptimization of **R**esistance **P**rojection And **S**pot welding processes [71]. SORPAS simulation was performed for weldability lobe as well as processing profile curves such as dynamic resistances and thermal profiles. The quench-temper welding profile used for all welding experiments was based from the welding scheme used by Gould and Diallo. The quench period prior to tempering pulses was kept constant at 1 second (60 cycles) and is verified with simulated thermal profiles. Figure 3-5 illustrates simulated thermal profile of the weld pool after one second quench period (red).



**Figure 3-5: Preliminary simulated weld thermal profile for tempering scheme optimization**

The welding schemes for the different experiments of each following chapters:

1. As-delivered, coated steel experiment for in-direct hot-stamping project,

**Table 3-3: As-delivered coated welding scheme - for in-direct hot-stamping application**

Electrode Force [kN]	Schedule [kA, cycle @ 60Hz]						
	Squeeze	Pulse 1	Cooling 1	Pulse 2	Cooling 2	Pulse 3	Hold
4.4	70	16, 7.2	2	8, 16	60	50-70% Max I, 30	10

- Hot-stamped steel experiment for direct hot-stamping project.

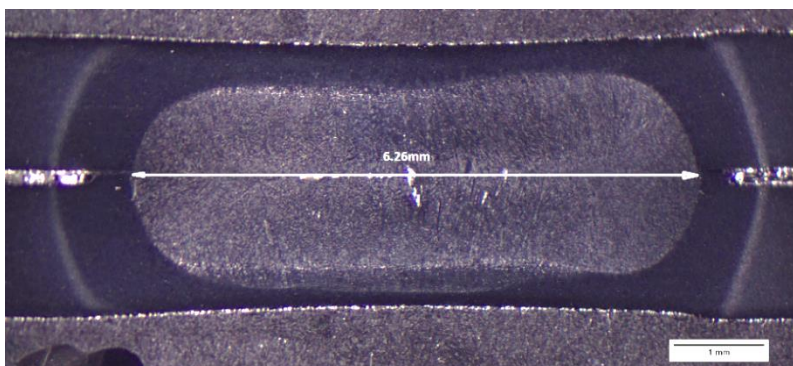
**Table 3-4: Hot-stamped welding scheme - for direct hot-stamping application**

Electrode Force [kN]	Schedule [kA, cycle @ 60Hz]						
	Squeeze	Pulse 1	Cooling 1	Pulse 2	Cooling 2	Pulse 3	Hold
5	70	6.5, 12	4	6-9, 16	60	50-70% Max I, 30	10

All of the welding schemes listed in the above tables utilizes the electrode mentioned previously and water cooling is regulated at 20°C and a 6L/min flow rate.

### 3.2.3 Weld Size Measurement

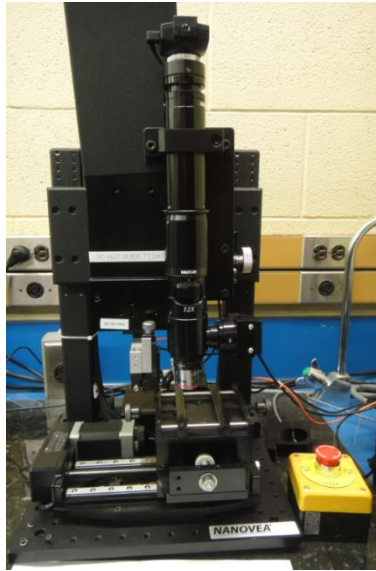
Weld size measurements was mainly performed from metallographic cross-sections of the weld nugget by imaging analysis with digital micro stereoscopy (magnification range from 2 to 5x). Figure 3-6 is a sample weld cross-section illustrating the fusion zone and measured weld size.



**Figure 3-6: Weld size measurement by metallographic inspection**

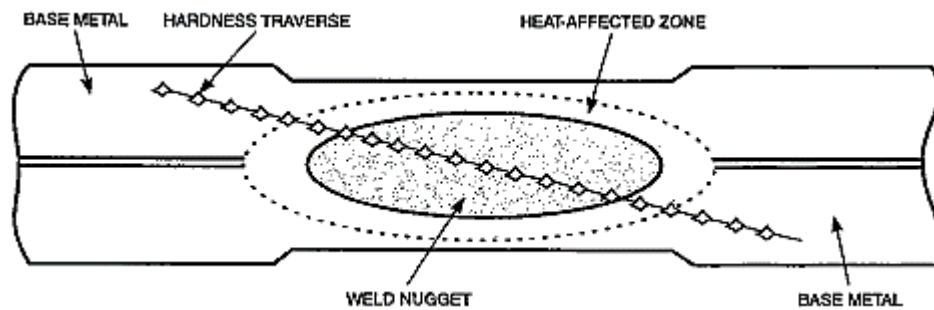
### 3.2.4 Vickers Hardness Testing

Vickers micro hardness testing was performed on cross-sectioned welds on an automated micro-hardness indentation platform, Nanovea CB500.



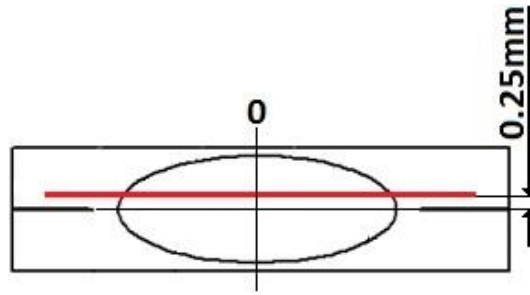
**Figure 3-7: Nanovea CB500 automated micro-indenter**

Two different hardness mapping profiles were performed on weld cross-sections: general AWS specified indentation map for nugget analysis, and modified straight-line indentation map for faying area hardness observations.



**Figure 3-8: AWS specified micro-hardness mapping [17, 18]**

AWS specified hardness mapping was performed with 0.5kg load and each indent is spaced at 0.5mm spacing, with indenter dwell time kept at 15 seconds.



**Figure 3-9: Modified straight line micro-hardness map for faying line hardness analysis**

The modified hardness map has the indentation line offset by 0.25mm from the faying surface line. The indentations were spread across 15mm in length from the left and right portions weld nugget, centered at the nugget center line. The indentations were 0.5mm spaced and indented with 1kg load and dwelling at 15 seconds each.

### **3.2.5 Tensile Testing**

TST and CTT were used to characterize mechanical properties of the welds. The tensile test were conducted at 10mm/min strain rates as recommended by AWS standards. The tensile tests were conducted with MTS 880 hydraulic tensile tester with capacity of 100kN. TST for as-delivered USIBOR sheet welds were done on the modified specimens as discussed earlier and hot-stamped USIBOR sheets welds done on the 30x100mm coupons. TST setup used can be seen in Figure 3-10. CTT for both as-delivered and hot-stamped USIBOR sheet welds were conducted as per AWS standard. Figure 3-11 illustrates the test setup.



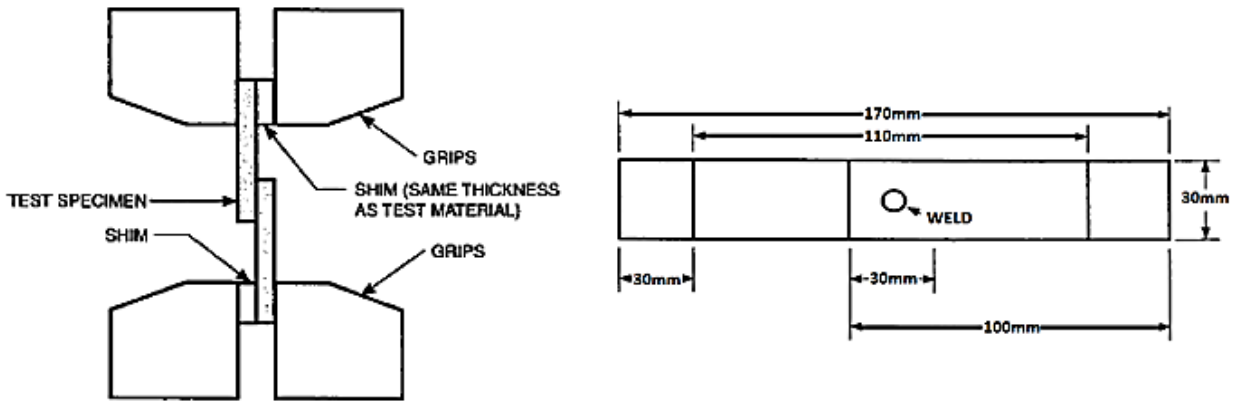


Figure 3-10: Tensile shear test setup: schematics and specimen layout [17, 18]

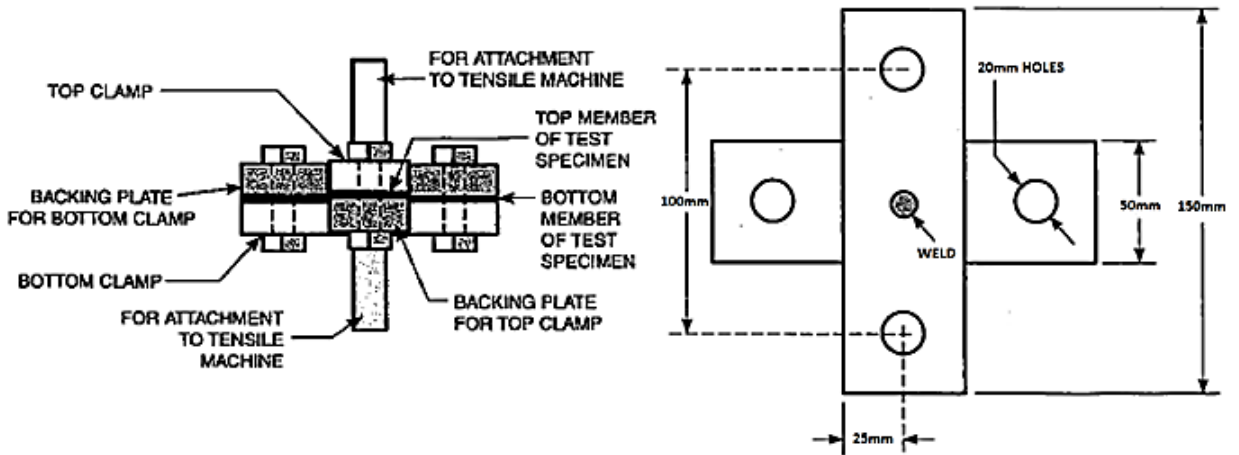


Figure 3-11: Cross tensile test setup: schematics and specimen layout [17, 18]

### **3.3 Metallographic Characterization**

Metallographic cross-section samples were prepared and weld microstructure was examined by optical microscopy (OM) and scanning electron microscopy (SEM) characterization techniques.

#### **3.3.1 Sample Preparation**

Weld specimens for microscopy were cross-sectioned paralleled to the rolling direction of the steel sheet for the as-delivered and hot-stamped sheets. The cross-sectioning is done with precision abrasive sawing, and the weld cross-sections were hot mounted in carbon infused phenol bakelite®. The mounted samples were mechanically ground and polished with diamond suspended lubricant from 6um to 0.5um particle size. Metallographic etching of the specimens were done with 1.2% ( $C_6H_3N_3O_7$ ) aqueous picric solution for prior-austenite grain boundaries observations (weld pool), and 2% ( $HNO_3OH$ ) Nital etching for 2-4 seconds for general OM and SEM procedures.

#### **3.3.2 Microscopy**

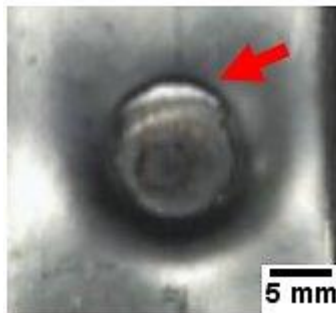
Optical microscopy was performed on Olympus BX51M coupled with image analysis software QCapture Pro Ver. 5.1. All OM was done on bright field imaging at magnification range from 50 to 1000x. Snapped microscopic images were processed and analyzed with QCapture Pro Ver. 5.1. SEM was performed on Zeiss Leo model 1550. All SEM imaging is done at 10kV electron volt at 10mm working distance. Selected imaging magnification range was 5000 to 50000x.

## Chapter 4

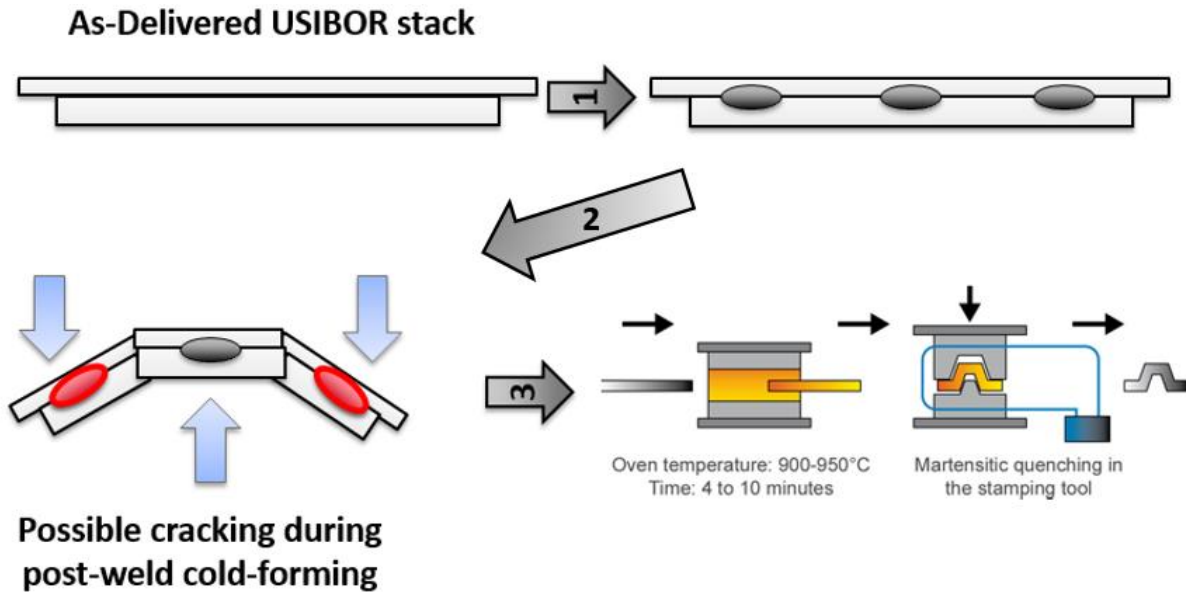
### RSW and In-Process Tempering of As-Delivered USIBOR Sheets

In this chapter, in-process tempering was applied to the fusion zone of welds in as-delivered USIBOR sheets (without heat treatment or stamping performed), which would be used for in-direct hot stamping applications. The indirect hot stamping process involves the addition of a cold pre-forming process of the component up to nearly the final geometry (up to 90 to 95% of its final shape) and finally hot-stamped (heated and stamped) to the final geometry. Indirect hot stamping is generally employed for producing components with very complex shapes, where additional forming operations are required.

One particular case of indirect hot stamping of USIBOR sheets involves localized strengthening of a U-channel column by welding a reinforcing patch to the main forming blank. This reinforcement method is known as tailor welded patching (TWP). RSW was chosen as the joining method of attaching the reinforcing patch, where the patch was welded to the main forming blank prior to the cold forming process. After cold forming, crack opening around the nugget, perpendicular to direction of the stretch (Figure 4-1) can be observed. The failures are exclusively located at welds on the side flanges. Figure 4-2 is a schematic illustrating in-direct hot stamping of TWP component and the effected welds.

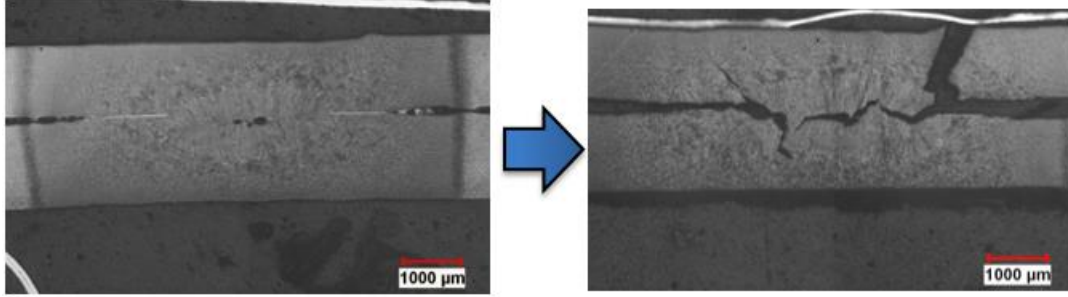


**Figure 4-1: As-delivered USIBOR weld: base material tearing around the nugget (red arrow) after cold forming**



**Figure 4-2: Tailored welded patch for indirect hot-stamping schematics: side flange weld failure (red) of a U-channel due to localized weld shear before final hot stamping operation [8]**

Based on the characteristics of weld failure, it was determined that the failures were due to shear overload of a rigid nugget in a ductile base material, identical to fracture propagation associated with TST. Further observations through optical microscopy of weld cross sections indicated that the fracture can occur through the weld interface and/or through the sheet thickness, where the initial quality of the weld nugget played an important role. The observations dictated that RSW nuggets in the as-delivered USIBOR sheets suffer from the same low nugget ductility as the hot-stamped versions. As a result, it is of particular interest to determine whether weld tempering can exhibit higher ductility during intermediate cold forming operations which may be required in preparing tailor welded hot-stamping blanks.



**Figure 4-3: Weld fracture of As-delivered USIBOR welds after cold forming: weld fracture through the interface and sheet thickness [72]**

Welding scheme optimization for as-delivered USIBOR welds was performed to establish a baseline nugget to evaluate the effectiveness of the tempering. Initial weld challenges related to lack of fusion due to the presence of the Al-Si coatings was addressed by the addition of a pre-pulse current. Similar weld tempering profiles from literature were applied for weld tempering and the pre-tempering solidification period was simulated with SORPAS 2D to ensure full solidification. Evaluation on the level of tempering was achieved by comparison of weld Vickers micro-hardness profiles of weldments subjected to varying tempering levels with isothermally tempered (furnace tempered) and non-tempered nuggets.

Joint performance was assessed by both cross tensile (CTT) and tensile shear tests (TST) at quasi-static strain rates. The effects of joint performance (particularly joint strength) of tempered welds of varying tempering levels are compared with a baseline non-tempered weld nugget. Corresponding tensile data and hardness profiles were cross examined to select the best performing welding and tempering scheme. Finally microstructural evolution of tempering was observed and analyzed to explain the effects of microstructural changes with the application of tempering pulses.

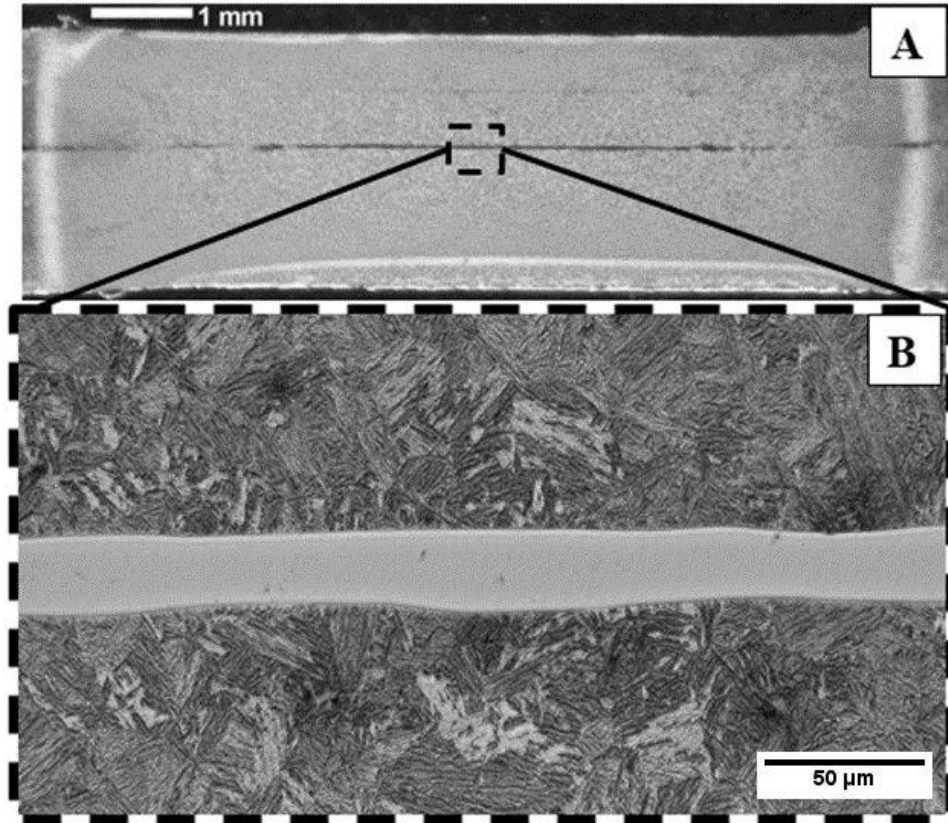
The experiments associated in this chapter serve as preliminary proof of concept for the effect of in-process tempering of USIBOR spot welds. Actual cold forming operations for in-direct hot stamping was not performed since the solid mechanics portion was not within the scope of this thesis. It should be

noted that findings discussed in this chapter are based previous works of two published conference papers [73, 72].

## **4.1 Welding Scheme Optimization**

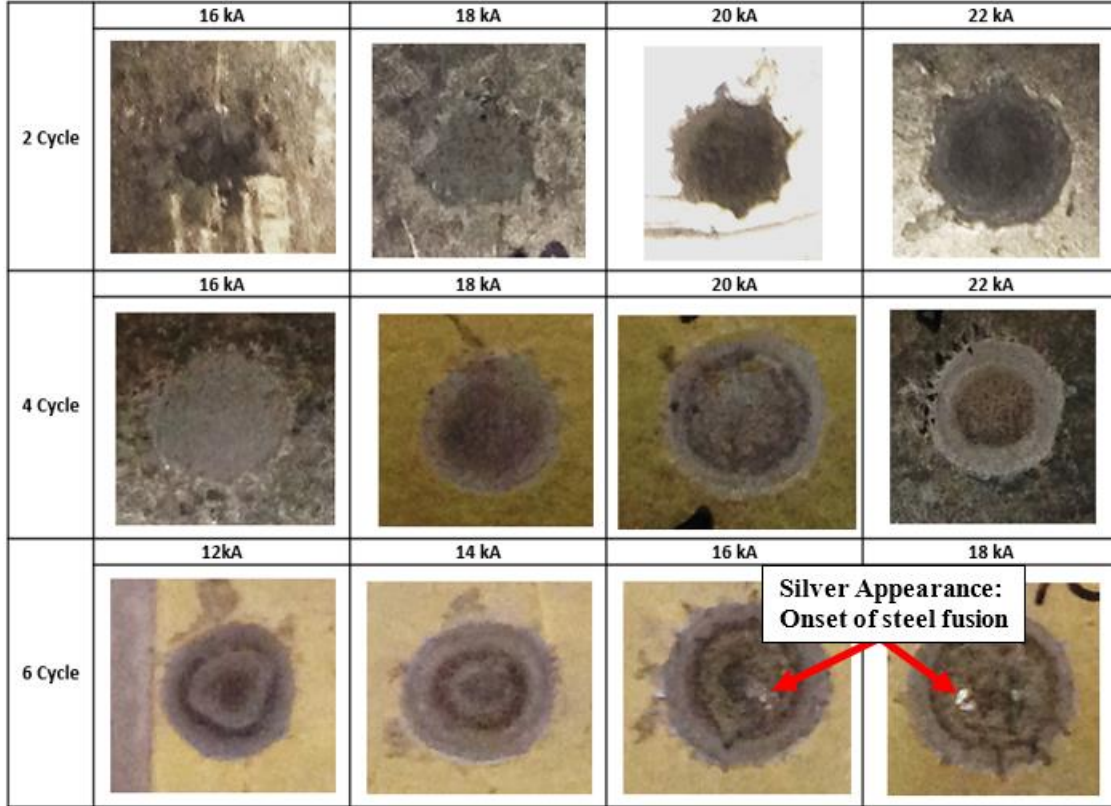
### **4.1.1 Application of pre-pulse current for coating removal**

The preliminary welds performed with single pulsed welding scheme failed due to lack of fusion. An example of a weld cross-section of an unfused joint is shown in Figure 4-4, where only a single main weld current was applied. It can be noted that the sheet interface has not been disrupted in (Figure 4-4A), showing a dark separation line in the weld interface and the absence a weld pool formation. The detail of the nugget center in Figure 4-4B confirms that the Al-Si is intact and continuous at the sheet interface; however, the coating is compressed towards the outer periphery of the weld. The application of only a main welding pulse has only achieved a brazing joint between the sheets through the Al-Si coating, with partial welding of the steel at the outer boundary of the weld. Under normal circumstances of hot-stamped USIBOR sheets, the Fe-Al reaction occurs within the coating layer, causing the coating to be enriched with iron through diffusion from hot stamping, thus increasing electrical resistivity of the coating. In the case of as-delivered USIBOR sheets, the Al-Si coating has not yet been enriched with iron, additionally, the rapid thermal history of RSW does not allow enough time for iron diffusion to form the proper intermetallic phases within the coating. As such, it is suggested that the low interfacial resistance of as-delivered Al-Si coating significantly limits heat generation and inhibits weld pool formation for proper fusion joint. Initial solution to this welding challenge was the removal of Al-Si coating; however, it was not a viable solution for manufacturing considerations since removal of the coating will no longer protect the steels from oxidation during the final phase of the indirect hot stamping process. This emphasizes the need for alternate welding parameters for as-delivered USIBOR steel that has not undergone the hot-stamping heat treatment.



**Figure 4-4: A) Optical macrograph of cross-section when no pre-pulse is applied, B) detail of interface at nugget center, showing the Al-Si coating remaining at the interface.**

In order to displace the Al-Si coating from the interface, an initial high-current pre-pulse was required before the main welding pulse current. In order to assess the role of the cycle time and current on the coating and interface structure, the pre-pulse parameters in Figure 4-5 were applied, followed by peel testing and visual observation of the superficially welded coupon. The interface surfaces with bright silver regions (indicated with arrows) represent the onset phenomenon of bonded steel when either 16 or 18 kA was applied for 6 cycles. Further observations to the weld surfaces indicated that 18kA current pulses was too aggressive at the electrode/sheet interfaces, as such a pre-pulse of increased time of 7.2 cycles and 16 kA was applied for all subsequent testing in order to ensure the coating has been sufficiently disrupted by the pre-pulse for consistent weld pool formation.



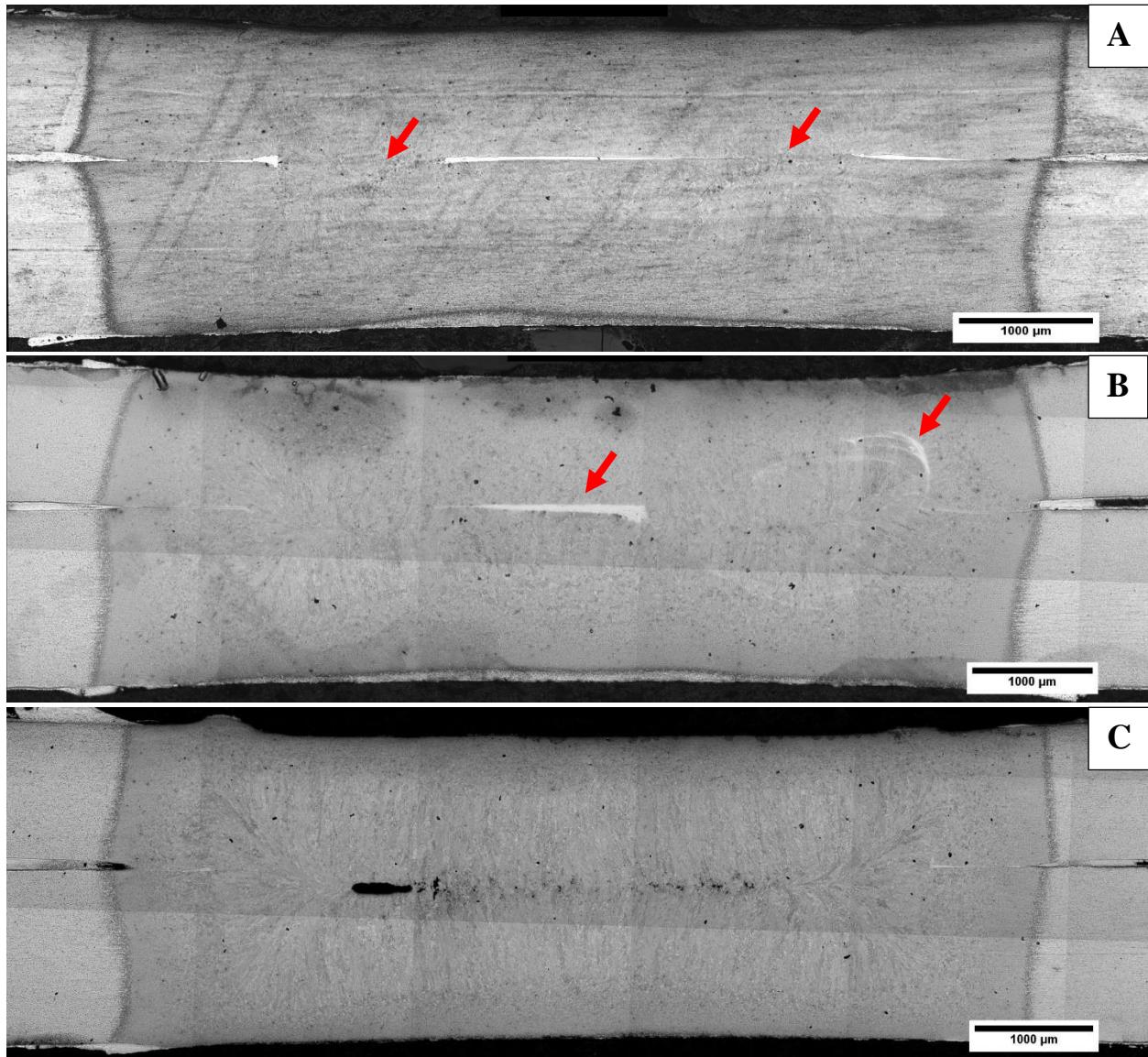
**Figure 4-5: Appearance of interface following the application of pre-pulse parameter cycle times and currents**

#### 4.1.2 Weld growth progression

In order to verify the effectiveness of pre-pulse current for coating dispersion, a series of interrupted weldments were made (at 7.2 cycles, 13.2, and weld completion). The interrupted nuggets were cross-sectioned for metallographic observation of weld growth progression. Figure 4-6 illustrates the weld growth progression of as-delivered USIBOR weldment using the welding scheme documented in Table 3-3. Shortly after the pre-pulse current, two weld pools can be observed to initiate at the interface periphery (arrows in Figure 4-6A), successfully penetrating through the coating for better heat generation. The formation of the two weld pools suggests formation of an annular nugget with coating material trapped in the center. After 13.2 cycles, weld pool growth can be observed, gradually stirring the coating into the molten zone and expelling it to the weld notches (arrow in Figure 4-6B). Additionally, the thickening of the coating layer at



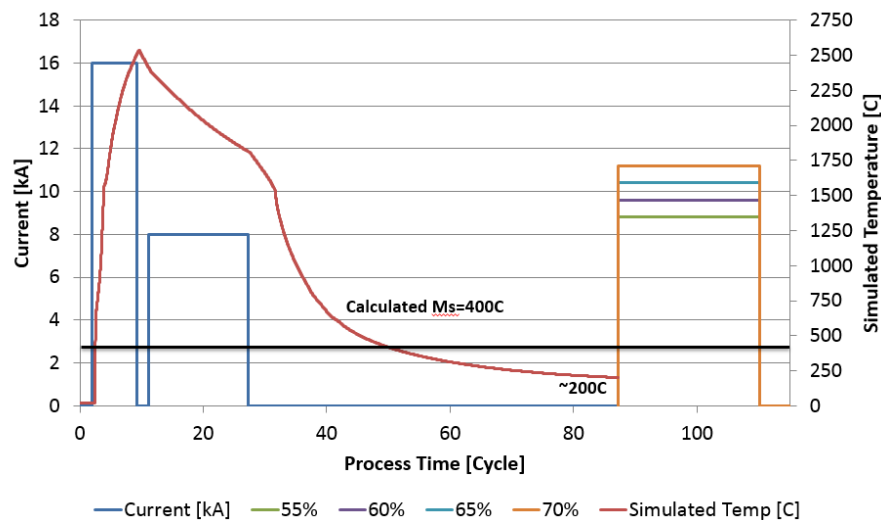
the right side of the weld nugget suggests pressure imbalance due to either misalignment or insufficient force. At weld completion (Figure 4-6C), a dog-bone weld nugget can be observed with all coating material squeezed out into the corona bonds. The irregular nugget shape is caused by a combination of heat imbalance from the different sheet thicknesses and weld pool initiation sites.



**Figure 4-6: As-delivered USIBOR nugget growth progression: A) growth progression after pre-pulse current (7.2 cycles) B) growth progression after 13.2 cycles welding time C) final nugget growth progression**

### 4.1.3 Tempering pulse selection

The nugget thermal profile was simulated with SORPAS to verify sufficient weld pool solidification for meaningful tempering of the weld structure. Figure 4-7 illustrates main welding current vs process time parameters (blue) with overlapping thermal history (red), followed by tempering pulse currents (various colours). The quench period was simulated for one second for weld pool solidification, bringing the weld pool temperature down to around 200°C. This temperature is sufficiently below the martensite start temperature (approx. 400°C), thus ensuring that the weld microstructure will be fully martensitic before tempering.



**Figure 4-7: Welding current pulses and SORPAS simulated thermal history for weld quench prior to in-process tempering pulses**

As mentioned in previous chapters, temper pulse currents are kept at constant 30 cycles of cycle times, while the current levels were selected as percentages of the maximum applied current from the main nugget growth pulses, in this case 16kA instead of 8kA to counteract current density loss caused by surrounding conductive aluminized coating. Temper currents were evaluated based on percentages of this peak current, ranging from 55 to 70% at 5 increments (8.8 to 11.2kA at 0.8kA increments).

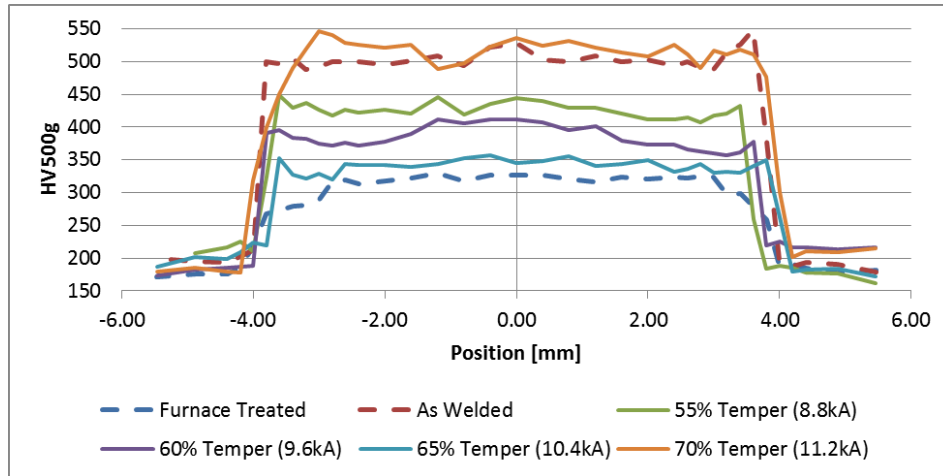
## **4.2 Mechanical Testing Results**

In order to evaluate the effectiveness of tempering pulses, micro-hardness and tensile tests were performed on the welds. Vickers micro-hardness testing indicates the extent of microstructural softening of the weld nugget and instrumented tensile shear and cross tensile tests evaluate the tensile resistance of the welds. The main points of analysis for the mechanical tests are: extent and locations of softening (micro-hardness profiles) and joint performance (peak fracture loads).

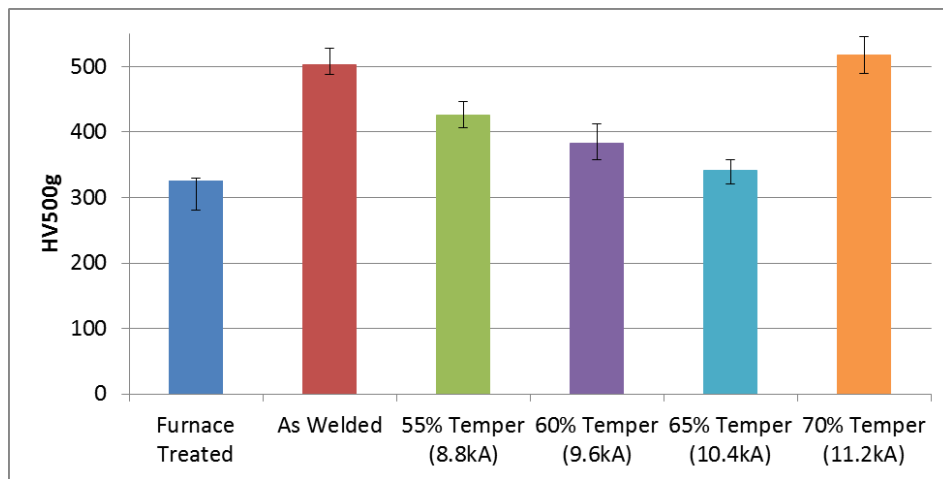
### **4.2.1 Nugget Hardness Profile**

The hardness of tempered welds were compared to an upper and lower limit baseline, where the upper limit is an as-welded (non-tempered) nugget and the lower limit is a fully tempered sample which corresponded to an as-welded spot weld that was furnace heat treated at 600°C for 1 hour. The average hardness for furnace treated and as-welded nuggets were 502 and 326 Hv respectively. Hardness measurements were taken along the diagonal of the weld as specified in AWS D8.9M. Figure 4-8 illustrates the overall hardness profiles and Figure 4-9 illustrates the difference in average hardness of the nugget center.

Initial observations of the micro-hardness results indicated that the tempering heat concentrated at the weld nugget, decreasing hardness by varying levels at corresponding current inputs. With increasing tempering current from 8.8kA, 9.6kA, to 10.4kA, the average hardness decreases linearly from 425, 383, to 342 Hv respectively. The average hardness, however, increased to 518Hv when a 11.2kA temper pulse was applied, suggesting that the nugget has been overheated and formation of austenite occurred followed by the martensite transformation.



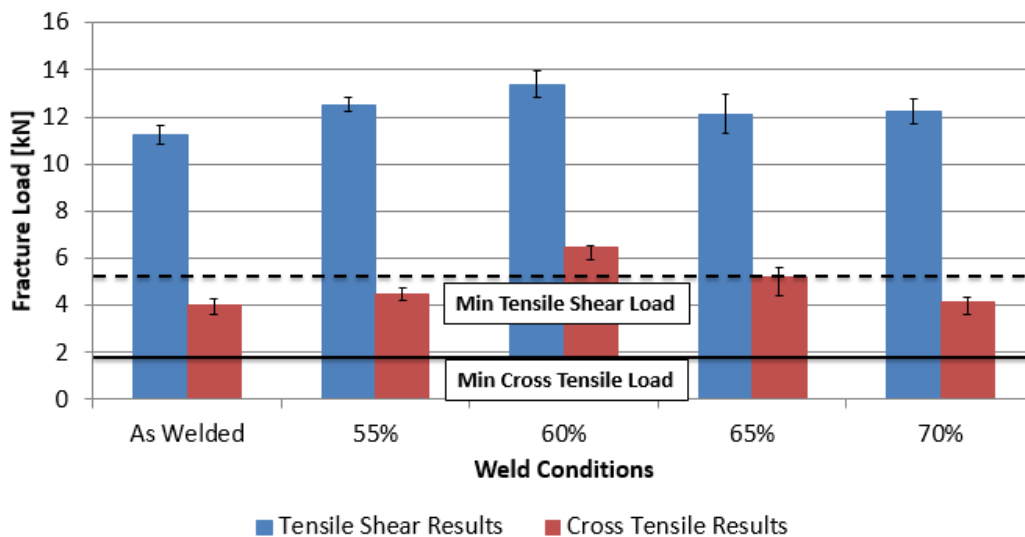
**Figure 4-8: Hardness map profile of as-welded and tempered weldments on as-delivered USIBOR sheets**



**Figure 4-9: Average hardness of nugget centers**

## 4.2.2 Tensile Shear and Cross Tension Results

TST and CTT were performed for joint performance evaluation for as-welded and tempered joints from 55% to 70% max tempering current. Figure 4-10 illustrates TSS and CTS comparison between as-welded and tempered weldments.



**Figure 4-10: Tensile shear and cross tensile joint performance comparison between as-welded (non-tempered) and tempered welds**

The force values for TSS tests (blue bars) averaged at 11.2kN in the as-welded condition, which is considerably higher than the 5.3kN (black dash line) requirement set by AWS standards. When tempering pulses were introduced, the tensile shear loads increased linearly, maximizing at 13.4kN when the 9.6kA (60%) temper pulse was applied. Commonly, softening of the nugget would result in diminishing TSS as the overall nugget integrity (hardness) is decreased from tempering. However, increased toughness of the nugget is believed to have contributed to increased TSS as the nugget is allowed to deform under tensile shear loading, ultimately followed by fracture initiation at the softer base material surrounding the nugget. When tempering currents of 10.4kA (65%) are applied, on the other hand, the TSS values exhibited a slight

decrease from 13.4 to 12.1kN, and held constant when the tempering current was increased to 70% max current.

The overall CTS results (red bars) also exceeded minimal AWS CTS requirement and exhibited near identical trend in cross tensile performance with the application of tempering currents. The CTS increased from 4.0kN to 6.5kN when comparing the as-welded condition to a 60% tempering current magnitude. Again, the increase in CTS is a result in increased toughness of the nugget, allowing better weld opening resistance associated with CTT. The tensile performance began to diminish at 65% max current temper, averaging at 5.2kN and dropping further at 4.2kN when 70% max current temper pulse was applied. These results can be explained by the principle that the local over-heated region from the tempering currents leads to stress concentration zones for easy crack propagation which promotes failure.

### **4.3 Tempered Microstructural Evolution**

Microstructural evolution of each of the temper pulse welds were examined. The cross-sections for the welds produced using 9.6kA, 10.4 and 11.2 kA respectively are shown in Figure 4-11. There was no distinguishable in changes of microstructure for the 9.6kA tempered cross sectioned in Figure 4-11A. A striking feature is the formation of dark-etching regions near the periphery of the nugget in Figure 4-11B. With increasing temper current, these dark regions increased in size, and eventually propagate throughout the weld nugget, as shown in Figure 4-11C. These regions were later confirmed to correspond to the locations of recrystallization of the martensite. The increasing size of the recrystallized zones is consistent with increasing peak temperatures as the tempering current was increased. The formation of recrystallized zones, forming non-uniform tempered microstructure, confirming the hypothesis of diminishing joint performance for temper currents beyond 60% max current.



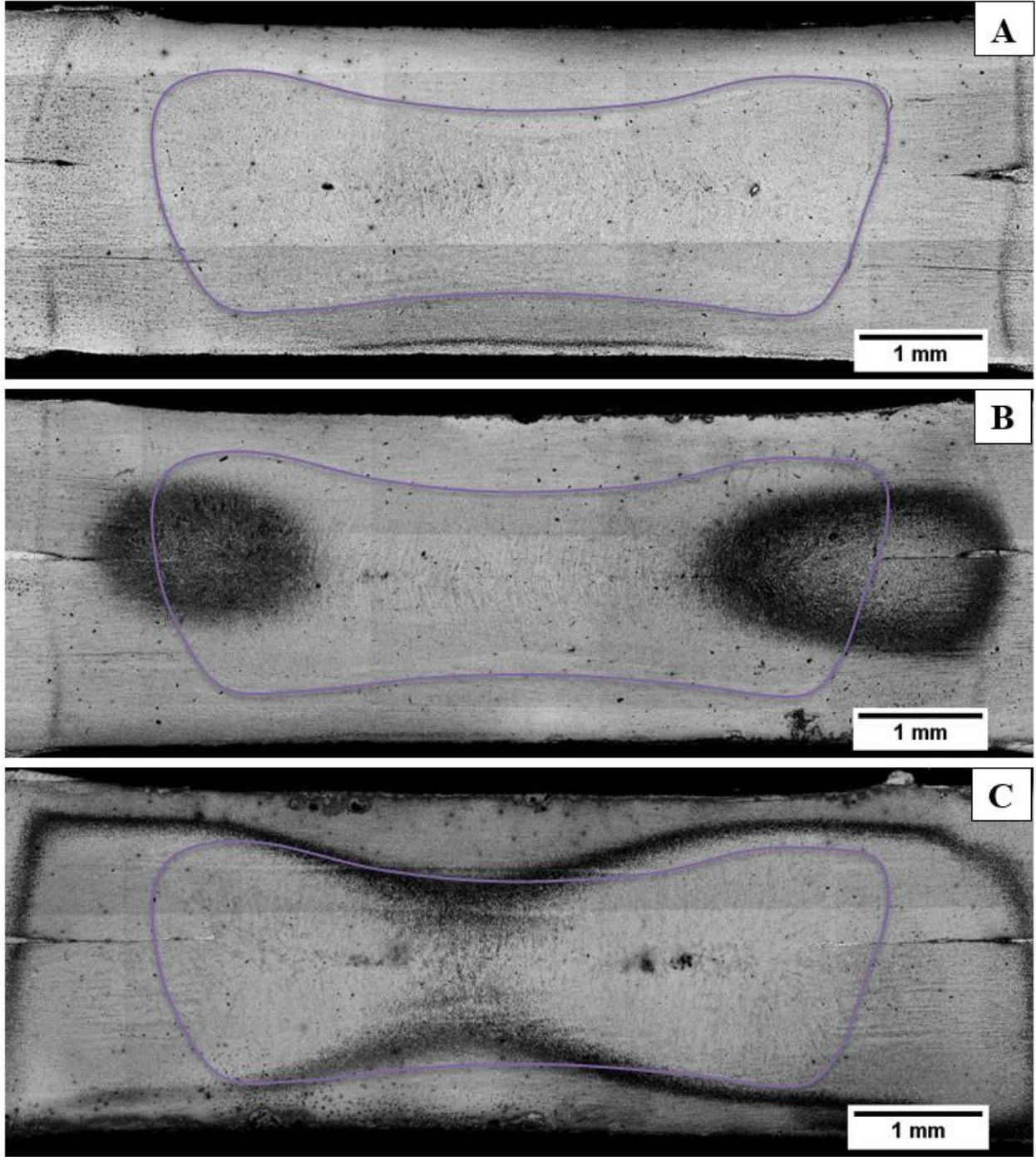


Figure 4-11: Microstructural evolution of different tempering levels: A) 60% max current temper (9.6kA), B) 65% max current temper (10.4kA), C) 70% max current temper (11.2kA)

## 4.4 Summary

Preliminary weldments made on as-delivered USIBOR sheets proved challenging due to the highly conductive aluminized coating inhibiting heat generation for proper fusion. Metallurgical observations confirmed that Al-Si coating was retained within the joint interface, forming brazed rather than full fusion joints, as such disruptions/removal of the aluminized coating was required for sufficient heat generation for proper weldments.

A parameter matrix of instantaneous spike current pulses and cycle times was tested and verified superficially by joint interface evaluation through peel tests. The parameter combination that exhibited onset of steel fusion from the joint interface was selected for pre-pulse current parameter. The effectiveness of this pre-pulse in disrupting the coating and promoting nugget growth was verified by a series of weld progression cross-section microstructures.

A series of in-situ tempering currents held at 0.5 seconds of constant welding time was applied to the as-delivered USIBOR welds after 1.0 second of quench period. 65% peak current (10.4kA) tempering parameter yielded the highest softening of the martensitic nugget structure, averaging Vickers hardness at 340Hv. Weld tempering at 70% peak current (11.2kA) resulted in a recrystallization of the weld nugget due to microstructure overheat, increasing the average weld hardness back to 518Hv.

Joint performance comparison between non-tempered and tempered welds, indicated tensile strength improvements between 55 to 60% peak current tempers (8.8 to 9.6kA) for both CTT and TST evaluations. Peak current temper schemes exceeding 60% resulted in diminishing joint performance. This was later analyzed by metallographic observations and concluded that non-uniform tempered structures with localized recrystallized zones, creating stress concentrations, leading to a performance decrease when more than a 60% peak current is applied during tempering.



## Chapter 5

### RSW and In-Process Tempering of Hot-Stamped USIBOR Sheets

In this chapter, weldment and in-process tempering behavior on hot-stamped USIBOR sheets is investigated and correlated with joint performance, hardness, fracture mode, and microstructures. The extent of weld tempering was evaluated by a comparison between as-welded and tempered weldments, with tempering pulse current ranges from 50% to 70% of the maximum current during the temper pulses at increasing increments of 5%. Three representative weldments are selected for detailed discussion: as-welded (not tempered), optimally tempered, and over-heated tempered weldments.

Initial weld nugget optimization was conducted to ensure consistent base-nugget prior to application of tempering pulses. In addition, weld quench period was simulated with SORPAS 2D to ensure fully solidification of weld pool for meaningful tempering of the microstructure.

Prior to successful nugget tempering, weld challenges of secondary weld pool formation was present. The phenomenon were caused by of low machine stiffness and “less than perfect” electrode alignment when utilizing tempering current pulses for hot-stamped USIBOR RSW. The issue was mitigated by careful tuning of electrode alignment.

Joint performance was assessed by employing instrumented cross tensile (CTT) and tensile shear tests (TST) at quasi-static strain rates; from which, joint strength, displacement, fracture mode, and weld toughness were examined. The corresponding tensile information was then cross-examined with Vickers micro-hardness maps for both tempered and non-tempered welds. In addition, cross-sections of fractured representative welds were also examined for crack initiation and propagation to assess corresponding joint performance data.

Weld microstructural evolution between as-welded and optimally tempered microstructures were compared with both optical and scanning electron microscopy. Optical microscopy is used to characterize

the metallurgical changes across the weld structure from the FZ to BM. Scanning electron micrographs illustrate these changes in detail within the martensitic lath structure as well as carbide precipitations at different heat affected regions.

### 5.1 Welding scheme optimization

Optimization of initial weld nugget was performed with the application of a two pulse welding scheme was a modified version of the AWS two pulse welding scheme [74]. The initial current pulse of 6.5kA for 12cycles (200ms) was selected and verified experimentally after yielding nugget diameter 5.07mm, just above the minimum nugget size, 4.90mm. The second pulse followed after a 4 cycle (67ms) cooling period to control nugget overheat was tested between 6-9kA at 1kA increments with a duration of 16 cycles (267ms). At 6kA to 7kA current increments, the weld nugget remained constant, averaging 5.4mm in diameter. When weld currents beyond 7kA were applied, the weld diameter increased in a linear fashion, maximizing at 6.9mm prior to expulsion at 8.5kA and beyond. The selected weld parameter for the in-process heat treatment current pulses is the 6.5-8kA scheme, yielding maximum nugget at 6.9mm. Figure 5-1 illustrates weld growth based on increasing applied currents.

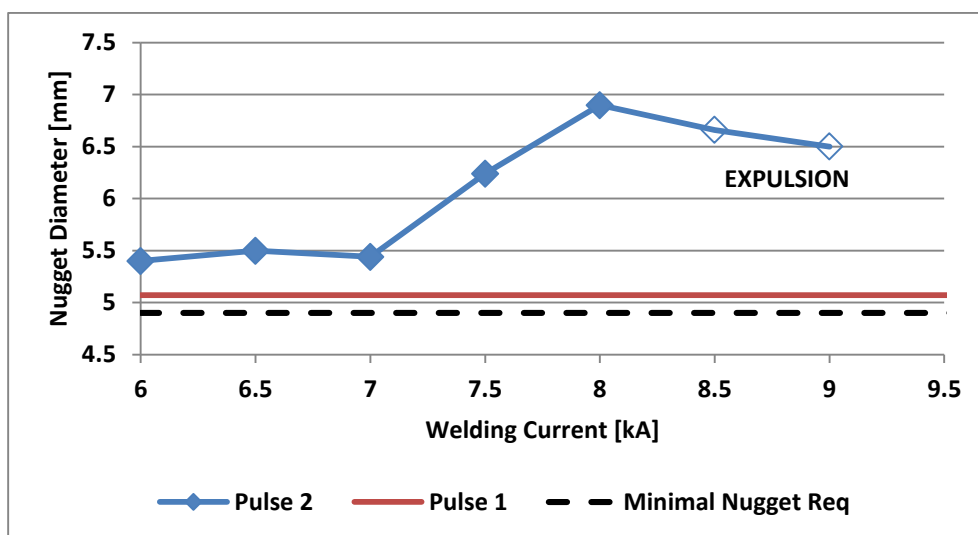
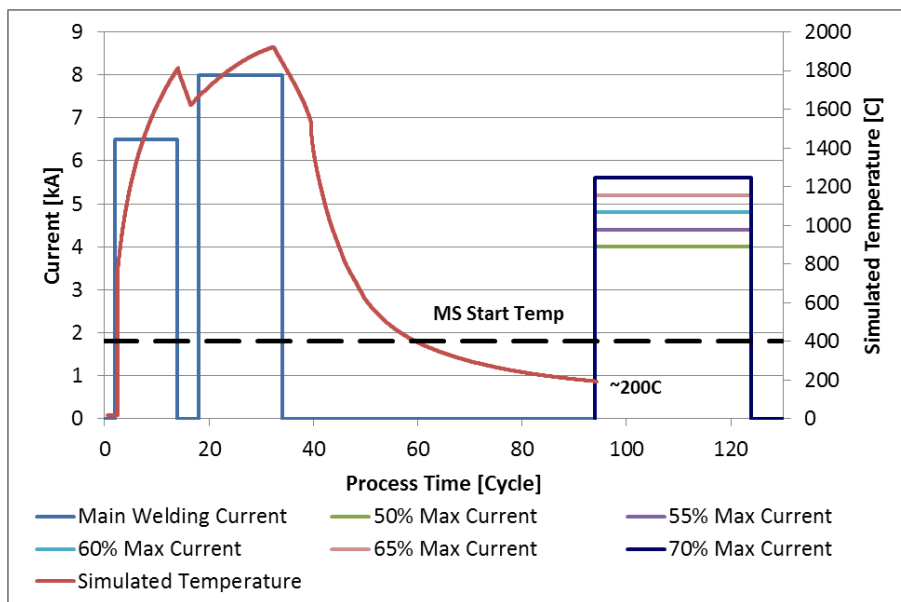


Figure 5-1: Hot-stamped USIBOR weld: initial nugget optimization

### 5.1.1 Quench period determination and Temper pulse application

Sufficient solidification of the weld pool was required in order to have meaningful tempering of the weld microstructure. Simulated thermal profile of the weld pool indicated after one second of cooling time brings the weld pool temperature down to around 200°C, far below martensitic start temperature ( $M_s$ )



**Figure 5-2: Weld Nugget Thermal Profile & Welding Scheme Pulses**

As previously mentioned, cycle times for temper pulses were kept constant at 30 cycles (0.5 seconds) and the currents selected were of percentages of the maximum applied current from the main nugget development pulses (in this case 8kA). Temper current percentages from 50 to 70% at 5% increments were tested. For simplicity, only 55% and 70% max current temper pulses were selected for detailed discussions, as these two temper profiles provided the most significant changes in the microstructure and weld performance behavior. The selection criteria for these two weldments will be covered in the following joint performance analysis.

### 5.1.2 Tempering Challenges

Prior to attaining successful tempered weld structures, challenges of secondary weld pool formation created by the tempering pulses was a major concern. The formation of a secondary weld pool prohibits the original weld structured to be successfully tempered, as a fraction of the weld nugget can be re-melted, while the remaining fraction becomes part of the heat affected region. The appearance of secondary weld pool is an indication of heat imbalance caused by electrode misalignment. Figure 5-3 illustrates the weld cross-section comparison between a nugget created by severely misaligned electrodes to a weld nugget with ideal electrode alignment.

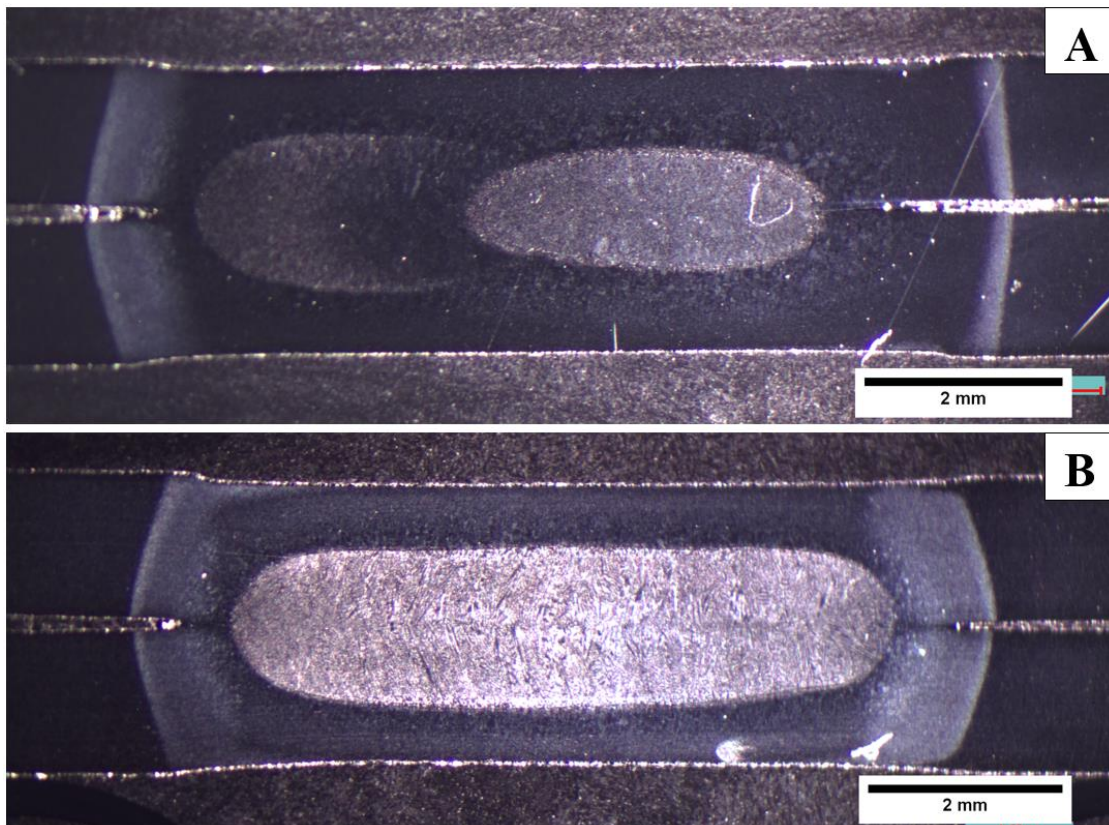
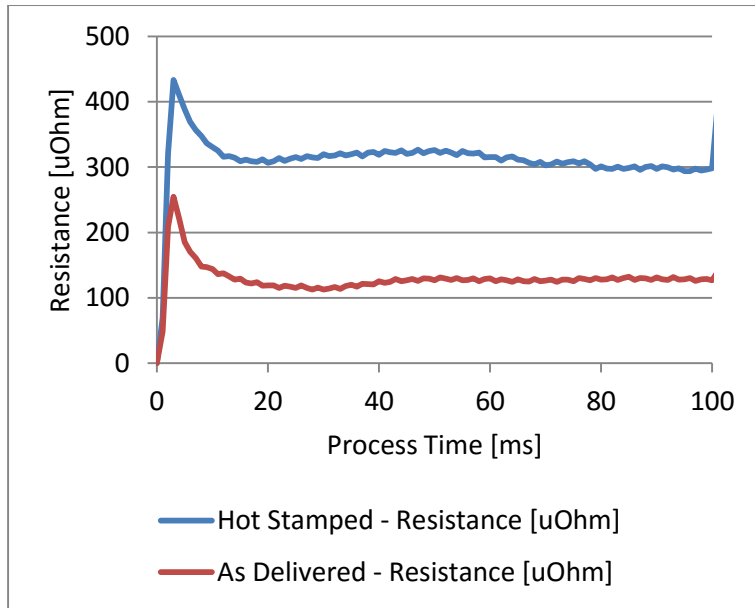


Figure 5-3: Secondary weld pool formation from tempering pulse current due to electrode misalignment: A) severely misaligned, B) ideal alignment

The main cause for secondary weld pool formation is due to deviation of current density caused by electrode misalignment that can be a direct result to poor setup or low machine stiffness when welding high strength materials such as USIBOR. Any component deflection due to low machine stiffness can easily lead to electrode angular misalignment and current density lost at desired weld locations, ultimately creating heat imbalance. In addition, increased resistivity associated with hot-stamped USIBOR in comparison with as-delivered version has high influences towards secondary weld pool formation when current path deviates from electrode misalignment. An iron-rich coating increases the resistivity by more than two times in comparison with as-delivered USIBOR (Figure 5-4). As a result, it is much easier to create a second weld pool with tempering pulse with hot-stamped USIBOR than with as-delivered USIBOR studied in Chapter 4.



**Figure 5-4: Example hot-stamped VS as-delivered USIBOR dynamic resistance**

The formation of secondary weld pool was mitigated by fine tuning electrode concentricity alignment. The end result weld nugget was similar to the corrected alignment weld as illustrated in Figure 5-3B.

## 5.2 Mechanical Testing

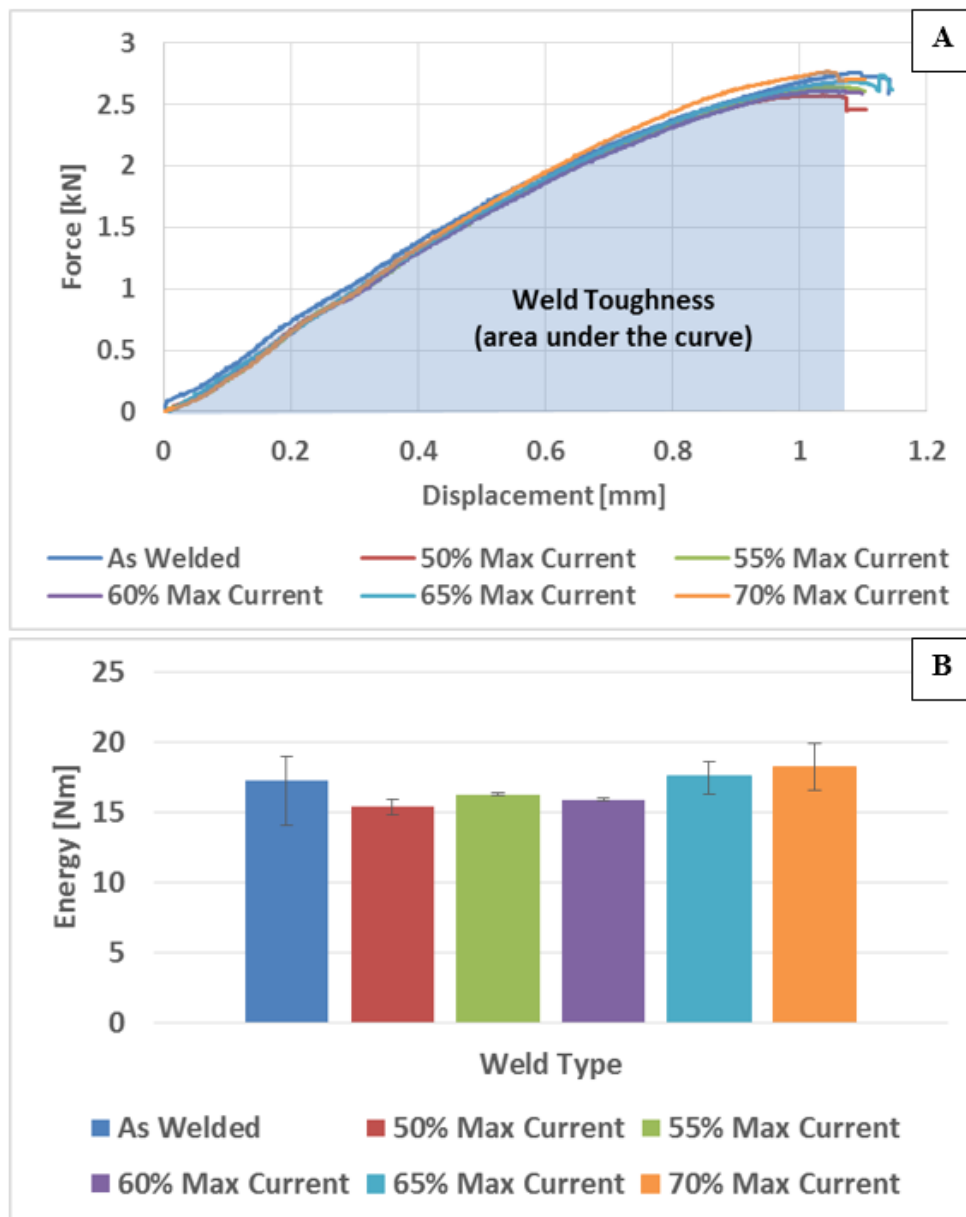
### 5.2.1 Lap Shear and Cross Tensile Performance

Instrumented lap-shear and cross tensile tests of the full spectrum of tempering currents from 50 to 70% max currents were laid out in order to discern any trends in joint mechanical performance. The issues considered for analysis were joint toughness (area under load-displacement curves) and failure mode.

#### 5.2.1.1 Tensile Shear Performance

Figure 5-5 illustrates the lap shear tensile force displacement curves and calculated weld toughness of each welds. The general trend of TSS in tempered and as-welded weldments was that weld strength and toughness decrease for the tempering power at 50 to 60% max currents, and weld strength/toughness recover the as-welded performance range with increased scatter when 65 to 70% maximum temper currents are applied. The highest peak load was attained by the as-welded joint averaging at 27.4kN, at an average fracture displacement of 1.06mm, and weld toughness (energy absorption) of 17.3J. On the other hand, the lowest joint performance was achieved with the 50% max current temper weldment, with a peak load of 25.8J, average fracture displacement of 1.02mm, and calculated weld toughness at 15.5J, resulting in a 10% performance decrease compared to as-welded nugget. TST results of the rest of the welds can be found in Appendix B.

Unlike the behavior observed with welds in Chapter 4, there was no joint performance improvement with the addition of weld tempering for lap shear testing mode; however, there is no significant performance decrease with the addition of tempering, suggesting that tempering for hot-stamped USIBOR weldments does not affect lap-shear joint performance.



**Figure 5-5: Hot-stamped USIBOR tensile shear joint performance comparison between tempered and non-tempered welds: A) load-displacement curves, B) calculated weld toughness**

### 5.2.1.2 Cross Tensile Performance

Tensile results differ significantly between as-welded and tempered nugget strength and toughness in the cross tensile loading mode. In Figure 5-6, the as-welded and tempered welds force displacement

curve and calculated energy absorption are illustrated. The as-welded nugget provides an average fracture force of 7.82kN and fractures at 10.24mm displacement, providing a fracture energy of 43.69J. In comparison to TST results, the failure displacement values are significantly greater than TST displacements (by nearly tenfold) regardless of the lower fracture loads achieved from CTT.

All of the tempered welds exhibited higher joint performance in comparison with the as-welded baseline, with a maximum energy absorption increase of 51.4% achieved by the 55% max current tempered nugget. The 55% max current tempered nugget achieved an increased fracture load at 10.0kN and displacement at 13.63mm; with a fracture energy absorbed of 66.2J. Improvement in performance did not continue to increase when currents increased from the 60% to 70% max current tempered values. At 60% max current temper, a decrease of fracture force and displacement was observed in comparison with the 55% max current tempered weld. The joint performance achieved with further increasing tempering current remain consistent up to 70% max current. The specific cross tensile performance data can be found in Appendix B.

With careful comparison of load-displacement curves between as-welded and tempered welds, it can be observed that the 70% max current tempered weldments shares very similar fracture displacement compared to the as-welded nugget, fracturing at 9.98mm. As a result, the energy increase is due to an increase of fracture load up to 9.51kN. This phenomenon can be explained by the re-austenization of weld nugget caused by severe overheating from the tempering pulse.

In order to further understand the differences and effects of optimally tempered and overheated tempering, three representative welds (as-welded, 55% max current, and 70% max current) are selected for detailed analysis in the following hardness and microstructural evolution sections.



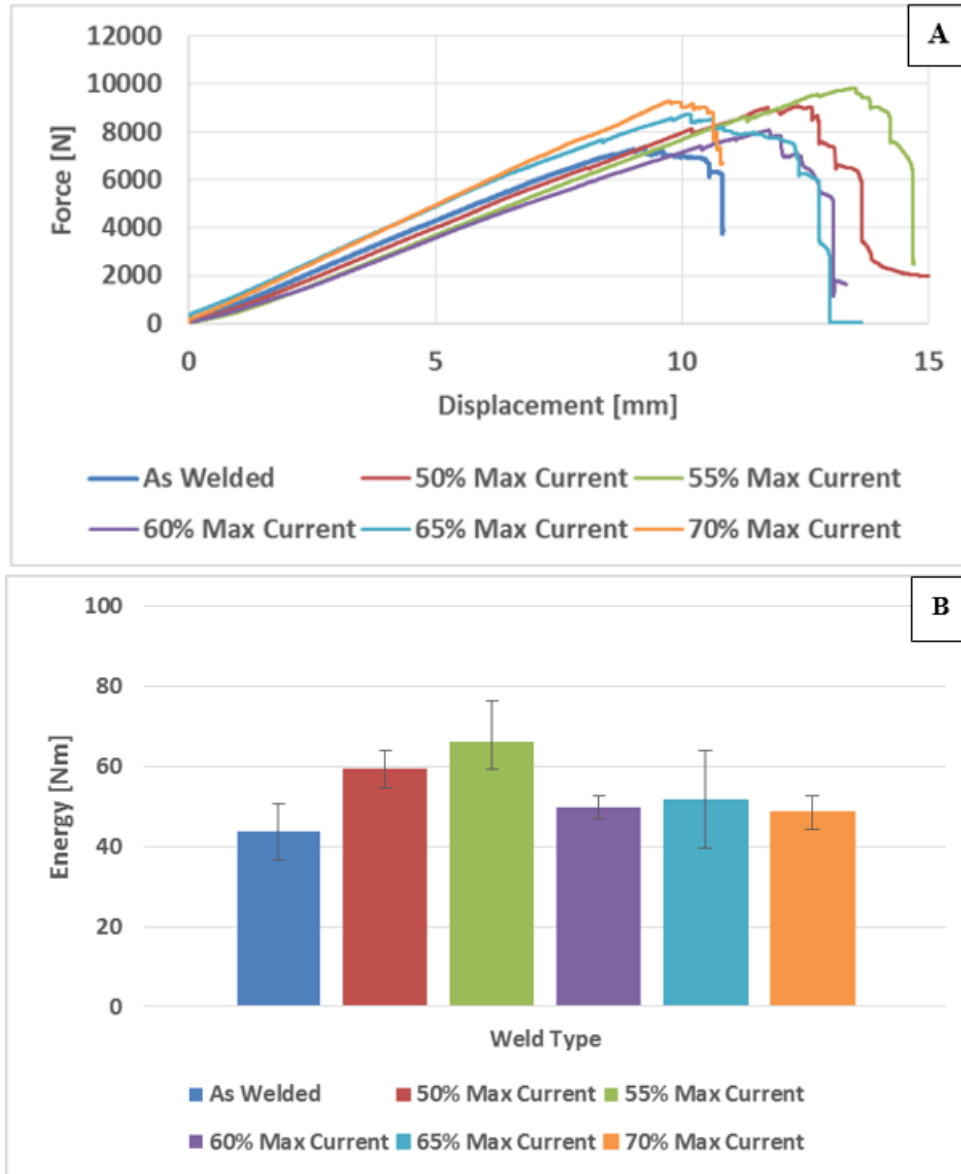


Figure 5-6: Hot-stamped USIBOR cross tensile joint performance comparison between tempered and non-tempered welds: A) load-displacement curves, B) calculated weld toughness

## 5.2.2 Micro-hardness measurements

Vickers micro-hardness indentation profiles were conducted across the three representative welds: as-welded, optimally tempered (55% max current pulse), and overheated tempered (70% max current pulse) (Figure 5-7). The average fusion boundary location (3.5mm from nugget center) of all three welds and the most softened point of the as-welded nugget SCHAZ (4.5mm from nugget center) are labelled for reference. For data consistency, the micro-hardness profiles coincide with the location of metallurgical characterization that will be discussed in the next section.

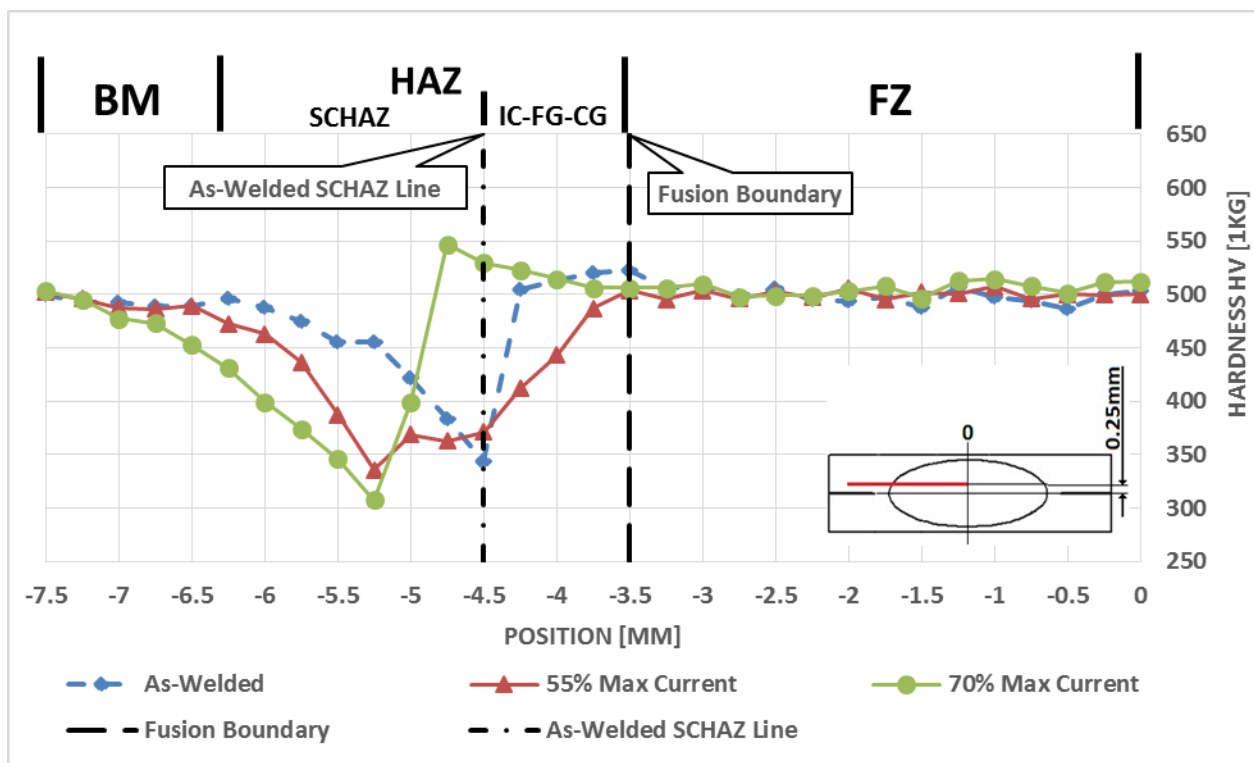


Figure 5-7: Weld Nugget Hardness Profile: a) As-Welded, b) Optimal Tempered, c) Overheated Tempered

All three weldments exhibited consistent hardness averaging 500Hv within the fusion zone. The effect of weld softening of different characteristics are all situated in the HAZ. Average hardness within the CGHAZ, FGHAZ, and ICHAZ remain high at 521, 517, 509Hv respectively for the as-welded profile.

This is due to the high hardenability characteristics of USIBOR allowing most of the HAZ to remain fully martensitic after weld quench. The hardness transition occurs between 4.25 to 4.5mm away from the weld center, with a sharp drop in hardness from 505Hv down to 344Hv. The SCHAZ spans from the 4.5mm to the 6.25mm mark, with minimal hardness at 344Hv gradually returning to the 500Hv ranges.

At an optimal tempering of power (55% max current), significant softening within the upper-critical HAZ can be observed, effectively softening all three CGHAZ, FGHAZ and ICHAZ with a gradual downward trend in hardness from >500Hv to 496, 465, and 360Hv respectively. The application of temper pulses also results in a shift of the softest SCHAZ point away from the center of the nugget, with a minimum hardness of 336Hv situating at the 5.25mm mark compared to the 4.5mm mark for the as-welded nugget. This softening characteristics is believed to be beneficial to lowering stress concentrations at the weld periphery, specifically at the corona bonds, effectively nullifying notch sensitivity.

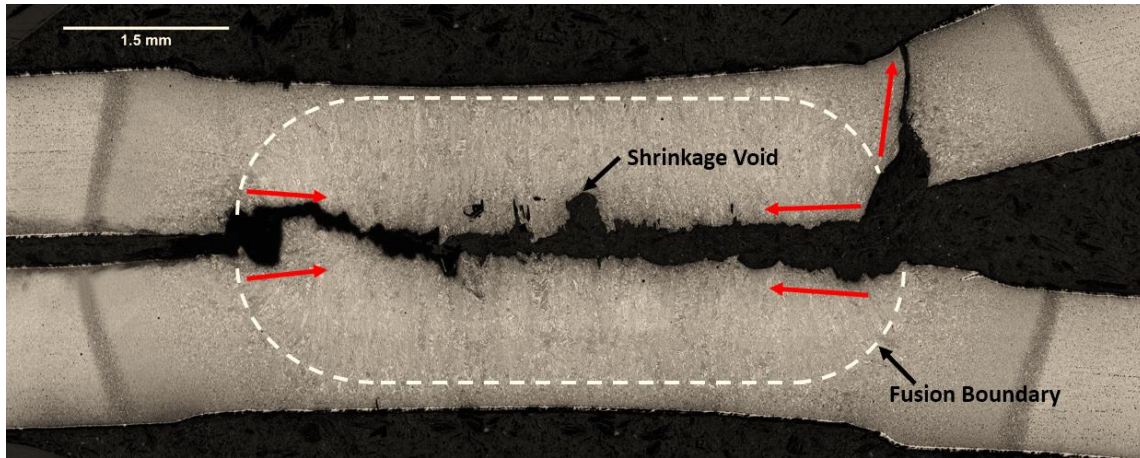
At overheated tempering currents >60%, the HAZ is significantly expanded stretching from the FB to the 4.75mm mark. The entire upper-critical HAZ retained its high hardness due to an overabundance of current input, resulting in a large portion of the HAZ to become transformed into austenite and quenched to martensite. The issue of notch sensitivity is expected to return with this amount of current input.

### **5.3 Failure Analysis**

As previously mentioned, the different types of weld failure relates closely to the nugget's load bearing and energy absorption capacity. The transition between interfacial (IF) to pullout failure (PO) mode generally relates to increasing weld diameter until the fusion zone strength exceeds HAZ local yield strength, resulting in necking and fracture of material surrounding the weld nugget. However, interfacial failure mode remain prominent for USIBOR RSW. Cross sections of the three representative fractured welds (as-welded, optimally tempered, and overheated tempered) in are illustrated from Figure 5-8 to Figure 5-10. The comparison between the three cross sections correlates with tensile and hardness results as observed in

the previous sections. It should be noted that the cross sections are specifically fractured cross tension samples since the most significant changes to joint performance was observed from the CTT experiments.

#### 5.3.1.1.1 As-welded (Non-tempered)

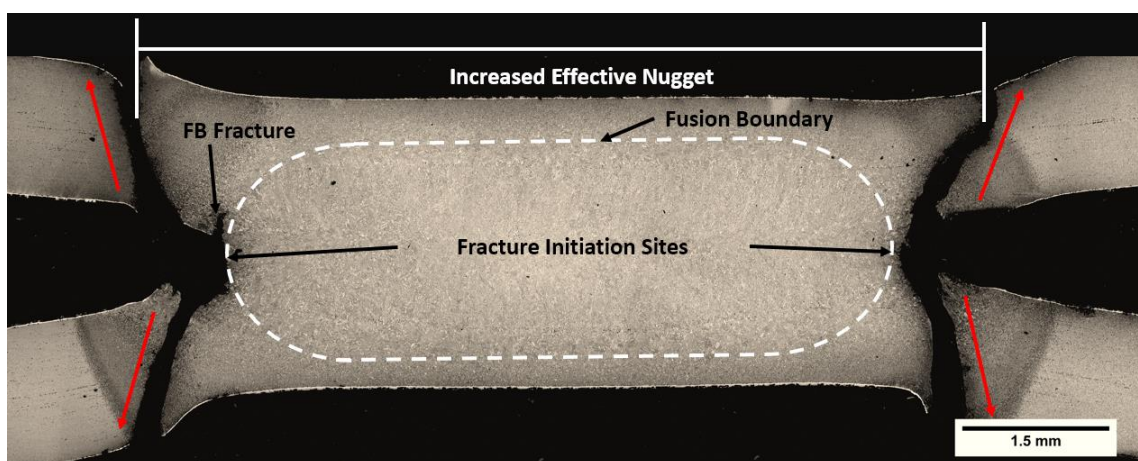


**Figure 5-8: Cross tensile fracture cross-section of as-welded (non-tempered) hot-stamped USIBOR weldment**

Two out of three non-tempered welds failed interfacially with the third failing with partial pullout during CTT. As illustrated in the Figure 5-8, crack initiation occurs at the corona bonds, where brittle coating intermetallic and stress concentration points reside. The crack propagation cuts inwards towards the weld center as the periphery of the weld is pulled open from the cross tensile loading. Interfacial failure is also assisted by the presence of shrinkage voids that are created from rapid cooling of the weld pool during solidification. This resulted a non-continuous structure within the fusion nugget, presenting as weak points during fracture. In the case of partial pullout the right side of the cross-section in Figure 5-8, the crack propagation appeared to have propagated through the UCHAZ, despite the high hardness of the material in the area. This simply explains that that brittle fracture occurs instantaneously through the weld interface instead of prolonged displacement from necking of base material commonly observed in nugget pullout failure mode.

#### 5.3.1.1.2 Optimally tempered welded (55% max current temper)

The fracture cross-section of the optimally tempered weld exhibited pullout failure mode of all three measured welds, with crack initiation occurring at the corona bonds and the crack propagated through UCHAZ. It should be noted that the weld nugget is remain attached with one side of the base material with majority of surrounding base material having fractured, resulting in the double pullout failure appearance illustrated in Figure 5-9.

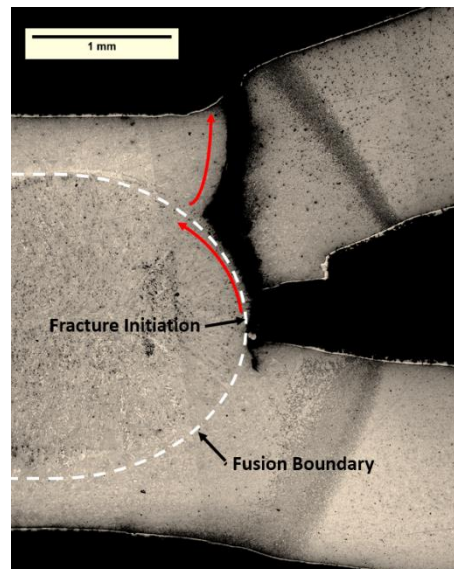


**Figure 5-9: Cross tensile fracture cross-section of optimally tempered hot-stamped USIBOR weldment**

Based on the corresponding hardness decrease of the UCHAZ as well as SCHAZ widening, the crack propagation through the heat affected base material resulted in an outward direction crack path as shown with red arrows in Figure 5-9. The resulting button diameter (also labelled as effective nugget) is much greater than the initial weld pool diameter (as indicated by fusion boundary, dashed white line). *I.e.* a nugget diameter of 6.9mm vs. an effective nugget of 8.6mm. The increased effective nugget diameter requires a much larger force and increased ductility for the weld button to neck and fracture, as such, explaining the increased nugget toughness in the cross tensile mode.

#### 5.3.1.1.3 Overheated tempered weld (70% max current temper)

All of the overheated tempered welds failed with pullout failure mode. This is illustrated with red arrows in Figure 5-10, where the fracture propagation path, initiating from the corona bond point of the weld interface, is followed closely with the fusion boundary until fracturing through the base material. Based on load-displacement curve, the decrease in displacement indicated that the nugget yielded much sooner than that of 55% tempered weld, despite the higher fracture forces attained. The faster yielding of the weld joint was a result of stress concentration points of the corona bond allowing for brittle failure through the HAZ as soon as the fracture load is reached, this was reinforced by the micro-hardness profile discussed in the previous section, ultimately resulting in lower weld toughness.



**Figure 5-10: Cross tensile fracture cross section of overheated tempered hot-stamped USIBOR weldment - fusion boundary fracture path**

## 5.4 Weld Microstructure

Two representative weld cross-sections of as-welded (non-tempered) and tempered nuggets along with microstructural details of specific zones are illustrated in following figures. Microstructural changes between the tempered and non-tempered weld nuggets are investigated and compared with both OM and SEM. For simplicity, only one quarter of the weld nugget of identical orientation was imaged and analyzed.

### 5.4.1 Microstructural Evolution Comparison – Optical Microscopy

The microstructural variation in the as-welded and tempered nuggets can be observed in Figure 5-11 and Figure 5-12. The figures are divided into 5 different regions and indicated with letterings as, “A” FZ, “B” CGHAZ, “C” FGHAZ, “D” ICHAZ, and finally “E” the unaffected BM. It should be noted that SCHAZ structures do not exhibit physical changes in comparison with BM at optical microstructure magnifications. This is due to the absence of phase transformations (thermal histories at sub-critical temperatures), as such, the SCHAZ was not characterized with OM in Figure 5-11 and Figure 5-12.

#### 5.4.1.1 Macrostructure:

As-welded and tempered macrostructure significantly differ from each other, specifically in the HAZ regions labelled from “B” to “D”. HAZ of the tempered weldment presented with darkened microstructure phases, localizing between the fusion boundary and ICHAZ, and the formation of the structure is a result of partial phase transformation due to localized heating in the weld periphery when the temper pulse was applied. Partial phase transformation can commonly be observed in the ICHAZ where the thermal history is between the  $A_{C1}$  and  $A_{C3}$  critical temperatures.

Normally, temper heating should initiate from the weld center due to path of the least resistance through the weld metal and resistively heating is solely based on bulk resistance of the weld nugget. However, the phenomenon of periphery heating (also observed in welds in Chapter 4) for the hot-stamped

state weldments can be explained by the combined effect of electrode misalignment and the presence of coating intermetallic in the corona bond. In the case of slight angular electrode misalignment, weld current can concentrate at one side of the weld, specifically at the weld periphery. In addition, as discussed in Chapter 2, the intermetallic achieved within the corona bond creates highly conductive paths, diminishing current density through the weld center. Consequently, the application of the tempering pulse, current density is localized at the HAZ and heating initiates at the corona bonds.

#### 5.4.1.2 Fusion Zone:

The FZ microstructure between as-welded and tempered weldments do not exhibit significant differences. As illustrated in Figure 5-11A and Figure 5-12B, the FZ microstructure consists needle-like martensitic structure with columnar structure as a result of epitaxial solidification and growth from the FB towards the weld center. Thermal history within the FZ exceeds liquidus temperatures ( $T > 1500^{\circ}\text{C}$ ) and quenched rapidly by the copper electrodes, resulting in a fully martensitic microstructure.

#### 5.4.1.3 Coarse Grain HAZ:

The CGHAZ structures differ between as-welded and tempered welds. Common martensitic grain coarsening can be observed in the as-welded weldment, due to peak temperatures in the CGHAZ are well above  $A_{c3}$  temperature, resulting in 100% austenite transformation. Subsequent rapid cooling resulted with large martensitic packets within large prior austenite grains. Tempered CGHAZ exhibited darker partially transformed phases within martensitic structure, specifically between packets and prior austenite grain boundaries. The overall microstructure remains martensitic.

#### 5.4.1.4 Fine Grain HAZ:

In the FGHAZ, grain refinement of the martensitic structure can be observed as distinct lath structure become hard to distinguish at the observed magnification for the non-tempered weldment. The



peak temperature in this region still exceeded  $A_{c3}$ ; however, not at a level that significant austenite grain growth can be observed. When the microstructure is quenched, finer martensitic structure is transformed. In the case of tempered FG-HAZ, like tempered CGHAZ, partially transformed phases can be observed; however, the overall structure is much finer due to grain refinement.

#### 5.4.1.5 Inter-Critical HAZ:

The microstructure within the ICHAZ consists a mixture of brighter retransformed martensitic phase and remaining darker martensitic phase. Peak temperatures within this region exceed the  $A_{c1}$  temperature but does not exceed  $A_{c3}$ . Consequently, partial dissolution of hot-stamped martensite structure into austenite occurs and subsequently quenched, forming new martensitic phases again. The ICHAZ microstructure between the as-welded and tempered weldments do not differ significantly, since the majority of the tempered nugget HAZ was partially transformed.

#### 5.4.1.6 Base Metal:

Finally, the BM microstructure of the as-welded and tempered weldments share the same martensitic morphology after the alloy has been hot pressed. This region does not exhibit any changes in microstructure since thermal histories were not high enough to undergo any metallurgical transformations.

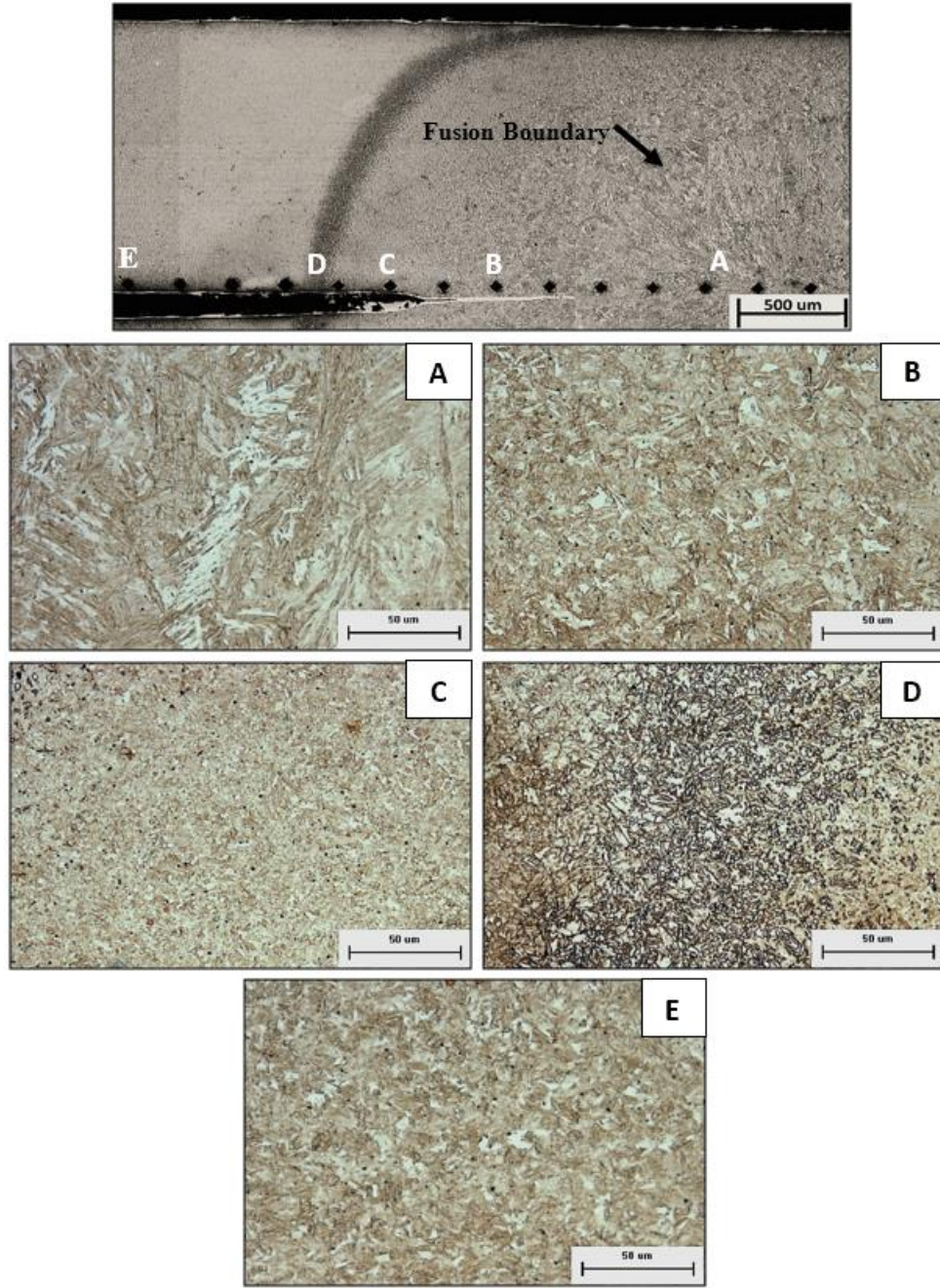
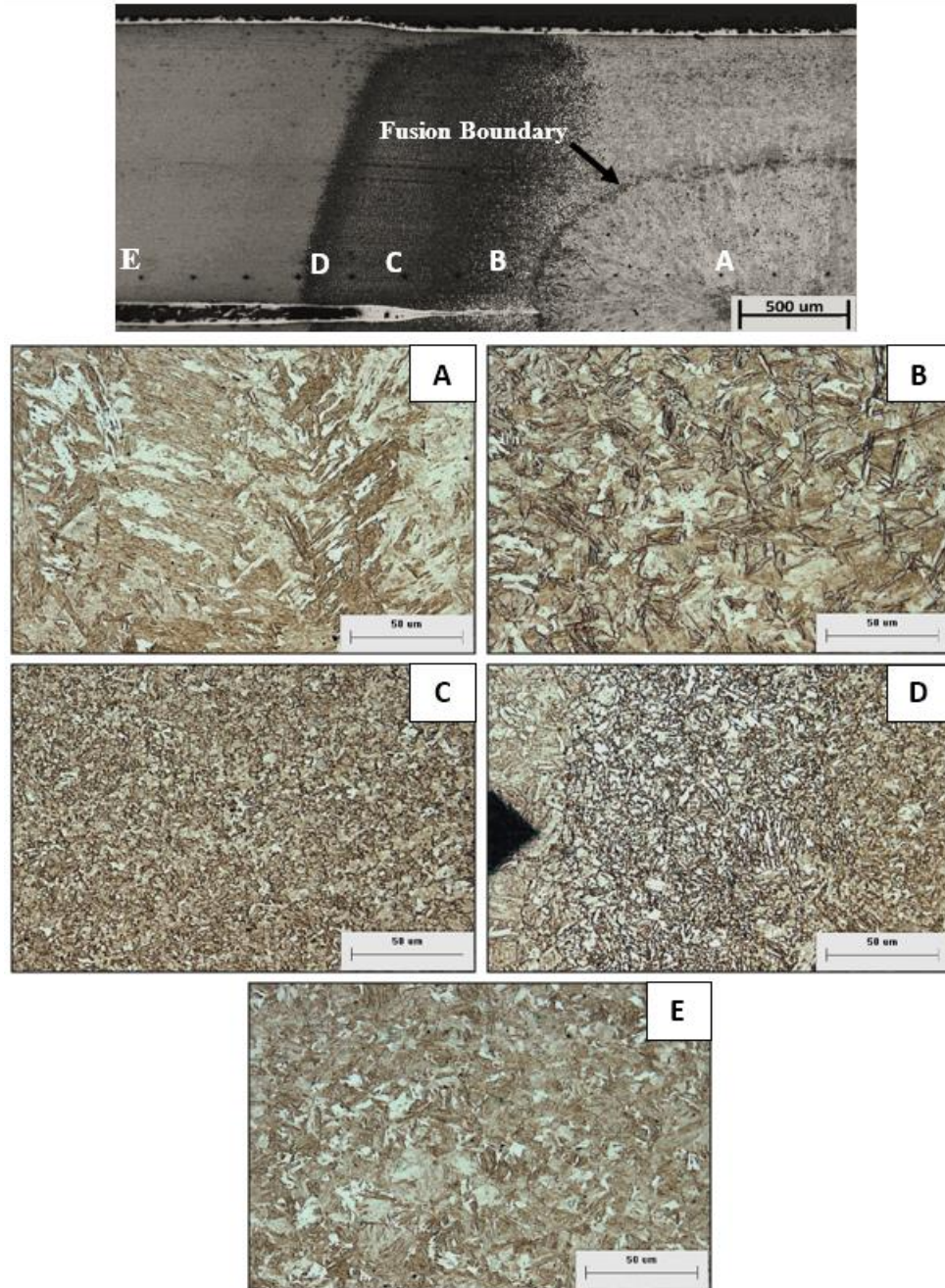


Figure 5-11: As-welded cross-section macrostructure and detailed microstructure of different regions: A) fusion zone (FZ), B) coarse grain region (CGHAZ), C) fine grain region (FGHAZ), D) inter-critical region (ICHAZ), E) base metal (BM)



**Figure 5-12: Tempered cross-section macrostructure and detailed microstructure of different regions: A) fusion zone (FZ), B) coarse grain region (CGHAZ), C) fine grain region (FGHAZ), D) inter-critical region (ICHAZ), E) base metal (BM)**

## 5.4.2 Microstructural Evolution Comparison – Scanning Electron Microscopy

Microstructure characterization by SEM of the HAZ sub-structures of as-welded (labelled A-x) and tempered (labelled T-x) weldments are illustrated in Figure 5-13. Each sub-region is labelled alphabetically as the second letter from B to E: “B” CGHAZ, “C” FGHAZ, “D” ICHAZ, and “E” SCHAZ. The comparisons between as-welded and tempered microstructure benchmarks the degree of tempering.

### 5.4.2.1.1 Coarse Grain HAZ

Two types of martensitic formations can be observed within the as-welded CGHAZ (Figure 5-13A-B): needle like structures with fine carbide precipitation (white specks) are auto-tempered martensite (ATM) and finer and lighter martensite phases (M) situated between packets. Auto-tempering of martensite is caused by non-uniform martensite formation rates as the microstructure is quenched. Martensite that forms faster become slightly tempered before the rest of the structure is transformed to martensite structures. The tempered CGHAZ (Figure 5-13T-B) depicts a much different structure. The major change is the decomposition of lath structures and the formation of severely tempered martensite packets (STM) where large amount carbide precipitation (white speckles) can be observed. It should be noted that the martensite of different contrasts are caused by structures of different orientation. Additionally, bright packets of newly formed martensite (NM) due to partial transformation can be observed. This is consistent with the darker phases within grain boundaries shown in Figure 5-12B. Finally, boundaries are much brighter compared to the non-tempered counterpart. This is believed to be caused by additional carbon diffusion caused by the applied temper pulse.

### 5.4.2.2 Fine Grain HAZ

As-welded FGHAZ (Figure 5-13A-C) exhibits a much finer, but similar, martensitic structure with comparison to its coarse grained counterpart. Evidence of auto-tempered and normal martensite structures



can be observed. Due to the grain refinement, slight evidence of prior austenite grain boundary can be observed at the given magnification (distinguished by dashed line borders). The tempered FGHAZ (Figure 5-13T-C) consists a mixture of severely tempered martensite packets and newly formed martensite from partial transformations. The overall structure is finer due to the initial fine structure at given location from the first weld quench. The same brightly lit boundary structures can also be observed from diffusion.

#### 5.4.2.3 Inter-Critical HAZ

Near identical structures can be observed in both as-welded and tempered ICHAZ illustrated in Figure 5-13A-D and Figure 5-13T-D respectively. Due to the thermal histories of the ICHAZ from the initial weld solidification, the microstructures here are partially transformed, forming two different phases: newly transformed martensite (NM) and ferritic islands (F). The formation of new martensite is caused by decomposition of the original martensite structure into austenite, and again quenched back into martensite. The retained martensite that are not partially transformed undergoes rejection of carbon out of its metastable phase into ferritic islands. It should be noted that the applied temper pulse allowed further carbon diffusion to occur, resulting higher contrast between the phases and bright boundaries.

#### 5.4.2.4 Sub-Critical HAZ

As-welded and tempered SCHAZ share near identical microstructures (Figure 5-13A-E and Figure 5-13T-E). Both micrographs exhibit severely tempered martensite structures throughout as this region experiences subcritical temperatures, resulting in fully tempered martensite. In comparison to the as-welded SCHAZ, larger prior austenite grain boundaries (illustrated by dashed lines) can be observed in the SCHAZ with the addition of temper pulse. This can be expected due to prolonged exposure to tempering temperatures, allowing further decomposition of martensitic lath structures.

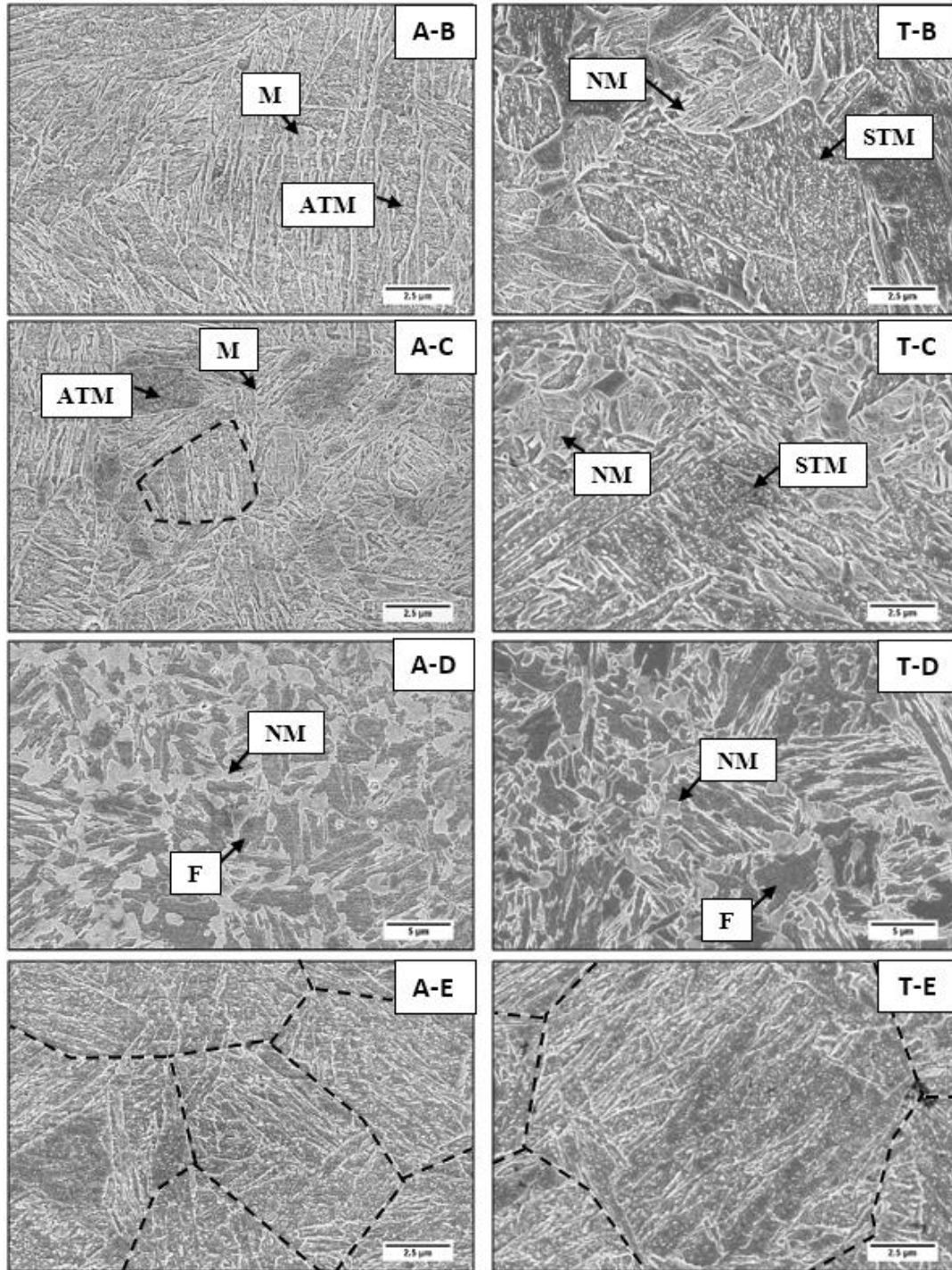


Figure 5-13: SEM micrographs at 20k magnification illustrating A-B, C, D, E) As-welded HAZ microstructures and T-B, C, D, E) Tempered HAZ microstructures

## 5.5 Summary

Initial weld optimization was performed to ensure consistent weld nugget for tempering. A two pulse welding scheme was used, with the first pulse to disrupt and displace the coating at the interface and the second pulse to grow the nugget to full size. Sufficient cooling time for tempering was also simulated and tested. Preliminary weld tempering exhibited secondary weld pool formation. This was caused by severe electrode misalignment, due to poor fit-up. Fine tuning of electrode alignment resolved the secondary weld pool formation, and the practical requirements for this in the field should be carefully considered.

Joint performance test indicated toughness decrease by 10% with initial tempering powers at 50 % max current, then revert back to better performance at higher tempering temperatures. Cross tensile performance indicated linear performance increase at initial tempering powers, with a peak at 55% max current temper. The maximum weld toughness improvement peaked at 51% in comparison with as-welded nugget. Performance improvement stops after 60% and increasing tempering powers. Three representative welds were selected from the joint performance data for detailed discussions: as-welded, optimally tempered (55% max current power), and overheated tempered (70% max current power).

Fractured cross tensile cross-sections illustrated interfacial/partial failure mode for as-welded nugget, and ductile pullout failure for the tempered nugget. The combination of fracture paths and increased effective nugget dimensions resulted increased weld performance.

Micro-hardness measurements and OM characterization indicated weld periphery softening with evidence of partial phase transformations and tempering beyond FB extending through HAZ. In addition, SCHAZ shift and growth away from FZ provided smooth hardness transitions, providing better joint performance. Micro-hardness results for overheated tempered weld indicated austenite transformation within the HAZ, further shifting SCHAZ away from the FZ. The retransformation of austenite near the

corona bond reintroduced notch sensitivity, resulting in brittle fracture paths. Finally, SEM analysis indicated increased carbide precipitation within UHAZ from the optimally tempered weld in comparison with as-welded nugget, concluding the presence of partial tempering.

Regardless of the joint performance improvements, the lengthened weld cycle time as a result of the tempering pulse may not be a popular weld tailoring alternative among automotive industries. However, it should be noted that weld tailoring is not required for all of the welds within a BIW structure. Only a selected few welds bridging between crumple zones and passenger compartment would be required for reduced peak loading and enhanced impact energy absorption during crash events. As such, the overall production time during assembly will not be significantly prolonged. Nevertheless, further improvements of the welding scheme for shorter cycle times will be more attractive. The discussion for potential future work will be covered in the next chapter.



## Chapter 6

### Conclusion and Recommendations

This research work aims to understand the effects of secondary current tempering on joint performance in resistance spot welding of USIBOR steels. The modification and optimization of welding schemes involved identifying corresponding joint mechanical strength, weld micro-hardness, failure modes, and microstructures. The results of RSW joints involving tempering in USIBOR steel with different conditions were presented to investigate the effects of in-process tempering currents. As such, the conclusions of this thesis are presented in the following sections, followed by future work pertaining to this research.

#### 6.1 RSW and In-Process Tempering of As-Delivered USIBOR Sheets

The objective of this chapter was to serve as a preliminary testing chapter for analyze the effects of in-process tempering on joint performance. The conclusions are as follows:

Interruption of the fusion zone formation a result of retained aluminized coating inhibiting heat generation was mitigated by the incorporation of high current pre-pulse. The added pre-pulse effectively disrupted the aluminized coating prior to main nugget formation.

Micro-hardness mapping, indicated significant weld tempering with diminishing hardness at increasing tempering power. Maximum softening occurred at 65% max current power and hardness reverted back into the 500Hv range with higher tempering currents. Joint mechanical strengths, however, did not correlate directly with tempering currents, due to a non-uniform weld structure. This was later confirmed with microstructural observations, indicating localized recrystallized zones within the weld corona, creating stress concentration, leading to performance decrease.

## 6.2 RSW and In-Process Tempering of Hot-Stamped USIBOR Sheets

The objective of this chapter was to investigate the effects that in-process tempering has on hot-stamped USIBOR during RSW in an attempt to improve nugget toughness and change the weld failure mode from interfacial to pullout fracture. The conclusions are as follows:

A modified welding and tempering parameter used for hot-stamped USIBOR welds in contrast to the as-delivered welds in the previous experiment. The optimized weld tensile and energy was achieved with 55% maximum current tempering parameter (4.4kA temper current for 0.5s). The tempered weld achieved an average 51% of weld toughness increase for cross-tension tests, with a minor toughness trade-off in tensile shear strength being reduced by 6% in comparison to non-tempered welds.

Fracture micrograph analysis indicated non-tempered welds failed in a brittle interfacial fracture, while the 55% maximum current tempered weld achieved pullout failure mode. The tempered weld fractured with crack initiating from the corona bond and propagating outwards through the HAZ and base metal, away from the weld nugget. The overall pullout button diameter (effective nugget diameter) measured at 8.6mm for the tempered weld, in contrast with the 6.4mm diameter for the non-tempered weld. Vickers hardness profile indicated gradual decrease in hardness within the HAZ, starting from the fusion boundary extending out to the SC-HAZ. The gradual HAZ hardness decrease, situating between the fully hardened weld nugget and base material, providing a smoother crack propagation path, and diminishing notch sensitivity for interfacial failure to occur.

Optical microscopy characterization indicated partial phase transformations and tempering beyond fusion boundary extending through HAZ for the tempered weld. Finally, SEM analysis indicated increased carbide precipitation within UCHAZ for the 55% max current tempered weld in comparison with as-welded nugget, concluding the occurrence of partial tempering within the HAZ.

Based on the experimental results, it is evident that weld toughness increase can be achieved, not by weld nugget tempering; however, by tailoring of HAZ width and hardness transition. Similar weld microstructure can be achieved by alternative welding parameter without the application of solidification time and tempering currents, ultimately shortening weld cycle times. Details of alternative welding method will be discussed in the next section.

### 6.3 Future Work Recommendations

This work has successfully show that the application of in-process weld tempering have beneficial improvements towards cross tensile joint performance. However, the findings from this study have prompted additional questions on possible improvements for weld tempering. An outlook for future work that will complement the present research field is presented in this section

Prolonged weld cycle time for in-process weld tempering is deemed too long for cycle times by majority of automotive industries. As such, improvements on welding scheme in terms of decreasing weld cycle times is necessary. One potential alternative to in-process weld tailoring while reducing weld cycle time is the application of post heating currents at lower power levels immediately after the main welding cycles (as such, a quench period will not be needed) [75]. This prolongs the HAZ thermal profile before it is quenched below  $M_s$  temperature, ensuring slower cooling within the HAZ, allowing pullout failure mode to occur. Similar idea has been attempted by Wakabayashi *et al.*; however, the type of steel used within their experiment was not specified to be 22MnB5 grade hot-stamping steel.

One area of concern was the joint performance behavior that the in-process tempering pulse have on dissimilar metal welds, specifically at locations that bridges crumple zones to the passenger compartment within a BIW assembly. Although not performed within this research thesis, weld tempering for RSW between USIBOR and other grades of AHSS, specifically DP, TRIP, or ArcelorMittal's DUCTIBOR,


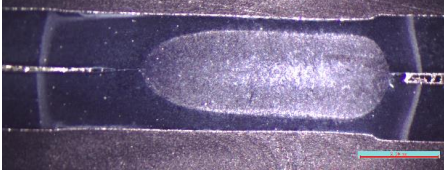
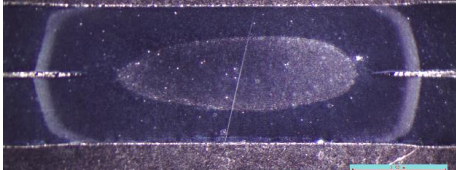
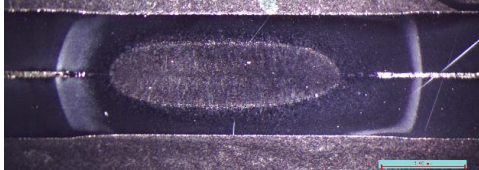
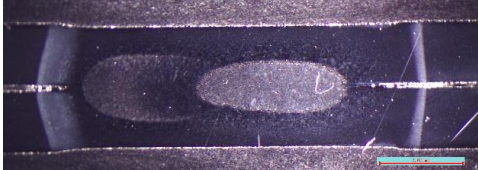

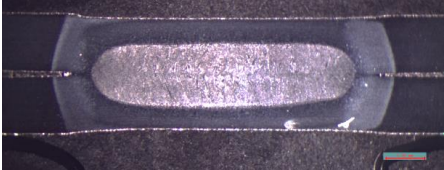

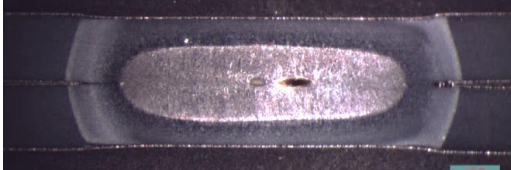
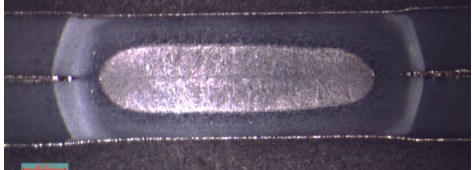
designed for crumple zones. Weld tempering research done on dissimilar metal welds will provide additional real-life application knowledge for in-process weld tempering.

Another area of concern for this study was the performance results of the tailored welds during crash events. Due to the lack of access to impact testing equipment, impact performance tests for the tempered welds was not performed. Explorations into crash performance will provide better insights on the actual effects of weld tailoring as well as weld behavior when surrounding material deforms. Impact studies also open up numerous solid mechanics topics for research.

One final concern for welding USIBOR is electrode longevity. Welding hot stamped USIBOR is known for decreased electrode life due to combination of increased material hardness leading to early deformation of electrode contact face and chemical reactions between coating and contact surface. With the addition of tempering pulses, it is apparent that electrode life will be shorter; however, this also creates new initiative for new electrode designs that will contribute to better electrode longevity.

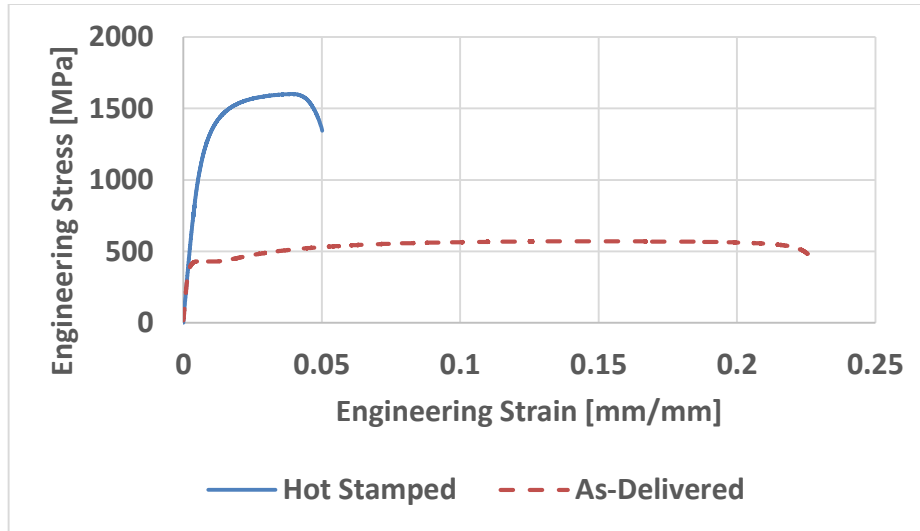
# Appendix A

## Hot-Stamped USIBOR Weld Stereoscopy Images

Electrode Misaligned Tempered Welds	
 <p>55% PWHT</p>	 <p>60% PWHT</p>
 <p>65% PWHT</p>	 <p>70% PWHT</p>
 <p>75% PWHT</p>	
Electrode Aligned Tempered Welds	
 <p>50% PWHT</p>	 <p>55% PWHT</p>
 <p>60% PWHT</p>	 <p>65% PWHT</p>
 <p>70% PWHT</p>	

## Appendix B

### Instrumented Experimental Data



**Figure 6-1: USIBOR 1500P Base Metal Tensile Data**

**Table 5: Tensile Shear Test Results for Hot-Stamped Tempered Welds**

Hot-Stamped Tempered Welds Tensile Shear Test Result						
Weld Type	Toughness % Difference	Fracture Force kN	Displacement mm	Energy N.m	Button Diameter mm	Failure Mode
As Welded	0.0%	27.41	1.06	17.29	7.54	IF
50% Max Current	-10.6%	25.84	1.02	15.46	7.22	PO
55% Max Current	-5.9%	26.42	1.05	16.28	7.10	PO
60% Max Current	-8.0%	26.12	1.04	15.91	7.20	PF
65% Max Current	1.7%	26.97	1.09	17.58	7.68	PF
70% Max Current	5.4%	27.90	1.10	18.22	9.47	PF

**Table 6: Cross Tensile Test Results for Hot-Stamped Tempered Welds**

<b>Hot-Stamped Tempered Welds Cross-Tensile Test Result</b>						
Weld Type	Toughness % Difference	Fracture Force kN	Displacement mm	Energy N.m	Button Diameter mm	Failure Mode
As Welded	0.0%	7.82	10.24	43.69	6.44	IF/PF
50% Max Current	35.9%	9.17	12.29	59.39	7.17	PO
55% Max Current	51.4%	9.99	13.63	66.17	7.24	PO
60% Max Current	13.9%	8.11	11.88	49.76	6.95	PO
65% Max Current	18.5%	9.02	10.56	51.76	6.86	PO
70% Max Current	11.0%	9.51	9.98	48.48	8.94	PO

## Bibliography

- [1] United States Environmental Protection Agency, "EPA and NHTSA Set Standards to Reduce Greenhouse Gases and Improve Fuel Economy for Model years 2017-2025 Cars and Light Trucks," US-EPA, 2012.
- [2] International Iron and Steel Institute, "Determination of Weight Elasticity of Fuel Economy for Conventional ICE Vehicles, Hybrid Vehicles, and Fuel Cell Vehicles," WorldAutoSteel, Middletown, OH, 2007.
- [3] International Iron and Steel Institute, "Communication Module Mass Reduction," WorldAutoSteel, Middletown, OH, 2006.
- [4] World Auto Steel - S. Keeler, M. Kimchi, "Advanced High-Strength Steel Application Guideline Version 5.0," WorldAutoSteel, 2014.
- [5] M. Pouranvari and S. P. H. Marashi, "Critical review of automotive steels spot welding: process, structure, and properties," *Science and Technology of Welding and Joining*, vol. 18, no. 5, pp. 361-403, 2013.
- [6] M. Takahashi, "Development of High Strength Steels for Automobiles," *Nippon Steel Technical Report*, vol. No. 88, pp. 1-7, 2003.
- [7] M. Maikranz-Valentin, U. Weidig, U. School, H. H. Becker and K. Steinhoff, "Components with Optimised Properties due to Advanced Thermo-mechanical Process Strategies in Hot Sheet Metal Forming," *Steel Research International*, vol. 79, no. 2, pp. 92-97, 2008.
- [8] ArcelorMittal, *Steels for Hot Stamping - Usibor*, ArcelorMittal, 2014.
- [9] A. Bardelcik, C. P. Salisbury, S. Winkler, M. Wells and M. J. Worswick, "Effect of cooling rate on the high strain rate properties of boron steel," *International Journal of Impact Engineering*, vol. 37, pp. 694-702, 2010.
- [10] H. Karbasian and A. Tekkaya, "A review on hot stamping," *Journal of Material Processing Technology*, no. 210, pp. 2103-2118, 2010.
- [11] S. Westgate, "The resistance spot welding of high and ultra-high strength steels," in *3rd International Seminar on Advances in Resistance Welding*, Berlin, Germany, 2004.
- [12] W. Hou, "Methods and Systems for Resistance Spot Welding using Direct Current Micro Pulses". United States of America Patent Patent Pending: Pub No. US 2001/0036816 A1, 17 February 2011.
- [13] R. Brooks, "Accepting the Challenge of Welding UHSS," *Welding Design & Fabrication*, 13 June 2013. [Online]. Available: <http://weldingdesign.com/processes/accepting-challenge-welding-uhss>. [Accessed November 2015].
- [14] I. Diallo, T. Dupuy and C. Kaczynski, "High Strength Steel Spot Weld Strength improvement through In Situ Post Weld Heat Treatment," in *Sheet Metal Welding Conference XVI*, Livonia, MI., 2014.
- [15] G. Shi and S. A. Westgate, "Resistance spot welding of high strength steels," in *11th International Conference on the Joining of Materials*, Helsingor, Denmark, 2003.
- [16] Y. J. Chao, "Failure mode of spot welds: interfacial versus pullout," *Science and Technology of Welding and Joining*, vol. 8, no. 2, pp. 133-137, 2003.



- [17] AWS D8 Committee on Automotive Welding, AWS D8.1M:2007 Specification for Automotive Weld Quality - Resistance Spot Welding of Steel, Miami, FL: American Welding Society , 2007.
- [18] AWS D8 Committee on Automotive Welding, AWS D8.9M:2012 Test Methods for Evaluating the Resistance Spot Welding Behaviour of Automotive Sheet Steel Materials, Miami, FL: American Welding Society, 2012.
- [19] ISO Internatial Standard, ISO 5821-2009: Resistance Welding - Spot Welding Electrode Caps, 2009.
- [20] ASTM International , E8-04: Standard Test Methods for Tension Testing of Metallic Materials, West Conshohocken, PA: ASTM International, 2004, pp. 1-.
- [21] N. T. Williams and J. D. Parker, "Review of resistance spot welding of steel sheets - Part 1," *International Materials Reviews*, vol. 49, no. 2, pp. 45-75, 2004.
- [22] Shinkokiki Co.,Ltd, "Basis and Point of Resistance Welding (1)," Shinkokiki Co., Ltd, 2014. [Online]. Available: <http://www.shinkokiki.co.jp/en/knowledge/miracle>. [Accessed November 2015].
- [23] H. Zhang and J. Senkara, "Electrothermal Processes of Welding," in *Resistance Welding - Fundamentals and Applications*, Boca Raton, FL, Taylor & Francis Group, 2006, pp. 19-57.
- [24] G. F. Scradler and A. K. Elshennawy, "Welding Process - Resistance Welding," in *Manufacturing Processes and Materials, Fourth Edition*, Scoeity of Manufacturing Engineers, 2000, pp. 306-311.
- [25] E. Thomson, "Method of Electric Welding". United States of America Patent 451,345, 28 April 1891.
- [26] Welding Information Center, "History of Welding," Welding Information Center - Library & Knowledge Base, 2004. [Online]. Available: [http://www.weldinginfocenter.com/history/his\\_01.html](http://www.weldinginfocenter.com/history/his_01.html). [Accessed September 2015].
- [27] K. R. Chan, *Weldability and Degradation Study of Coated Electrodes for Resistance Spot Welding*, Waterloo: University of Waterloo, 2005.
- [28] D. C. Saha, C. W. Ji and Y. D. Park, "Coating behaviour and nugget formation during resistance welding of hot forming steels," *Science and Technology of Welding and Joinin*, vol. 00, no. 0, pp. 1-14, 2015.
- [29] M. Uran and U. Zupanc, *Dynamic resistance of surfac- protected high-strength martensitic steels*, International Institute of Welding.
- [30] W. Li, E. Feng, D. Cerjanec and G. A. Grzadzinski, "Energy Consumption in Ac and MFDC Resistance Spot Welding," in *Sheet Metal Welding Conference XI*, Sterling Heights, MI, 2004.
- [31] S. Hwang, M. J. Kang and D. C. Kim, "Expulsion Reduction in Resistance Spot Welding by Controlling of welding Current Waveform," *Physics Engineering*, vol. 10, pp. 2775-2781, 2011.
- [32] H. Zhang and J. Senkara, "Influence of Mechanical Characteristics of Welding Machines," in *Resistance Spot Welding - Fundamental and Application*, Boca Raton, FL, Taylor & Francis Group, 2006, pp. 287-337.
- [33] H. Tang, W. Hou, S. J. Hu, H. Y. Zhang, Z. Feng and M. Kimchi, "Influence of Welding Machine Mechanical Characteristics on the Resistance Spot Welding Process and Weld Quality," *Welding Research*, pp. 116-124, 2003.
- [34] H. A. Neid, "The Finite Element Modelling of the Resistance Spot Welding Process," *Welding Research Supplement*, pp. 123-132, 1984.
- [35] J. Senkara, H. Zhang and S. J. Hu, "Expulsion Prediction in Resistance Spot Welding," *Welding Journal*, pp. 123-132, 2004.

- [36] H. Zhang and J. Senkara, "Mechanical Testing," in *Resistance Spot Welding - Fundamental and Application*, Boca Raton, FL, Taylor & Francis Group, 2006, pp. 107-119.
- [37] D. J. Radakovic and M. Tumuluru, "An Evaluation of the Cross-Tensio Test of Resistance Spot Welds in High-Strength Dual-Phase Steels," *Welding Research*, vol. 91, no. s, pp. 8-15, 2012.
- [38] D. J. Radakovic and M. Tumuluru, "Predicting Resistance Spot Weld Failure Modes in Shear Tension Tests of Advanced High-Strength Automotive Steels," *Welding Research*, vol. 87, no. s, pp. 96-105, 2008.
- [39] Y. J. Chao, "Ultimate Strength and Failure Mechanism of Resistance Spot Weld Subjected to Tensile, Shear, or Combined Tensile/Shear Loads," *Journal of Engineering Materials and Technology*, vol. 125, pp. 125-132, 2003.
- [40] M. I. Khan, M. L. Kuntz and Y. Zhou, "Effects of weld microstructure on static and impact performance of resistance spot welded joints in advanced high strength steels," *Science and Technology of Welding and Joining*, vol. 13, no. 3, pp. 294-304, 2008.
- [41] M. Pouranvari and S. P. H. Marashi, "Failure mode transition in AHSS resistance spot welds. Part I. Controlling Factors," *Materials Science and Engineering A*, no. 528, pp. 8337-8343, 2011.
- [42] M. Pouranvari, H. R. Asgari, S. M. Mosavizadch, S. P. H. Marashi and M. Goodarzi, "Effect of weld nugget size on overload failure mode of resistance spot welds," *Science and Technology of Welding and Joining*, vol. 12, no. 3, pp. 217-225, 2007.
- [43] K. Stearling, in *Introduction to the physical metallurgy of welding*, Butterworths & Co (Publishers) Ltd., 1983, pp. 110-112.
- [44] H. Zhang and J. Senkara, "Welding Metallurgy," in *Resistance Spot Welding - Fundamentals and Application*, Boca Raton, FL, Taylor & Francis Group, 2006, pp. 1-5.
- [45] S. Kou, "Fusion Zone - Weld Metal Solidification II: Microstructure within Grains," in *Welding Metallurgy 2nd Edition*, Hoboken, New Jersey, John Wiley and Sons, Inc., 2002, pp. 199-209.
- [46] J. C. Lippold, *Welding Metallurgy and Weldability*, John Wiley & Sons, 2014.
- [47] A. K. Sinha, "Basic Heat Treatment - Homogenizing," in *Physical Metallurgy Handbook*, McGraw-Hill, 2003, p. 12.5.
- [48] A. K. Sinha, "Martensite," in *Physical Metallurgy Handbook*, McGraw-Hill, 2003, pp. 8.1-8.36.
- [49] ASM International. Handbook Committe, "Microstructure, Processing, and Properties of Steel (Martensite)," in *ASM Handbook 10th ed.*, Materials Park, OH, ASM International, 1990, pp. 133-137.
- [50] S. Morito, X. Huang, T. Furuhashi, T. Maki and N. Hansen, "The morphology and crystallography of lath martensite in alloy steels," *Acta Materialia*, vol. 54, pp. 5323-5331, 2006.
- [51] S. Morito, H. Tanaka, R. Konishi, T. Furuhashi and T. Maki, "The morphology and crystallography of lath martensite in Fe-C alloys," *Acta Materialia*, vol. 51, pp. 1789-1799, 2003.
- [52] A. K. Sinha, "Tempering," in *Physical Metallurgy Handbook*, McGraw-Hill, 2003, pp. 14.1-14.59.
- [53] G. R. Speich and W. C. Leslie, "Tempering of Steel," *Metallurgical Transactions*, vol. 3, pp. 1043-1054, 1972.
- [54] R. A. Grange, C. R. Hribal and L. F. Porter, "Hardness of Tempered Martensite in Carbon and Low-Alloy Steels," *Metallurgical Transactions A*, vol. 8, no. A, pp. 1775-1785, 1977.

- [55] K. Cvetkovski, J. Ahlstrom and B. Karlsson, "Influence of short heat pulses on properties of martensite in medium carbon steels," *Materials Science and Engineering A*, vol. 561, pp. 321-328, 2013.
- [56] E. Biro, J. R. McDermid, S. Vignier and Y. Zhou, "Decoupling of the softening processes during rapid tempering of a martensitic steel," *Materials Science and Engineering A*, vol. 615, pp. 395-404, 2014.
- [57] E. Biro, S. Vignier, C. Kaczynski, J. R. McDermid, E. Lucas, J. D. Embury and Y. Zhou, "Predicting Transient Softening in the Sub-Critical Heat-Affected Zone of Dual-Phase and Martensitic Steel Welds," *ISIJ International*, vol. 53, no. 1, pp. 110-118, 2013.
- [58] V. H. Baltazar, S. S. Nayak and Y. Zhou, "Tempering of Martensite in Dual-Phase Steels and Its Effects on Softening Behaviour," *Metallurgical and Materials Transactions A*, pp. 1-15, 2011.
- [59] M. Merklein and J. Lechler, "Investigation of the thermo-mechanical properties of hot stamping steels," *Journal of Materials Processing Technology*, vol. 177, pp. 452-455, 2006.
- [60] M. Suehiro, J. Maki, K. Kusumi, M. Ohgami and T. Miyakoshi, "Properties of Aluminium-Coated Steels for Hot-Forming," *Nippon Steel Technical Report*, no. 88, pp. 16-21, 2003.
- [61] D. W. Fan and B. C. D. Cooman, "State-of-the-knowledge on Coating Systems for Hot Stamped Parts," *Steel Research International*, vol. 83, pp. 1-22, 2012.
- [62] Salzgitter Flachstahl, *22MnB5 Boron Alloyed Quenched and Tempered Steel*, Salzgitter Flachstahl GmbH, 2007.
- [63] A. K. Sinha, "Iron-Carbon Alloys," in *Physical Metallurgy Handbook*, McGraw-Hill, 2003, pp. 1.1-1.68.
- [64] R. Veit, H. Hofmann, R. Kolleck, P. Brugger, I. Thomas and S. Sikora, *Phase Formation of Al/Si Coatings during Induction Heating of Boron Alloyed Steel Sheets*, Graz, Austria: Graz University of Technology - Institute Tools and Forming.
- [65] J. P. Kong and C. Y. Kang, "Effect of alloying elements on expulsion in electric resistance spot welding of advanced high strength steels," *Science and Technology of Welding and Joining*, vol. 00, no. 0, pp. 1-11, 2015.
- [66] C. W. Ji, I. Jo, H. Lee, I. D. Choi, Y. D. Kim and Y. D. Park, "Effects of surface coating on weld growth of resistance spot welded hot-stamped boron steels," *Journal of Mechanical Science and Technology*, vol. 28, no. 11, pp. 4761-4769, 2014.
- [67] E. Schmidova and P. Hanus, "Weldability of Al-Si Coated High Strength Martensitic Steel," *Periodica Polytechnica*, vol. 41, no. 2, pp. 127-132, 2013.
- [68] S. Furusako, G. Murayama, H. Oikawa, T. Nose, F. Watanbe, H. Hamatani and Y. Takahashi, "Current Problems and the Answer Techniques in Welding Technique of Auto Bodies - First Part," Nippon Steel, Chiba, JP, 2013.
- [69] Y. S. Jong, Y. K. Lee, D. C. Kim, M. J. Kang, I. S. Hwang and W. B. Lee, "Microstructural Evolution and Mechanical Properties of Resistance Spot Welded Ultra High Strength Steel Containing Boron," *Materials Transactions*, vol. 52, no. 6, pp. 1330-1333, 2011.
- [70] W. L. Chuko and J. E. Gould, "Development of appropriate resistance spot welding practice for transformation-hardened steels," *AWS Welding Journal*, pp. 1-7, 2002.
- [71] Swantec Software and Engineering APS, "SORPAS 2D Version 11.5," Swantec Software and Engineering APS, Lyngby, Denmark, 2013.

- [72] K. Lowes, O. L. Ighodaro, E. Biro and N. Zhou, "Optimizing Spot Welding Schedules for Tailor Welded Patch Applications in Press Hardened Steels," in *Sheet Metal Welding Conference XVI*, Livonia, Mi, 2014.
- [73] J. Hou, K. Chan, N. Scotchmer, N. Zhou and A. Gerlich, "In-Situ Tempering of Hot Stamped Martensitic Steel," in *Sheet Metal Welding Conference XVI*, Livonia, Mi, 2014.
- [74] D. C. Saha and Y.-D. Park, "Weldability and Liquation Cracking Characteristics on Resistance Spot Welded High-Mn Austenitic Steel," in *ASM International - Trends in Welding Research IX*, Chicago, IL, 2012.
- [75] C. Wakabayashi, S. Furusako and Y. Miyazaki, "Strengthening spot weld joining by autotempering acceleration at heat affected zone," *Science and Technology of Welding and Joining*, vol. 20, no. 6, pp. 468-472, 2015.